



**UNIVERSITY OF THESSALY**  
**SCHOOL OF PUBLIC HEALTH**  
**MEDICAL SCHOOL**



DEPARTMENT OF MEDICAL PHYSICS

Director: Professor Constantin Kappas

---

PhD Dissertation

**"Monte Carlo simulation of modern techniques of intensity modulated  
radiation therapy (IMRT)"**

from

**PANAGIOTIS TSIAMAS**

PhD candidate of Medical Physics 2012

Submitted as part of  
the requirements requested for obtaining  
a PhD Diploma  
Larissa, 2012



DANA-FARBER/BRIGHAM AND WOMEN'S





**ΠΑΝΕΠΙΣΤΗΜΙΟ ΘΕΣΣΑΛΙΑΣ**  
**ΣΧΟΛΗ ΕΠΙΣΤΗΜΩΝ ΥΓΕΙΑΣ**



**ΤΜΗΜΑ ΙΑΤΡΙΚΗΣ**

ΤΜΗΜΑ ΙΑΤΡΙΚΗΣ ΦΥΣΙΚΗΣ

Διευθυντής: Καθηγητής Κωνσταντίνος ΚΑΠΠΑΣ

Διδακτορική Διατριβή

**"Monte Carlo εξομοίωση σύγχρονων τεχνικών διαμορφούμενης έντασης  
ακτινοθεραπείας (IMRT)"**

υπό

**ΠΑΝΑΓΙΩΤΗ ΤΣΙΑΜΑ**

Υποψήφιος Διδακτωρ Ιατρικής Φυσικής 2012

Υπεβλήθη για την εκπλήρωση μέρους των  
απαιτήσεων για την απόκτηση του  
Διδακτορικού Διπλώματος  
Λάρισα, 2012



DANA-FARBER/BRIGHAM AND WOMEN'S



© 2012 Παναγιώτης Τσιάμας

Η έγκριση της διδακτορικής διατριβής από το Τμήμα Ιατρικής της Σχολής Επιστημών Υγείας του Πανεπιστημίου Θεσσαλίας δεν υποδηλώνει αποδοχή των απόψεων του συγγραφέα (Ν. 5343/32 αρ. 202 παρ. 2).

**Εγκρίθηκε από τα Μέλη της Επταμελούς Εξεταστικής Επιτροπής  
(6<sup>η</sup>/11 - 07 - 2012 ΓΣΕΣ):**

- |   |   |
|---|---|
| <b>1<sup>ος</sup> Εξεταστής<br/>(Επιβλέπων)</b> | <b>Δρ. Κωνσταντίνος Κάππας</b><br><i>Καθηγητής Ιατρικής Φυσικής, Τμήμα Ιατρικής, Πανεπιστήμιο Θεσσαλίας</i>                           |
| <b>2<sup>ος</sup> Εξεταστής</b>                 | <b>Δρ. Κυριακή Θεοδώρου</b><br><i>Επίκουρη Καθηγήτρια Ιατρικής Φυσικής – Πληροφορικής, Τμήμα Ιατρικής, Πανεπιστήμιο Θεσσαλίας</i>     |
| <b>3<sup>ος</sup> Εξεταστής</b>                 | <b>Dr. Piotr Zygmanski</b><br><i>Assistant Professor of Radiation Oncology, BWH/ DFCI, Harvard Medical School</i>                     |
| <b>4<sup>ος</sup> Εξεταστής</b>                 | <b>Δρ. Τζων Καλέφ-Εζρά</b><br><i>Καθηγητής Ιατρικής Φυσικής, Τμήμα Ιατρικής, Πανεπιστήμιο Ιωαννίνων</i>                               |
| <b>5<sup>ος</sup> Εξεταστής</b>                 | <b>Δρ. Δημήτριος Εμφιετζόγλου</b><br><i>Επίκουρος Καθηγητής Ιατρικής Φυσικής, Τμήμα Ιατρικής, Πανεπιστήμιο Ιωαννίνων</i>              |
| <b>6<sup>ος</sup> Εξεταστής</b>                 | <b>Δρ. Γεώργιος Κύργιας</b><br><i>Επίκουρος Καθηγητής Ακτινοθεραπείας, Τμήμα Ιατρικής, Πανεπιστήμιο Θεσσαλίας</i>                     |
| <b>7<sup>ος</sup> Εξεταστής</b>                 | <b>Δρ. Παναγιώτα Ματσουκά</b><br><i>Καθηγήτρια Παθολογίας-Αιματολογίας, Τομέας Παθολογίας, Τμήμα Ιατρικής, Πανεπιστήμιο Θεσσαλίας</i> |

*Approved from all members of the seven-member examination committee  
(6<sup>th</sup> /11 - 07 - 2012 ΓΣΕΣ):*

<b>1<sup>st</sup> Examiner (Supervisor)</b>	<b>Dr. Constantinos Kappas</b> <i>Professor of Medical Physics, Medical School, University of Thessaly</i>
<b>2<sup>nd</sup> Examiner</b>	<b>Dr. Kiriaki Theodorou</b> <i>Assistant Professor of Medical Physics – Information Science, Medical School, University of Thessaly</i>
<b>3<sup>rd</sup> Examiner</b>	<b>Dr. Piotr Zygmanski</b> <i>Assistant Professor of Radiation Oncology, BWH/DFCI, Harvard Medical School</i>
<b>4<sup>th</sup> Examiner</b>	<b>Dr. John Kalef-Ezra</b> <i>Professor of Medical Physics, Medical School, University of Ioannina</i>
<b>5<sup>th</sup> Examiner</b>	<b>Dr. Dimitrios Emfietzoglou</b> <i>Assistant Professor of Medical Physics, Medical School, University of Ioannina</i>
<b>6<sup>th</sup> Examiner</b>	<b>Dr. George Kyrgias</b> <i>Assistant Professor of Radiation Therapy, Medical School, University of Thessaly</i>
<b>7<sup>th</sup> Examiner</b>	<b>Dr. Panayota Matsouka</b> <i>Professor of Pathology-Hematology, Departments of Pathology, Medical School, University of Thessaly</i>

# "Monte Carlo εξομοίωση σύγχρονων τεχνικών διαμορφούμενης έντασης ακτινοθεραπείας (IMRT)"

**ΠΑΝΑΓΙΩΤΗΣ ΤΣΙΑΜΑΣ**

Πανεπιστήμιο Θεσσαλίας, Τμήμα Ιατρικής, 2012

## **ΤΡΙΜΕΛΗΣ ΣΥΜΒΟΥΛΕΥΤΙΚΗ ΕΠΙΤΡΟΠΗ**

- 1. Δρ. Κωνσταντίνος Κάππας**, Καθηγητής Ιατρικής Φυσικής, Τμήμα Ιατρικής, Πανεπιστήμιο Θεσσαλίας, (Επιβλέπων)
- 2. Δρ. Κυριακή Θεοδώρου**, Επίκουρη Καθηγήτρια Ιατρικής Φυσικής - Πληροφορικής, Τμήμα Ιατρικής, Πανεπιστήμιο Θεσσαλίας
- 3. Δρ. Piotr Zygmanski**, Επίκουρος Καθηγητής Ακτινοθεραπευτικής Ογκολογίας, BWH/DFCI, Τμήμα Ιατρικής, Πανεπιστήμιο Χάρβαρντ.

# **"Monte Carlo simulation of modern radiotherapy treatment techniques of intensity modulated radiation therapy (IMRT)"**

**PANAGIOTIS TSIAMAS**

University of Thessaly, Medical School, 2012

## ***THREE MEMBER ADVISORY COMMITTEE***

- 1. Dr. Constantinos Kappas**, Professor of Medical Physics, Medical School, University of Thessaly, **(Supervisor)**
- 2. Dr. Kiriaki Theodorou**, Assistant Professor of Medical Physics – Information Science, Medical School, University of Thessaly
- 3. Dr. Piotr Zygmanski**, Assistant Professor of Radiation Oncology, BWH/DFCI, Harvard Medical School

*Στην οικογένεια μου,  
που ήταν το αεράκι  
που «έσπρώξε» τα πανιά μου,*

*Στους φίλους μου,  
που ταξιδεύουν πάντα μαζί μου  
ακόμα και όταν είμαστε σε διαφορετικές θάλασσες,*

*Και στην μούσα μου,  
που θα με πάει σε νέες περιπέτειες*



## ACKNOWLEDGEMENTS

This dissertation not only represents my work of the past three years, since October 2009 when I started my PhD journey, but also is a result of encounters and collaborations at various levels with different people. As each person's contribution to my PhD dissertation is unique I have decided to mention them in chronological order.

Firstly, I would like to thank Professor Constantine Kappas, for being the one who introduced me in 2001 to the fascinating world of Medical Physics for the first time. Together with Assistant Professor Kiki Theodorou, I have to specially thank them both for two reasons: for bringing me in to the MC world and for giving me the opportunity to go to Boston and complete my PhD at BWH. Moreover, I would like to thank Instructor Ioannis Tsougos not only for his scientific help but also for his kind friendship. Special thanks to Thomas Killindris for giving me all the necessary programming tools for my "Bostonian" experience.

Next, I would like to express my deepest gratitude to Professor Mike Makrigiorgos and Doctor Associate Professor Karen Marcus for giving me the opportunity to join BWH/DFCI and for supporting me during the period of my PhD work.

Last but not least, I would like to thank Assistant Professor Piotr Zygmanski, who was my immediate mentor at BWH. I would like to thank him for supporting me from day one in Boston. Most of all I would like to thank him for teaching me a great lesson through everyday practice of science with its ups and downs and nonetheless making a steady progress towards the goal of my dissertation. I learned that scientific integrity comes through patience, hard work and cool headed evaluation of the details and not through big fancy words.

Special thanks to Professor Erno Sajo for our many fruitful discussions on Monte Carlo simulation and physics.

Finally, I would like to thank all of my colleagues throughout these years, for their help and support, in particular: Eva, Evaggelia, John, Giannis, Nikos, Michalis, Sook Kien Ng, Joerg, Zhaohui Han, Mandar Bhagwat, and Fulya Cifter. Many thanks to other professional colleagues: Assistant Professor Joao Seco, Assistant Professor Yulia Lyatskaya, Assistant Professor Ross Berbeco and Dr. Wil Nwga.

These acknowledgements would be incomplete if I would not mention my family: Maria and Kostas, Aris, Tonia and Giota, as well as my "Bostonian" family: Ioannis, Popi, Fillipos, Alexandra, Mariza, Christos and Charis.

# Curriculum Vitae

## PERSONAL INFORMATION

Surname:	<b>Tsiamas</b>
Name:	<b>Panagiotis</b>
Date of Birth:	11 July 1980
Place of Birth:	Athens, Attica, Greece
Address:	98A Longwood Ave. Apt. 4
Place of Residence:	Brookline, MA 02446, USA
Mobile:	6974-306274/ 617-869-4504
Email:	<a href="mailto:ptsiamas@partners.org">ptsiamas@partners.org</a>

## CURRENT STATUS

- **Mar 2009 – presence:** PhD Student in Medical Physics, Medical School, University of Thessaly, Greece (PhD started: March 2009; expected graduation: September 2012).
- **Oct 2009 – presence:** Research fellow Harvard Medical school, radiation oncology department.
- **Oct 2009 – presence:** Research fellow at Brigham and Women's Hospital and in Dana – Farber Institute.

## PhD RUNNING TITLE

- Monte Carlo simulation with modern techniques of intensity modulated radiation therapy (IMRT).

## EDUCATION

- Master's Degree in Medical Physics.  
Medical Physics Department, Medical School, University of Patras Greece (2008).
- Bachelor Degree in Physics.  
Physics Department, Aristotle University of Thessaloniki, Greece (2006).

## DISSERTATION

- **Master Dissertation:** "Out of field Spectrum determination of Electra's SL-18 Linac with MLC, for 6 and 15 MV, with Monte Carlo simulation", Medical School, University of Patras, (2008).
- **Bachelor Dissertation:** "Dosimetry with Monte Carlo techniques in radiation therapy", Aristotle University of Thessaloniki, Greece (2006).

## PAPERS PUBLISHED PEER-REVIEWED SCIENTIFIC JOURNALS

1. **Tsiamas P**, Seco J, Han Z, Bhagwat M, Maddox J, Kappas C, Theodorou K, Makrigiorgos M, Marcus K and Zygmanski P, "A modification of flattening filter free linac for IMRT", Medical Physics 2011, (38), 2342 - 2352.
2. Ngwa W, **Tsiamas P**, Zygmanski P, Makrigiorgos GM, Berbeco RI, "A multipurpose quality assurance phantom for the small animal radiation research platform (SARRP)", Phys Med Biol. May 7;57(9):2575-86, 2012.

## PAPERS SUBMITTED IN PEER-REVIEWED SCIENTIFIC JOURNALS

1. **P Tsiamas**, B Liu, F Cifter, W F. Ngwa, R I Berbeco, C Kappas, K Theodorou, K Marcus, M G. Makrigiorgos, E Sajo, P Zygmanski, "Impact of beam quality on megavoltage radiotherapy

treatment techniques utilizing gold nanoparticles for dose enhancement”, Under review – Radiotherapy & Oncology.

2. **P. Tsiamas**, E. Sajo, F. Cifter, K. Theodorou, C. Kappas, M. Makrigiorgos, K. Marcus, P. Zygmanski, “Beam quality and dose perturbation of 6 MV flattening-filter-free beams”, under review – European Journal of medical physics.
3. F Cifter, **P Tsiamas**, P Zygmanski, E Sajo, “Parametric Study of Gold Nanoparticle Dose Enhancement Using Deterministic Computations” Under review – Medical Physics.
4. Sajo E, **Tsiamas P**, Cifter F, Zygmanski P “Deterministic computations of nanoscale energy deposition about nanoparticles”, Under review – Medical Physics.
5. A Detappe, **P Tsiamas**, W Ngwa, P Zygmanski and R Berbeco, “The effect of flattening filter free delivery on endothelial dose enhancement during gold nanoparticle-aided radiotherapy”, Under Review – Phys Med Biol.
6. P Zygmanski, W Hoegel, **P Tsiamas**, F Cifter, E Sajo, “A stochastic model of cell survival for high-Z nanoparticle radiotherapy” Under review – Medical Physics.
7. L Wack, W Ngwa, E Tryggestad, **P Tsiamas**, R Berbeco, S K Ng, J Hesser and P Zygmanski, “Kilovoltage beam of a small animal irradiator: Film dosimetry in homogeneous and heterogeneous media”, under review – European Journal of medical physics.

## ORAL PRESENTATIONS

1. Ngwa W, **Tsiamas P**, Zygmanski P, Makrigiorgos GM, Berbeco RI, “A Multipurpose Quality Assurance Phantom for the Small Animal Radiation Research Platform (SARRP)”, TU-C-BRB-06: Med Phys., 39 (6), 3899, 2012.
2. “A straightforward conversion of IMRT plans optimized for the standard linac for delivery on FFF linac without re-optimization”, International Workshop of Recent Advances in Monte Carlo Techniques for Radiation Therapy June 8-10, 2011 Montreal – Canada.
3. “A modification Filter Free (FFF) linac”, NEAAPM – young investigation symposium, May 2011.

## POSTER PRESENTATIONS

1. **Tsiamas P**, Sajo E, Cifter F, Theodorou K, Kappas K, Makrigiorgos M, Marcus K, Zygmanski P., “Optimal Clinical Megavoltage X-Ray Beam Quality for Contrast Enhanced RT (CERT)”, SU-E-T-35, Med Phys., Jun;39 (6), 3710, 2012.
2. Matching of Flattening-Filter-Less (FFL) to Standard (STD) linac beams based on Monte Carlo simulations Innovation/Impact.”, SU-GG-T-387, Med. Phys. June;37, 3275, 2010.
3. “Monte Carlo study of the out-of-field spectra for 6MV and 15MV photon beams with and without MLC”. Theodorou K, Parameritis I, **Tsiamas P**, Kappas C, ESTRO meeting 2008, Gotenborg Sweden.

## PARTICIPATION IN INTERNATIONAL CONFERENCES - TEACHING COURSES

1. 54th Annual Meeting of the American Association of Physicists in Medicine, Charlotte, North Carolina, July 29- August 2, 2012.
2. International Workshop of Recent Advances in Monte Carlo Techniques for Radiation Therapy, Montreal – Canada June 8-10, 2011.
3. 52nd Annual Meeting of the American Association of Physicists in Medicine, Philadelphia, Pennsylvania, July 18-22, 2010
4. Physics for Clinical Radiotherapy, ESTRO course, Athens, Greece, 2009

## PARTICIPATION IN NATIONAL CONFERENCES - TEACHING COURSES

- Certificate of attendance in the 11<sup>th</sup> Interuniversity Symposium organized by the “Aristotle’s” Institute, with subject “Multidisciplinary Approach in Oncology & Treatment Planning”. Thessaloniki 29 August –1 September.

- Meeting of Hellenic Committee Atomic Energy on “Radiation Protection in Radiology”, 30 March 2007, Athens.
- National Symposium of “Genomatics and Nanotechnology in Biomedicine” hosted by the Institute of Biomedical Research and Technology (IBET) in cooperation with the Medical Department of the University of Thessaly, 30 November-1 December 2007, Larissa.
- 3<sup>rd</sup> Symposium of Vascular Surgery and Angiology of the University of Thessaly, 23-25 May 2008, Larissa.
- “Seminar on Radiation Protection”, 3<sup>rd</sup> Symposium of Vascular Surgery and Angiology of the University of Thessaly, 24 May 2008, Larissa.
- Symposium on “Evolutions in Nuclear Medicine”, 12-14 September 2008, Volos.

#### **MEMBER OF INTERNATIONAL SCIENTIFIC COMMUNITY**

- AAPM (American Association of Physicists in Medicine)
- ESTRO Member (European Society for Therapeutic Radiology and Oncology).
- ABR (American Board of Radiology)

#### **CLINICAL PRACTICE AND EXPERIENCE**

- Clinical training in the Physics of Nuclear Medicine in “Evangelismos” Hospital, Athens, Greece, 2009.
- Clinical training in the Physics of Radiotherapy in the University Hospital of Larissa, Greece, 2008-2009.
- Clinical training in the Physics of Diagnostic Radiology in the University Hospital of Larissa, Greece, 2008-2009.

#### **PROFESSIONAL LICENSES**

- American Board of Radiology (ABR) Part I Radiologic Physics (2011).
- License of practicing Medical Physics in the area of Non Ionizing Radiation (Ministry of Health, Athens, Greece, 2009).

## Περίληψη/Επιτομή

Η ακτινοθεραπεία αντιμετωπίζει ένα παλαιό-συνεχές δίλλημα: πώς να μεγιστοποιηθεί η εναπόθεση δόσης στα καρκινικά κύτταρα με την ταυτόχρονη εκμηδένιση της δόσης στα αντίστοιχα περιβάλλοντα υγιή. Σκεπτόμενοι πάνω σε αυτούς τους άξονες υπάρχουν δύο κυρίαρχοι παράγοντες που πιθανόν θα διαδραματίσουν σημαντικό ρόλο στο μέλλον. Ο πρώτος αφορά στην ανακάλυψη νέων φυσικών διαδικασιών και φαινομένων μεταξύ ακτινοβολίας και ύλης. Ο δεύτερος σχετίζεται με την ανάπτυξη νέων πηγών ακτινοβολίας, των οποίων οι ιδιότητες είναι προσαρμοσμένες έτσι ώστε να επιτευχθεί ο αρχικός στόχος. Προκύπτει λοιπόν ένα σημαντικό ερώτημα: Πώς να εισαχθούν νέες θεραπευτικές φόρμες με το μικρότερο δυνατό ρίσκο και βασισμένες στην ήδη υπάρχουσα κλινική εμπειρία που έχει προκύψει από τις υπάρχουσες συμβατικές θεραπευτικές τεχνικές;

Στόχος της παρούσας διδακτορικής διατριβής ήταν η προσπάθεια απάντησης στο τελευταίο ερώτημα μέσω της διερεύνησης εναλλακτικών τρόπων τροποποίησης της δέσμης του γραμμικού επιταχυντή, καθώς επίσης και του χαρακτηρισμού των δοσιμετρικών ιδιοτήτων, σε μικροσκοπικό και νανοσκοπικό επίπεδο, εφαρμογών διαμορφωμένης έντασης ακτινοθεραπείας (IMRT) και/ ή θεραπείας με νανοσωματίδια χρυσού (GNPT). Ιδιαίτερη έμφαση δε, δόθηκε στην τεχνική IMRT , χρησιμοποιώντας ως κύριο εργαλείο την μέθοδο Μοντε Κάρλο.

Συγκεκριμένα η παρούσα διδακτορική διατριβή χωρίστηκε σε τρία κυρίως μέρη. Στο πρώτο μελετήθηκε ένα εναλλακτικό σχέδιο γραμμικού επιταχυντή, μετά την αφαίρεση του φίλτρου της δέσμης, καθώς και οι αντίστοιχες επιδράσεις της χρήσης ενός τέτοιου μοντέλου σε περιπτώσεις θεραπείας με τεχνικές IMRT. Το προτεινόμενο σχέδιο γραμμικού επιταχυντή διατηρεί όλα τα πλεονεκτήματα ενός γραμμικού χωρίς φίλτρο, βελτιώνοντας σημαντικά τον ρυθμό δόσης και περιορίζοντας την σκέδαση που προέρχεται από την κεφαλή του γραμμικού. Από την άλλη η χρήση του παρουσιάζει προκλίσεις για μεγάλα πεδία και έκκεντρους στόχους. Στο δεύτερο μέρος της παρούσας διδακτορικής διατριβής πραγματοποιήθηκε μία εκτεταμένη ποιοτική και ποσοτική μελέτη άνω των 1300 φασμάτων διαφορετικών δεσμών ακτινοβολίας. Τα αποτελέσματα αυτής της μελέτης χρησιμοποιήθηκαν στο τρίτο και τελευταίο μέρος, στο οποίο μελετήθηκε το δοσιμετρικό αποτέλεσμα των προαναφερθέντων δεσμών ακτινοβολίας σε μικροσκοπικό επίπεδο, στην περίπτωση που νανοσωματίδια χρυσού είναι παρόντα. Επισημάνθηκαν οι βέλτιστες κλινικά τεχνικές ακτινοβολήσης που εγκυτώνται αποτελεσματική και ασφαλή εναπόθεση δόσης για ακτινοθεραπεία επαυξημένη με νανοσωματίδια χρυσού. Εν κατακλείδι στην παρούσα διδακτορική διατριβή μελετήθηκαν μη εφαρμοσμένες φυσικές διεργασίες υπό το πρίσμα μίας καινούργιας θεραπευτικής φόρμας (GNPT) και καθορίστηκαν οι βέλτιστες τεχνικές ακτινοθεραπείας που θα οδηγήσουν σε σταδιακή και ασφαλή κλινική εφαρμογή της.

## Summary/ Abstract

Clinical delivery of radiation therapy faces an old dilemma: how to maximize the dose to the tumoral cells while sparing the surrounding healthy tissue. Along this path two major innovations will most likely play an important role in the future. The first has to do with the employment of so far unutilized physical processes and effects of radiation with matter. The second one is associated with the development of new radiation sources whose properties are better suited to achieve the latter goal. An important question arises in this respect: how to introduce new treatment modalities with minimal risk relying on our extensive past clinical experience with the conventional treatment techniques.

The current PhD dissertation tries to answer this question by investigating alternative ways to modify the linear accelerator beam line and characterizing dosimetric properties at the macroscopic and nanoscopic level in application to Intensity Modulated Radiotherapy (IMRT) and/or Gold Nanoparticle Therapy (GNPT). Emphasis is given to IMRT with and without the presence of gold nanoparticles while the main tool used for all the studies is Monte Carlo method of radiation transport

The dissertation is divided into three major parts. In the first one, an alternative linac design is investigated by removing the flattening filter of the beam and by studying its impact on IMRT delivery. The flattening free linac design keeps all the benefits of the standard linac, while improving significantly dose rate and limiting head scatter. On the other hand it is being presents challenges for large IMRT fields and far off-axis points. In the second part of the dissertation an extensive qualitative and quantitative beam quality/ spectra study is carried for over 1300 different clinical irradiation conditions. The results from the second part are used in the third and last part of the dissertation in which the dosimetric impact of these different beam qualities on gold nanoparticle radiotherapy are studied. Optimal clinical irradiation techniques are identified which guarantee efficient and safe delivery of nanoparticle-enhanced radiotherapy. In summary, in this dissertation unutilized physical processes are investigated as the principle of new treatment modality (GNPT) and optimal radiotherapy techniques are determined for its gradual and safe introduction into the clinic.

# INDEX

<a href="#">ACKNOWLEDGEMENTS</a>	9
<a href="#">CURRICULUM VITAE</a>	10
<a href="#">SUMMARY/ ABSTRACT (Greek)</a>	13
<a href="#">SUMMARY/ ABSTRACT (English)</a>	14
<a href="#">INDEX</a>	15

<b>Chapter I</b>	<b>INTRODUCTION</b>
------------------	---------------------

<a href="#">1. General introduction</a>	18
<a href="#">2. Monte Carlo methods</a>	
<a href="#">A] Monte Carlo methods in general</a>	18
<a href="#">B] Basic concepts of Monte Carlo techniques</a>	19
<a href="#">i] a) Random numbers</a>	19
<a href="#">i] b) Random Number Generator properties</a>	20
<a href="#">ii] Variance reduction</a>	20
<a href="#">iii] The error estimation</a>	21
<a href="#">C] EGSnrc code</a>	22
<a href="#">D] Condensed History Approximation vs Track-Structure codes</a>	22
<a href="#">i] General Background theory</a>	22
<a href="#">ii] MC Codes: limitations and considerations</a>	23
<a href="#">iii] a) CHM and track-structure MC codes in general</a>	24
<a href="#">iii] b) modeling and simulation limitations</a>	24
<a href="#">iii] c) Geometrical limitations and considerations</a>	25
<a href="#">E] Deterministic codes</a>	26
<a href="#">3. X-ray beam properties of medical linac</a>	
<a href="#">A] Medical linac accelerator in general</a>	27
<a href="#">B] External radiation therapy techniques and advances</a>	28
<a href="#">C] Standard and unflattened beam lines</a>	29
<a href="#">D] Physics of the medical linac spectrum</a>	30
<a href="#">4. Nano-dosimetry</a>	
<a href="#">A] General concept of nano dosimetry</a>	32
<a href="#">B] Physics behind dose enhancement radiation therapy</a>	33
<a href="#">C] CERT and micro/ nano -CERT applications in medical physics</a>	34
<a href="#">D] Nanoparticles as dose enhancers</a>	35
<a href="#">E] Dose enhancement studies using Monte Carlo methods</a>	36
<a href="#">F] DER vs RBE and SER</a>	39
<a href="#">G] Imaging for tracking and localizing NP</a>	44
<a href="#">H] Nanodosimetry with Monte Carlo techniques</a>	45

<b>Chapter II</b>	<b>METHODS AND MATERIALS</b>
-------------------	------------------------------

## Part A: Modification of a FFF for IMRT

<a href="#">1. Monte Carlo simulation of the medical linac</a>	
<a href="#">A] Verification of the linac model in general</a>	47
<a href="#">B] MC model verification for FFF vs. STD linac</a>	48
<a href="#">i] Commissioning flowchart</a>	48
<a href="#">ii] EGSnrc code simulation parameters</a>	49

iii] Commissioning of STD linac.....	50
iv] Commissioning of model for IMRT.....	50
v] Commissioning of model for out-of-field area.....	51
vi] Commissioning of FFF linac.....	52
<b>2. Beam line modification.....</b>	
A] Modifying the energy of the FFF linac.....	53
B] Flattening of FFF beam by de-focusing the electron beam.....	53
C] Unflatness of FFF linac.....	54
<b>3. Treatment planning with the mFFF linac.....</b>	
A] General concept.....	55
B] Treatment planning commissioning for FFF /mFFF.....	56
C] Modification functions.....	57

## **Part B: Clinical spectra production and analysis**

<b>4. Clinical spectra.....</b>	
A] Clinical scenarios for photon spectra.....	57
B] Spectrum-weighted dose metrics.....	60

## **Part C: Optimal beam quality for NPRT**

<b>5. DER for clinical spectra - optimal beam quality for NPRT.....</b>	
A] General Methodology – spectral reconstruction methods.....	61
B] Deterministic and Monte Carlo simulations.....	62

## **Chapter III**

## **RESULTS**

### **Part A: Modification of a FFF for IMRT**

<b>1. Monte Carlo simulation of the medical linac.....</b>	
A] MC model verification for FFF vs. STD linac.....	64
i] Commissioning of STD linac.....	64
ii] Commissioning of model for IMRT.....	66
iii] Commissioning of model for out-of-field area.....	68
iv] Commissioning of FFF linac.....	68
<b>2. Beam line modification.....</b>	
A] Modifying the energy of the FFF linac.....	70
B] Flattening of FFF beam by de-focusing the electron beam.....	71
C] Unflatness of FFF linac.....	76
<b>3. Treatment planning with the mFFF linac.....</b>	
A] Treatment planning commissioning for FFF /mFFF.....	77
B] Modification functions.....	79
C] Modification function application.....	80

### **Part B: Clinical spectra production and analysis**

<b>4. Clinical spectra.....</b>	
A] Clinical scenarios for photon spectra.....	82
i] Spectral variations inside the irradiated field.....	82
ii] Spectral variations outside the irradiated field.....	84
iii] Spectral variations for IMRT fields.....	85
iv] Spectral variations due to heterogeneities.....	87
B] Spectrum-weighted dose metrics.....	88
i] Dose variations.....	88
ii] The impact of beam quality on the dose.....	89



<b>Part C: Clinical spectra production and analysis</b>	
<b><u>5. DER for clinical spectra - optimal beam quality for NPRT</u></b> .....	
<u>A] Monoenergetic beam calculation</u> .....	93
<u>B] Comparison of different clinical scenarios</u> .....	94
<b>Chapter IV</b>	<b>DISCUSSION</b>
<b>Part A: Modification of a FFF for IMRT</b>	
<b><u>1. Monte Carlo simulation of the medical linac and modification of the head assembly</u></b> .....	
<u>A] Monte Carlo model validation</u> .....	98
<u>B] Model of MLC</u> .....	99
<u>C] Modification of the FFF linac</u> .....	100
<b>Part B: Clinical spectra production and analysis</b>	
<b><u>2. Clinical beam quality and beam perturbation</u></b> .....	101
<b>Part C: Clinical spectra production and analysis</b>	
<b><u>3. DER for clinical spectra - optimal beam quality for NPRT</u></b> .....	104
<b>Chapter V</b>	<b>CONCLUTIONS</b>
	107
<b>Chapter VI</b>	<b>PhD OUTCOME</b>
	110
<b>Chapter VII</b>	<b>FUTURE GOALS</b>
	111
<b><u>APPENDIX</u></b>	112
<b><u>REFERENCES</u></b>	115

# **I. INTRODUCTION**

## **I.1. General Introduction**

This dissertation is divided into 6 chapters. In the first chapter a brief introduction to the Monte Carlo methods, x-ray beam properties and nanodosimetry are presented. The introduction gives the basic theoretical knowledge and concepts used in the dissertation. The second chapter introduces the methodology and the main concepts which were our contribution to the dissertation. It is divided into five sub-chapters. The first three describe the first major goal mentioned in the abstract. The last two describe the methods and materials of the last two major goals of the dissertation. The third chapter presents the results of the dissertation. The structure of the results is the same used in Chapter 2 for convenience and consistency reasons. The same structural sequence is followed in Chapter 4 as well, which is devoted to the discussion of the results. In the last two chapters conclusion, outcome of the PhD and future goals are presented.

## **I.2. Monte Carlo methods**

### **I.2.A Monte Carlo methods in general**

In 1949 Ulam and Metropolis introduced Monte Carlo (MC) method by publishing a paper with the title “The Monte Carlo Method” [1]. In the development stage of the method John von Neumann also played an equal important role. This method was used since then for studying a wide range of problems, from particle transport to economical theory, as well as in many other fields.

If we want to give a general definition of the method we could say that MC method represents an attempt to model physical processes by directly sampling the essential dynamics of a system described by probabilistic equations. So someone could argue that MC is a solution to a macroscopic system through simulation of its microscopic interactions. Fundamental component for deriving such a solution is the randomly sampling of the relationships or the microscopic interactions of the system until the result converges. Thus, the mechanism of executing a solution involves repetitive action or calculation steps. The fact that many microscopic interactions can be modeled mathematically makes it possible for the repetitive solution to be executed on a computer, using specific algorithms.

The system under analysis may have a probabilistic or statistical nature, meaning that the MC formulation will be a straightforward simulation, or it may have a deterministic or analytic nature, in which case an appropriate MC formulation may require some imagination and may appear contrived or artificial.

MC techniques in this field are useful for predicting the trajectories of high energy particles through detectors and other complex assemblies of materials. In this case theory cannot provide a sufficient precision or an analytical mathematical description of the microscopic and macroscopic physics. Theory can, however, provide intuition for the design of the measurement. MC methods are an adjustment to this process and they can serve in the analysis of the experiment and in the verification of the design [2].

## **1.2.B Basic concepts of Monte Carlo techniques**

Any system which is represented (or can be represented) by a probability distribution function can be simulated with the MC method. The main parts of the MC method are:

- i) The random number generator (RNG)
- ii) The variance reduction techniques
- iii) The probability distribution function
- iv) The sampling technique of the probability distribution function
- v) The error estimation

The focus of the current dissertation will be in MC methods for radiation transport of ionizing radiation (x-rays). The following section analyzes all of the above points. Further details are going to be given only for the first two points and for the last one as well. RNG and variance reduction techniques are important parts of the method, which all users of MC transport codes, regardless of their level of experience, have to treat with caution. A few more things will also be mentioned for the error estimation methods for reasons similar with the above [2, 3].

### **I.2.B.i.a Random numbers**

In order for the MC calculation to be accurate, large supplies of high quality random numbers are required. A random number could be any particular value of a continuous random variable distributed on the unit interval. The qualification for high quality arises from the special concern about the randomness of commonly used random number sequences. The quality of a supposedly random sequence of numbers can be established only after a very careful analysis, aimed at discovering patterns in random number sequences. The larger the number of tests satisfactorily passed and the higher the level of sophistication of these tests, the higher the quality of the sequence is.

This brings us to the deterministic production of random numbers using mathematical algorithms (pseudo random numbers). Each number  $\xi_i$  is produced according to the equation:

$$\xi_i = (A\xi_{i-1} + B) \text{ modulo } M \quad (1)$$

Where  $A$  is a multiplying factor,  $B$  is a constant and modulo  $M$  is the algorithm.  $M$  is selected to be equal to  $2^b$ , where  $b$  is the number of bits needed to represent an integer number.

The “pseudo” random number generator (RNG) is the core of a MC simulation. It generates the random nature needed for a MC simulation in order to imitate the true stochastic or random nature of the simulated system. The number of distinct elements produced before any of them are repeated, is called period. If the period of a sequence is very large, this periodic behavior loses its importance. The other required characteristics of a proper RNG besides having long period are uniqueness, uniformity, and efficiency [2, 3].

#### **I.2.B.i.b Random number Generators Properties**

The properties that RNG's must have in order to be considered reliable are:

##### a) Uncorrelated Sequences:

The sequences of random numbers should be serially uncorrelated. This means that any subsequence of random numbers should not be correlated with any other subsequence of random numbers. Most especially  $n$ -tuples of random numbers should be independent of one another.

##### b) Long Period:

The generator should be of long period (ideally, the generator should not repeat; practically the repetition should occur after the generation of a very large set of true random numbers).

##### c) Uniformity:

The sequence of random numbers should be uniform, and unbiased. That is, equal fractions of random numbers, should fall into equal 'areas' in space. For example if random numbers on  $[0, 1)$  are to be generated, it would be poor practice if more than half were to fall into  $[0, 0.1)$ , presuming the sample size is sufficiently large. Often when there is a lack of uniformity, there are  $n$ -tuples of random numbers, which are correlated. In this case the space might be filled in a definite, easily observable pattern. Thus, the properties of uniformity and uncorrelated sequences are loosely related.

##### d) Efficiency:

The generator should be efficient. In particular, the generator used on vector machines should be vectorizable with low overhead. With minimal effort, random number generators can be implemented in a high level language such as C or FORTRAN, and be observed to consume well less than 1% of overall CPU time over a large suite of applications [2, 3].

#### **I.2.B.ii Variance Reduction**

The name ‘variance reduction’ can be justified as follows. When comparing two different MC procedures used to estimate the same quantity, it is convenient to assign efficiency to each one.

Intuitively, this efficiency should increase for example, as the amount of time (computing time) required for each trial decreases and also should increase as the variance associated with the estimate decreases (all MC estimates have an inherent sampling variance). Thus if  $\varepsilon$  denotes the efficiency of a MC procedure, then:

$$\varepsilon \approx \frac{1}{t\sigma^2} \quad (2)$$

Where  $t$  is the amount of time required to complete one MC trial and  $\sigma^2$  is the sampling variance associated with the estimate of the quantity of interest. Since  $t$  is essentially determined by the computer being used, it is not generally profitable to consider increasing  $\varepsilon$  by conceiving ways to reduce it. This fact draws our attention to a search for general ways to increase  $\varepsilon$  by reducing  $\sigma^2$ . Some variance reduction techniques are relatively straightforward but most of them require the use of advanced statistics. Control varieties, antithetic varieties, Russian roulette, forced interactions, particle splitting; range rejection, transport cut-off, importance sampling and stratified sampling are some examples of variance reduction methods [2, 3].

### I.2.B.iii The error estimation

Error estimation in MC techniques is a fundamental concept as without it results can be meaningless and inconclusive. That is even more important as MC techniques are widely accepted by the scientific community but sometimes in an axiomatic way.

Simulations assume that there is scoring or tallying variable  $T(x)$ , where  $x$  is a range  $x_0 \leq x \leq X$  and a probability distribution function  $p(x)$ .  $T(x)$  and  $p(x)$  are related with the equation below:

$$T(x) \, dx = x p(x) \quad (3)$$

Moreover, simulations assume that the distribution  $p(x)$  has a true mean ( $\mu$ ), which is correct for most of the cases as there are tallies with no mean. So the question is what should be the value of  $N_{lv}$ , representing the number of MC histories, in order for the tallying variable to reach  $\mu$ ?

Mathematicians answered that question with the following statement *“Irrespectively from the shape of  $p(x)$  distribution the estimate of its mean will be normally (Gaussian) distributed and that the width of this distribution narrows with increased sampling”*. This statement agrees with the fundamental intuitive concept of MC techniques which is the following: *“the longer the computations time the more the convergence of the expected mean”* [2].

Finally, it is very important to say that the true mean value  $\mu$ , as well as its variance  $\sigma_x^2$  are not available to us and they have to be estimated. MC simulation calculates the estimated mean  $\bar{X}$ , which is an estimate of  $\mu$ , and its variance  $s_x^2$ , which is an estimate of the true variance  $\sigma_x^2$ . Below are the general equation used by MC codes.

- Mean value  $\bar{x}$ :

$$\bar{x} = \frac{1}{N_h} \sum_{i=1}^N x_i \quad (4)$$

- Variance associated with the distribution of  $x_i$ :

$$s_x^2 = \frac{1}{N_h - 1} \sum_{i=1}^n (x_i^2 - \bar{x}^2) \quad (5)$$

### **I.2.C EGSnrc code**

In this section some general information for the EGS MC code will be presented. The reason for this is dual. Firstly, it was the main code used either as the reference or benchmark for the usage of other codes or as primary code. Secondly, it is one of the most commonly used MC codes in Medical Physics. EGS stands for Electron-Gamma-Shower and is a general purpose package for the simulation of electrons, positrons and photons in an arbitrary geometry for particles with energies from 1 -10 keV to several hundreds of GeV. EGS system has a structured set of subroutines, which handles all of the physics in the simulation in such a way that give great geometrical flexibility benefits to the user, without touching the underline core of the code [4, 5]. EGS and its user interface OMEGA PROJECT are user friendly, with capability of simulating radiation transport of electrons (+ or -) or photons in any element, compound, or mixture, fast and considered to be a golden standard when it comes to dose calculation in radiation therapy [6]. Comparison of the EGSnrc code versus others will be further discussed in a following section.

### **I.2.D Condensed History Approximation vs Track - Structure codes**

#### **I.2.D.i General Background theory**

Photons interactions are simulated with accuracy one-by-one. However, in the case of electrons the simulation is more complex and challenging. The reason for this is the nature of the charged particle interactions.

Let us consider the case of an electron. The mean-free path of electrons, for example in oxygen, for relativistic energies (e.g. ~1MeV) is  $\sim 10^{-5}$  to  $10^{-4}$  g/cm<sup>2</sup>, taking into consideration various possible processes such as elastic, ionization, excitation or Bremsstrahlung. If these ranges are translated into number of interactions, then we conclude that an electron undergoes  $\sim 10^5$  -  $10^6$  interactions before slowing down. This means that a similar number of electron steps must be simulated for each MC history. As can someone naturally observe that is a very challenging and time consuming process [7].

The technique which solves the aforementioned problem is called Condense History Electron Transport and the MC codes using it are called Condensed History Method codes (CHM), introduced at 1963 by Berger [8]. The basic idea behind this method is that only few of the many interactions of each electron are causing significant directional changes or energy loss. Due to this fact, it is possible for small interactions to be combined into one larger effective one.

CHM has to solve two separate problems: a] the energy loss of each electron and b] the change of its direction. Fortunately, these two processes can be handled separately, as angular deflections do not lead to energy loss, and at the same time energy loss produces very little angular deflection. That makes the development of the technique easier during its initial phase. For the calculation of the energy loss Continuous Slowing down Approximation method is being used (CSDA) which is characterized by the stopping power or by distributions that are a function of the length of the electron path. The change of direction is being handled with the use of the “any-angle” theory introduced at the beginning of 1940’s [9, 10]. A stronger theoretical support of the CHM was accomplished when it was proved that the method converges at the exact solution of the Boltzmann transport equation in the limit of a small electron path-length. The same proof revealed that CHM is an approximation method with limitations, and can lead to wrong results if it is being used outside of its validity range [11]. After that a lot of efforts have been made to develop new and more accurate CHM algorithms.

MC codes which are using the above method are called CHM codes, whereas codes that are tracking all the interactions that charged particles are undergoing are called track-structure codes. Specific examples of such codes, from both categories, are going to be discussed in the following section. Moreover, specific limitations and challenges of the MC technique for radiation transport are going to be presented.

#### **I.2.D.ii MC Codes: limitations and considerations**

In the case of MC simulations there are two different uncertainties affecting significantly the outcome of the results. The first type of uncertainty is related to limitations of the physical model used to simulate a physical process (e.g. cross section data of a single electron loss by capture). The second type of uncertainty is related to limitation of the MC method itself. MC method generally is a numerical method which is being used to simulate the physical world. For an accurate simulation the particle transport position and the momentum of each particle must be known with accuracy. Below 1 keV quantum mechanics becomes more and more dominant and the position and the momentum of the particles are not known with accuracy. MC codes cannot take into account these effects due to the way that the method works, something that leads to uncertainties. These uncertainties might increase even more if we take into account the limitation of some codes regarding geometrical modeling of the simulated structures.



Cross sectional uncertainties are not negligible especially below 1keV. At this point it should be mentioned that in many studies collaboration of different codes is being used. Something like that is not a trivial task, as a lot of fine tuning between the codes is required, leading to higher complexity and adding more systematic errors at the overall process.

#### **I.2.D.iii.a CHM and track-structure MC codes in general**

Up until now there are many MC codes developed to solve dosimetrically problems. The most commonly used codes are EGS4/EGSnrc [4], MCNP [12], PENELOPE [13] and GEANT4 [14] and GEANT4-GEANT4-DNA [15] as well as some other codes which are dedicated to treatment planning like VMC++ [16]. These codes were used for a broad spectrum of applications, from radiation therapy and imaging to nuclear medicine. Regardless of the exact characteristics of each dosimetric project, MC code applications can be divided into two general research areas of interest: microdosimetry and micro- or nano- dosimetry. The differences between the two areas are the size of the volume in which dose is being scored, and the treatment of physical quantities. Macrodosimetric scoring is related with volumes of at least millimeter size, which can be translated to energy range of >1 keV. MC codes working at macroscale applications are well established while their agreement has been tested through many different applications, measurements and experiments. Some of the above are summarized in two review papers by Rogers [17] and Spezi and Lewis [18] as well as in one task group (TG-105) [19].

Micro-dosimetry or nano-dosimetry applications are simulating dose deposition to a micro or nano scale volumes. MC applications at this level present an increasing interest to researchers, as dose deposition at this scale is extremely important for potential damages to cellular and sub-cellular targets such as DNA, cell membrane etc. Recently, GEANT4 [14, 15] and PENELOPE [13] codes were the two general purpose codes, which extended their ranges and their geometrical modeling tools in order to simulate sub 1keV energies and nanodosimetric structures. GEANT4-DNA [15] package was added to the original version of the code, so that the code can simulate electrons down to 8.23 eV [20] while the threshold for ionization is fixed at 12.61 eV [21]. On the other hand PENELOPE can simulate particle transport down to 50 eV [22]. Traditionally simulations like these were performed with codes specifically created for these types of simulations. The most commonly used are OREC/NOREC [23], TRION [24], ETRAN, [25] but others have been also created from Emfietzoglou et al [26].

#### **I.2.D.iii.b Modeling and simulation limitations**

As previously mentioned, MC codes can be divided into CHM and track structure codes. CHM codes are general purpose codes such as EGSnrc and MCNP etc., whereas track-structure codes have been mentioned in the previous section. CHM method presents huge computational



benefits for the simulation, as the simulation time decreases significantly. Though this approximation method is accurate for macroscopic simulations, in the case of microscopic and nanoscopic simulations this method breaks down, because the particle tracks, which need to be detected, are much smaller [27].

Track-structure codes or event-by-event codes are following each particle separately for its full track. These codes exist for a few decades and they have a big contribution on the understanding of several physical processes [28, 29]. Due to this event-by-event codes computation time is much larger compared to the CHM codes. Because of this, they do not have any advantage for macroscopic applications but they are much more accurate for micro- / nano - scopic studies. Most of these codes are only valid for water (liquid or vapour) at the moment, a fact that limits their use. Liquid cross sectional data can be used for biological structures such as DNA's double helix, only if we assume that it is made from water. For macroscopic simulations assuming that different structures are made of water, is a valid assumption but for microscopic targets it is not an accurate approximation. In case of studies about the biological or the dosimetrically micro- / nano-scale enhancement, due to the presence of high-Z materials, correct use of cross sectional data is essential for obtaining reliable results. For sub-1 keV energies cross sectional data uncertainty is even up to 40% [20].

Furthermore, as it was mentioned by Thomson and Kawrakow [30] accuracy of the simulation is not only depended on the proper crosssectional data. Sub-1 keV simulations are facing validation issues. MC simulation is using a "classical" approach of physics, in which the location and momentum of each particle are known with accuracy. In reality, quantum theory dictates that particles position and momentum uncertainties should satisfy Heisenberg's uncertainty principle ( $\Delta x \Delta p \geq h/2\pi$ ). As long as these uncertainties are negligible compared to the actual momentum and relevant length scale of the particle steps, the classical approach is accurate. When these uncertainties cannot be neglected anymore the classical approach breaks down, so MC methods are not describing accurately particle transport. As it was shown [30] for 1keV electrons in liquid water uncertainty is already 5%, at 100 eV is 17 - 20% and for energies around 20 eV is ~50%.

#### **I.2.D.iii.c Geometrical limitations and considerations**

The development of different tools which were used for building different geometries, helped MC simulations to significantly reduce uncertainties coming from various geometrical simplifications of the problems. Geometrical modeling is of great importance when nano-structures are simulated, as the path length of the particles is not negligible compared to the size of different structures. Up until now most of the studies in literature are modeling cellular and sub-cellular structures by using general shapes like cubes, cylinders etc [31 - 33]. There is one study modeling specific structures in a sub cellular level with high accuracy [22]. Even in that

case, uncertainties during the calculation could not be neglected as in most of the cases the assumption made was that all structures are liquid water based. This assumption is generally true for larger scale modeling, but at a sub-cellular level is not so accurate, because other materials of different density and properties (e.g. fat) are present.

Conclusively, it can be said that MC simulations in micro-/ nano- scale are facing two sources of uncertainties originating from the cross section data used and from limitations of the method itself. The cross section data present uncertainties based on the material and energy area used. Furthermore, a separate type of uncertainty is introduced by the user as well, due to limitations of the computational model.

### **I.2.E Deterministic codes**

Deterministic methods are applied in addition to MC methods when simpler geometry allows their application. Their potential advantage is the speed of computations for 1D or 2D or some other special problems. These methods are based on giving numerical (deterministic) solutions to Boltzmann equation and can provide a description of the particle transport as the MC method does [34 - 36].

One of the first general-purpose coupled electron-photon discrete ordinates transport code was CEPXS/ONELD produced in 1989 [35]. CEPXS effectively converts the conventional discrete ordinates solution of the Boltzmann equation into a solution that uses the restricted CSDA to represent soft inelastic reactions both collision and radiative of electrons and positrons. The main assumption of the CEPXS/ONEDANT deterministic calculation is that the target can be represented in one-dimensional geometry, which allows very fast computer runs. The 1-D slab model computes the transverse-integrated flux as a function of depth in target for the actual pencil beam source. This solution is also equivalent to one in which the electron beam from the accelerator is modeled as an infinite planar source incident on a slab target region, rather than a pencil beam source on a finite size target [34 - 36].

Deterministic codes are much faster than MC codes and this is their main advantage as they can give a precise solution with less computational cost. Their speed difference can be orders of magnitude different dependent on the application. On the down side, more computational memory is required, especially for multi dimensional calculations. The main disadvantage of these codes, compared to MC ones, is their inability to give continuous results of the energy, angle and position of the particle. These codes find a solution for a predefined mesh of points by solving the Boltzmann transport equation from one point to the other. Moreover, they primarily provide information on the particle flux, but this can be used to calculate other quantities such as dose and yield as well [34].

## **I.3. X-ray beam properties of medical linac**

### **I.3.A Medical linac accelerator in general**

The past few decades the linac is one of the leading modalities used for external radiotherapy. Linac technology and design developed through time and lead to more accurate and faster treatments as well as to the developments of new RT treatment techniques.

MC simulation played an important role in the development stage of linacs, as well as in the improvement of their performance. That is because MC is a thorough, reliable and sometimes the only way to identify possible physical problems. Moreover, it is a very helpful tool that can be used at the design stage of new modalities by testing new ideas, even if the machines do not physically exist.

Regardless of the delivery technique and the linac type, most of the assembly of the linac head is similar. Below the level of the bending magnet and the electron gun there is the target, the collimation component (primary, secondary and ring collimators), the beam modulation components (jaws, MLC, SRS cones, SBRT cones, flattening filter or scattering foils etc) the ionization chambers and the mirror.

The mentioned parts vary in terms of geometrical features and material composition even for the same machine models. Detailed knowledge of the geometry, dimensions, composition as well as energy characteristic of the electron beam hitting the target, are essential for an accurate MC simulation of particle transport through the head assembly. That is why blue prints of the linac must be provided from the manufacturer. Unfortunately, the accuracy of the blue prints is questionable on many occasions. There are many reasons for that but two are considered to be the most important ones. The first has to do with the fact that most of the blue prints were not originally created in a systematic way according to the needs and potential challenges of a MC simulation. In fact, more accurate blue prints have been generated upon the demand of MC users, especially the past decade. The increasing demand of more accurate models and the number of researches using MC techniques, lead the manufactures to improve and sometimes to correct their blue prints. Recent blue prints are more and more MC oriented. The second reason has to do with the “uniqueness” of each machine. There are more than one ways to tune a machine to a certain output, so more than one possible model may fit a particular linac output.

Among other linac head elements the flattening filter is the most important one, presenting a vast design variety and simulation complexity. More details about assemblies with and without the flattening filter are going to be discussed later on. The following chapter will deal with the variety of the modern external radiation therapy techniques without getting into many details, as these are concepts well spoken and written through literature in the scientific community over

the past years. The final chapter of this section will discuss some basic concepts of the output spectrum of a medical linac and its underlying physics.

### **I.3.B External radiation therapy techniques and advances**

External radiation therapy is a general term that includes a lot of techniques and modalities. There are different ways to categorize external radiation therapy. The most general one is dividing it by particle source type. According to this we have photon, electron [7], heavy ions [37], proton [38], neutron [39] or pion therapy [40], though the most widely used are photons and electron therapies, while proton therapy is gradually gaining more and more ground. The other ones are only either in an experimental stage or limited to certain (national) institutes and treatment sites.

Because of the continuous advance of external therapy another sub-categorization must be made for each different source therapy. At this point, we will only focus on techniques used for photon therapy, as these were the main focus of the current dissertation.

The simplest technique used for photon therapy beams, regardless of the energy, is the open beam field (OB) irradiation. OB fields can be square or rectangular, centered or not and usually go from 4x4 – 40x40 cm<sup>2</sup>. The need to spare healthy tissue, surrounding the tumor, and boost the dose to the tumor has lead to the discovery of more refined beam shaping and modulation. This was a slowly progressive process in which technological advances played a very important role. However, the need for conformality leads to other techniques as Conformal Radiation Therapy (CRT) and 3D-CRT.

Newer techniques were put into clinical practice through time, which was even more oriented to specific treatment sites like brain, liver or lung. Techniques like those were Stereotactic Radiation Therapy (SRS),  $\gamma$ -knife, and Stereotactic Body Radiotherapy (SBRT). All these were based on the idea of using multiple narrow beams in one or a few fractions, which would deliver very high doses to the tumor but with a very sharp dose fall off. Finally, relatively recent advances lead to the development of more complex techniques, not only on the conceptual or delivery part but also in terms of the technology of the linacs. These techniques are Intensive Modulation Radiotherapy (IMRT), Volumetric-Modulated Arc Therapy (VMAT) and Tomotherapy. Further, details will be provided in the section of IMRT, as it is the main technique studied in the current dissertation [7].

Concluding, it has to be said that regardless of the source type and the delivery technology, there is a common ground for all the aforementioned radiotherapy techniques. This is the struggle to spare as much as possible of the healthy tissue, while increasing the dose to the tumor. This is even more difficult to achieve due the physical limitations of radiation, as interaction with matter

cannot separate healthy or cancerous tissues. Ionizing radiation in order to be delivered to the tumor has to be propagated through healthy tissues and lose ionizing energy therein. This implies that the damage from ionizing radiation occurs both in the entrance and exit regions of the beams. In addition, because of the radiation scatter, the sharpness of the treatment fields is degraded, and tissues adjacent to the tumor are irradiated with scattered radiation. Ultimately, the main problem sums up to the tumor to healthy tissue dose ratio. In order to improve and achieve better results, several ways have been employed in order to find new physical “healthy tissue friendly” processes, like the use of the sharp Bragg peak of the proton dose depth curve, or through the modification of current linac assemblies (e.g. removal of the flattening filter) to limit the head scatter, collimation of the field and conforming to the target, and improvement of the image based patient setup which allowed decreasing of treatment margins. More recent solutions to these challenges include: contrast enhanced radiotherapy, high Z nanoparticle RT (NPRT) and micro beam RT (MRT). NPRT methods rely on physical effects while MRT is based on more biological grounds. These methods will be discussed in the following sections.

### **I.3.C Standard and unflattened beam lines**

Recently, there was an interest in the clinical usage of Flattening-Filter-Free (FFF) linac. For this reason the properties of unflattened photon beams have been under re-investigation. The number of these publications increases every month, as new commercial beam lines are out in the market the past years. Removal of the flattening filter results in significantly increased dose rate, softening (and therefore decreased penetration) of the photon beam (for the same electron beam energy), decreased head scatter (and therefore decreased peripheral dose) and non-uniform (bell-shaped) open beam profile. Other noteworthy properties of FFF linac include increased surface dose and slight shifting of depth of maximum dose towards the surface. The increased dose rate for FFF linac depends on the energy of the photon beam, the material of the flattening filter, the manufacturer of the linac and the field size. Depending on these conditions, dose rate factor ranges from about 2 to 4 [41 - 60]. Increased dose rate, and therefore decreased treatment time, may minimize the possibility of intra-fractional target motion, increase treatment throughput and might potentially lead to radiobiological benefits for some tumors [61].

One of the goals of this dissertation was the investigation of crucial beam properties impacting the overall benefits of IMRT delivery using FFF linac instead of a standard linac with flattening filter (STD) linac. While the aforementioned benefits of FFF linac are clear for open beam or static MLC delivery (for instance for SRS/SBRT, which uses small fields with static field shaping), they are less clear for beams modulated with dynamic MLC (for instance for larger targets requiring dynamic modulation). The reason for this is that FFF linac intensity abruptly decreases with the off-axis distance, which can be clearly observed in larger field (>10x10 cm<sup>2</sup>) OB dose profiles. As

a result, off-axis-distance dependent compensation (modulation) is needed for delivering uniform dose to the tumor. If that modulation has to be done by dynamic MLC, then this may lead to significantly larger monitor units and therefore head (MLC) scatter (and effectively head leakage). This undesired behavior may be considerable for larger target volumes and for targets away from the central axis (e.g. such as in head and neck treatments). That will lead, at least partially, to cancelation of the original benefits of FFF linac.

Except from the recent IMRT optimization study [62], published literature on FFF has not yet fully addressed the problem of IMRT for off-axis targets or for larger volume targets. Different planning studies were published regarding IMRT for FFF linac [54, 62-66]. Most planning studies were performed for prostate cases. One of those studies indicates differences in MU efficiency between STD and FFL linac of 10-16% (larger for FFF plan) [63], whereas another study showed that for uncalibrated unflattened beams there is a MU benefit by a factor of  $\sim 2$  [64]. Other studies for head and neck cases report a 63% and  $\geq 25\%$  increase in MUs when FFF beam is used [62, 63]. However, another study reports an average increase in MUs of about 11% (for 6MV) for different cases and sites [54]. Even though, these planning IMRT studies have been reported for different treating sites, the published information is scant and cannot serve as a basis for final conclusion about MU efficiency in general cases.

One of the goals of this dissertation was to address the issue of considerable dose fall-off away from the central axis and its impact on IMRT monitor unit efficiency. For this reason we investigated an alternative linac design that resulted in a flattened photon beam emerging from the target. This beam was utilized in order to improve dynamic MLC modulation of the photon beam. Moreover, we studied the beams usefulness in terms of maximization the effective dose rate within the field and minimization of the out-of-field dose. Specifically, after characterizing the properties of FFF linac, we proposed a modified FFF (mFFF) beam line with a defocused electron beam. MC methods were used to study the impact of the altered electron beam on the flatness of the photon beam, without significantly sacrificing the aforementioned beneficial FFF beam properties.

### **I.3.D Physics of the medical linac spectrum**

The past years, the characterization and the study of the medical photon spectrum, for therapeutic and imaging applications, has received great attention which has been further increased recently [67 - 73]. The linac beam energy spectrum depends on field size, lateral location with respect to the central axis, depth, presence of heterogeneities in the patient (lung, bone etc), and the treatment technique used. Spectral variations play a role in dosimetry when energy-dependent detectors, such as TLDs, films, diode/ion chamber arrays are used [74]. Such



changes affect the response of these dosimeters, and in the case of mixed spectral content beams they may result in an inaccurate dose measurement. In addition, structural and design differences in the medical equipment or delivery techniques can lead to substantially different dosimetric beam properties.

One of the recent examples is the use of linacs without flattening filter. Using MC simulation techniques a number of investigators have studied the beam properties and characteristics of flattening filter-free linacs [41-60], as mentioned in the previous section, whereas removal of the flattening filter increases the lower energy component of the spectrum as the major beam hardening source of the linac head, flattening filter, is being removed. That change significantly alters the beam spectrum in different regions of the field and outside of it.

Despite the progress made in this area, there have been only a few studies published showing spectral changes of clinical photon beams. The main focus of these studies was to explore the problem of dose variations when energy-dependent dosimeters are used. These studies compare photon spectra for different field sizes, depths and treatment techniques [67-69]. Apart from a recent study by Scarboro et al [68], which presents an extensive investigation for different cases, the rest of the studies show limited examples of spectra.

Spectral changes in the photon fluence may also lead to changes in other clinically important properties of the beam. For instance, Titt et al [44] pointed out the dramatic difference of electron spectra at the surface of a water phantom when the flattening filter was removed. Vassiliev et al [46] showed that the depth of the maximum dose ( $d_{\max}$ ) moves 10 - 20% shallower, depending on the field size, when the flattening filter is removed. The same study calculated that the effective energy of an unflattened beam drops by about 2 MV (from 6 MV to 4 MV) compared to a beam shaped by flattening filter. This means that a PDD of FFF linac having the same nominal energy (6 MV) corresponds to a PDD of a linac with flattening filter and nominal energy of 4 MV. In order to point out the spectral changes between flattened and unflattened beams Vassiliev et al. [45] showed examples along the central axis of a nominal 18 MV beam.

Knowledge of the spectrum provides important information about the quality of the beam which can be useful for different applications, not only in therapeutic but also in imaging beams. For instance, in an attempt to improve the image quality of MV radiography, changes in the low-energy component of the spectrum for different bremsstrahlung targets and for unflattened beams were determined by several investigators [72, 73]. In other studies, attempts were made to quantify the amount of low energy particles in MV beams and their effect on dose and film response [69, 70] or the contamination of the beam by electrons and positrons [71].

One of the new areas of radiation therapy and imaging, in which spectral differences are of great importance, is dose enhanced radiation therapy with high-Z contrast agents and nanoparticles (such as iodine contrast, or gold nanoparticles). The past few years an acceleration of research

exploring techniques has been observed, which exploit the increased photoelectric absorption when materials of high-Z content have been uptaken by various tissues or cells [31, 32, 75-78]. Changes of the lower energy portion of the spectrum (e.g. < 300 keV) due to different irradiation conditions, in the regions where high-Z material is present, might have a large effect on the dose deposition at the microscopic scale while preserving the macroscopic dose level at its prescription value. Knowledge of the effective beam quality for these recently explored therapies is essential both for imaging and treatment delivery with low concentrations of high-Z elements.

Despite the recent interest in modified linac beams, there is a lack of systematic comparison of photon energy spectra among different clinical scenarios. One of the goals of the current dissertation was the presentation of a comprehensive database of clinical spectra, and the determination of qualitative and quantitative differences between these spectra, in case of STD and FFF linac beamlines for an extensive list of clinically important beams. Furthermore, an additional goal was the identification of possible clinical scenarios that might change the lower part of the spectrum (e.g. < 300 keV) area, which is associated with dose enhancement (DE) in radiation therapy and imaging.

## I.4. Nano-dosimetry

### I.4.A General concept of nano-dosimetry

Nanodosimetry is the measurement and application of nanoscale doses [79-82]. The term “*wants to emphasize the kind of measurements that are related with the energy transfer events within site of which are of the same order of magnitude as the mean interaction lengths of ionizing particles*” [81]. Dosimetric quantities at nanoscale are much different than the ones used at macroscale dosimetry. As scale decreases it more meaningful to avoid discussing about the dose, in a macroscopic way, but about the physical properties of single particle interactions (ionization, excitation, elastic scattering). In order to address the main differences between macro /-micro dosimetry and nanodosimetry two main key differences will be discussed:

1] In microdosimetry we consider a particle of energy  $E$  entering a small volume. The key quantity is energy imparted  $\epsilon$ . Imparted energy  $\epsilon$  is a stochastic quantity, whereas the absorbed dose, which is being used in macroscopic conditions, is not relevant any more. The energy imparted  $\epsilon$  to matter  $m$ , is the summation of all the energy deposits in that volume mass. So a new quantity  $z$  is defined as the specific energy imparted  $z = \epsilon/m$  [84, chapter 16, page 504], where  $m$  is the volume mass. In nano scale the main measured quantity which replaces energy  $\epsilon$  is the cluster size of the ionizations, meaning the number of ionizations for a specific area. Concluding, it can be said that microdosimetry is related with a single-event distribution of the



imparted energy  $f(\epsilon)$  while nanodosimetry with the single-event distribution of the ionization cluster size  $f(\text{cluster})$ .

2] In microdosimetry events that happened at the volume close to the volume of interest have a minor contribution to  $f(\epsilon)$ , but this is not the case for nanodosimetry as the events happening close to the area of interest are of great importance, due to the scale of the problem. As a result of the above statement, in microdosimetry  $f(\epsilon)$  can be safely assumed that it is related to the size of the area of interest. On the other hand, in nanodosimetry it is also related to the distance between an event, happening outside the area of interest, and the volume of interest as well as the range of the secondary electrons.

3] In microdosimetry mono-energetic heavy charged particles spectra are easier to describe using LET (low or high) as  $f(\epsilon)$  superimposes both high and low LET thus complicating things. In nanodosimetry the low LET component is always present (due to low energy electrons), while the high LET varies only with single-event distributions  $f(\text{cluster})$  of mono-energetic charged particles at high LET (due to primary ionizations). The variance of low and high LET depends on the distance between the event and the area of interest (affects low LET) and the volume of interest (affects high and low LET) [79-82].

#### **I.4.B Physics behind dose enhancement radiation therapy**

Dose fluctuations due the presence of high  $Z$  materials are well known for many decades [83]. The physical process behind that is the increased photoabsorbption when a material of higher  $Z$  is present, which leads to higher productions of photoelectrons, fluorescent photons and low energy Auger electrons. Photoabsorbption is directly related with the material ( $\sigma \sim Z$ ) and the energy of the incident photon ( $\sigma \sim 1/E^3$  or  $1/E^4$  depending on the energy range). A secondary effect that increases the magnitude of this effect is the production of Auger electrons, which are of shorter range [84, 85]. These electrons are the main reason of the increased dose deposition at the vicinity of the material as the produced photons are traveling longer distances and they do not contribute to the local dose [figure 1]. This phenomenon is being used in medical applications since the beginning of the '80s [86].

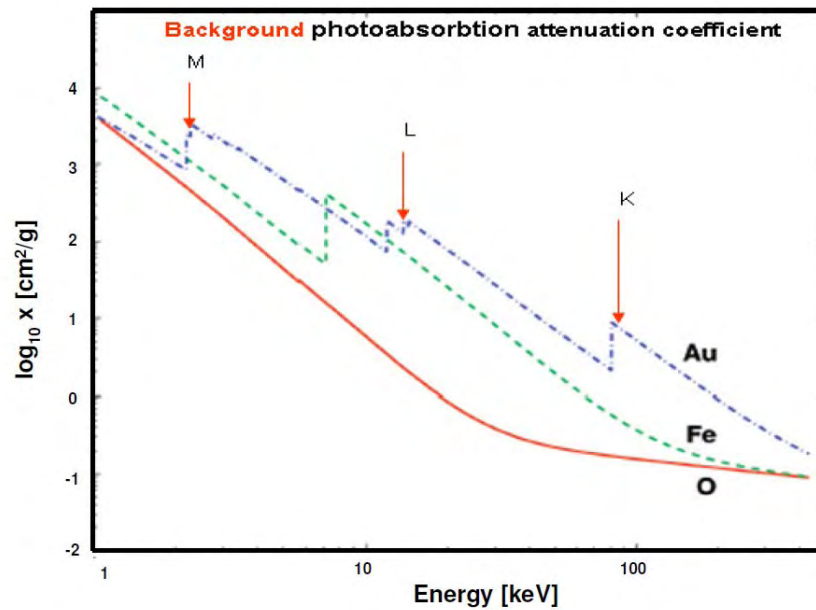


**Figure 1:** Photoabsorption attenuation coefficient versus energy for three different elements: gold (Au), iron (Fe) and oxygen (O). The figure shows the increase of the attenuation coefficient value for K, L, M shells.

#### **I.4.C CERT and micro/ nano-CERT applications in medical physics**

DE effect might present desired or undesired results. An undesired effect is the increased dose deposition which was noticed in cases of patients with implants or due to the hardware materials of the CT scans. On the other hand, proper use of this process could also dosimetrically benefit patients, as it can increase the dose deposition in the treatment area. The use of this effect leads to a potential treatment modality named contrast enhanced radiation therapy (CERT). For example CT contrast agents, such as iodine, with proper use can benefit dosimetrically the patient [86].

One of the new emerging technologies of the past ~15 years is nanotechnology. If this can be combined with the DE effect around high-Z materials, it could potentially lead to new techniques which will help to eradicate cancer [31, 32, 75-78, 87-99]. The combination of nanotechnology with dose enhancement effects could increase cell kill at micro or nano distances away from the nanoparticle. In micro or nanoscale the deposited energy due to a nano- high Z material is mostly related with the low energy Auger electrons (most probable energies are < 500 eV or ~25 nm range [85]), which have high LET compared to photoelectrons or Compton electrons. The Auger effect occurs within sub  $\mu\text{m}$  distance. Above that range and up until a few hundred of  $\mu\text{m}$ , photoelectrons (depending on the energy of the incident beam) are the dominant sources of energy deposition. DE drops with distance from the nanoparticle. DE for those cases might not be noticeable at the macroscale dose deposition, but leads to a substantial dose deposition increase at the nanoscale [75].

#### **I.4.D Nanoparticles as dose enhancers**

Through the years different materials were proposed as dose enhancers. The main ones are Iodine (I), Gadolinium (Gd), Gold (Au), Tungsten (W) and Bismuth (Bi). One of the most important dose enhancers used for therapeutic or imaging applications is gold. Gold has an atomic number of  $Z=79$ , but most importantly it is biocompatible so it can be used for medical applications [75, 76, 87]. Hainfield et al [100] were the firsts showing the effect in vivo, following the initial in vitro study by Regulla et al [101]. Up until now there are a lot of studies which are trying to characterize the impact of DE for a broad spectrum of conditions [31, 32, 75-78, 87-99]. These conditions are mostly related to the beam quality for selected kVp and MV beam as well as the characteristics of the nanoparticle, such as size, position of the particle, material of the nanoparticle and distance from the target. Different studies tried to demonstrate, in both an experimental and theoretical way, DE effects for kVp and MV spectral x-rays sources. Among theoretical techniques are the ones based on MC simulation [31, 32, 75-78, 87, 88, 92-94, 98, 99], as well as approximation models based on electron range tables [89-91]. Experimental techniques include cell survival data, imaging studies showing uptake by the tumor cells and other cells (e.g. endothelial) [87, 89-91, 95-99]. These studies have shown that GNP are forming clusters, regardless of their macroscopic biodistribution [94], therefore a cluster of GNPs at a cell membrane or inside the cell might be more appropriate than a single GNP model, irrespective of the macroscopic biodistribution.

Even though DE was demonstrated for various in vivo and in vitro scenarios as well for various clinical irradiation conditions, literature leaves a lot of questions open to be answered in the future, as well as many things to be clarified and separated. Measured, calculated or simulated DE does not always have the same meaning in various published studies. For example in some publications [31, 76, 92, 93] dose enhancement ratio DER is presented as a relative value ratio between dose with high-Z material present versus dose to water, as for other publications DE is presented as a ratio of other quantities, like interaction enhancement ratio etc. [87, 89-91]. Moreover, there is a big spectrum of geometrical setups, nanoparticles (NP) sizes and shapes, measured quantities which are related directly or indirectly to DER and initial irradiation conditions. All these factors can be misleading and might lead to results with large discrepancies. Furthermore, technical imaging limitations, which do not allow an accurate determination of the exact position of the NP with respect to the nano-target, increase the complexity of these studies. Finally, it is of great importance to link between published DER values and the actual increase of cell death when NPs are present.

#### **I.4.E Dose enhancement studies using Monte Carlo methods**

As described in a previous section, MC method can be a very valuable dosimetric tool. Up until now many authors used MC in order to identify and calculate DE effects under different conditions [31, 32, 75-78, 87, 88, 92-94, 98, 99]. Table 1 below summarizes the main points of all the published papers which used MC simulation to calculate DERs.

Cho et al. [75] were the first authors, which tried to calculate the dose deposition change when GNPs are present. Their first study was performed on a macroscopic scale. They assumed different concentration of gold inside a water-tumor volume and they calculated the dosimetric differences for various beams, energies and gold concentrations below that volume. The MC codes used were EGSnrc for the MV beams (6 and 4 MV with and without flattening filter (FFF)) and MCNP (for a 140 kVp beam). The source size was a 4x4 cm<sup>2</sup> spectral source for all cases, while target sized varied with the energy, larger for MV beams. Water - gold material was simulated with different concentration of gold (7, 18 and 30 mgAu/gr tumor) by assuming that gold concentration is uniform for all the tumor (water equivalent) volume. DER for these macroscopic calculations was calculated as the ratio of the absolute value of dose when water - gold is present versus dose for just water. The largest DER ~5.6 was measured for 140 kVp beam and for the largest concentration of 30 mgAu/gr tumor. For MV beams the DER shows an increase of dose from 1 to 5% dependent on the concentration.

Cho et al [76] and Jones et al. [31] used a similar technique to calculate microscopic DER for various beams. The method of the set up was the same as the one described in the study previously mentioned (add reference). A water equivalent tumor was modeled of 3x3x3 cm<sup>3</sup> (kVp and brachytherapy beams) and 2x2x3 cm<sup>3</sup> size (6 MV linac beams). Set up for the MV case was the same as in the previous study, whereas for the rest of the beams a spectral source of 0.01x0.01x1 cm<sup>3</sup> was placed at the center of the simulated volume. Cho et al used 7 and 18 mgAu/ gr tumor for all the simulations while Jones et al used only 7 mgAu/ gr tumor. In order to calculate microscopic DER (mDER), a combination of MCNP and EGSnrc MC codes was used along with NOREC code [23]. The latest, as mentioned in a previous section, is a track structure code capable to track each electron separately down to 100 eV. The smallest value of mDER was calculated for 6 MV beam. MV mDER was about 8, for the first 1µm from the Au-water material, and dropped about 50% for the next 100 µm. The largest values of ~1000 were calculated for Yb-169 (average energy ~93 keV) with the value dropping ~100 times after 10 µm. The smallest the average energy the highest the effect was, and the fastest mDER had been reduced with distance from the surface of the Au-water material.

F Van den Heuvel et al [77] calculated the DER for different monoenergetic beams from 0-200 kVp when 1mm slab of Au-water uniform material was present in a water phantom. Au

concentration from 0-10% was used for all the used energies. Monoenergetic beams were of the same size as the phantom surface. For comparison purposes a spectral beam of 110 kVp was used with the monoenergetic beams. For all the simulations the MCNP code was used. The results showed that the larger the concentration, the larger the calculated DER was. The largest values were calculated for 10% concentration of Au and showed that DER increases from 0 - 11 as energy goes from 0 – 60 keV. After 60 keV DER decreases with the exception of the energy of 80 keV, at which DER increases by ~10% compared to each neighbor points. The reason for that was that this energy is around the energy of the K edge shell photoabsorption. For 200 kVp DER had a value of 2. Spectral beam had a value of 8 for the same measured conditions. In the same study DER was also calculated for an OAR profile as a function of energy. DER values for the latest case followed a totally different pattern with DER being larger (~20) for the smallest energy, and were reduced to a value of ~4.5 as energy increased to 200 kVp energy. For that same case DER of the spectral beam was larger than the previous and its values increased from 8 to ~13.5.

M. K. K. Leung et al [32] and E. Lechtman et al [78] tried to calculate mDER not by simulating material of different concentration of Au but by looking the DER at the vicinity of a GNP. They used different spectral beams, external and brachytherapy ones, of an energy range from 21 keV (Pb-103 source) to 6 MV photon beams. For the case of external beams (6 MV, Co-60, 50 kVp, 250 kVp and 300 kVp) a source of the size of the GNP diameter was simulated and dose was scored at the surface of the GNP. DER was calculated as a ratio of dose with and without the presence of the GNP. For brachytherapy sources (Ir-192, Yb-169, I-125 and Pb-103) the spectrum of the source was placed on the center of the GNP and DER was calculated again in the same way as above. In order to calculate the effect of the GNP size, different sizes of 1.9, 2, 5, 30, 50 and 100 nm were tested.

Leung et al [32] used GEANT4 code [14] and calculated the interaction enhancement ratio for different GNP sizes and source energies. According to their results interactions were increased by a factor of 1000 for the lowest simulated energy (50 kVp) while an increase of at least 10 times remains even for 6 MV and Co-60 beams. Regarding the GNP size there is no big discrepancy between the smallest size used (2nm) and the largest one (100 nm) but there is an increase on the interaction ratio as GNP size decreases.

Lechtman et al [78] used MCNP5 for the macroscopic part of the simulation and PENELOPE [27] for the microscopic one. They calculated the relative DER for different energies and GNP sizes (1.9, 5 and 30 nm) with distance from the surface of the GNP. The larger the GNP the larger the relative DER values were, while as the energy of the source increases the relative DE affects larger GNP surrounding areas.

McMahon et al [92, 93] and Rahman et al [94] calculated DER for different sources. Energies ranged from 20 – 160 kVp (photons – kV range), 6 and 15 MV and electron beams of 6 and 12 MeV. GNP sizes ranged from 1.9 – 50 nm while Rahman et al assumed GNP size of 1.9 nm and concentration of 0.25, 0.5 and 1 mM of gold. Both used GEANT4-DNA MC code [13, 15]. McMahon et al showed that the relative ratio of dose deposited in water per ionization for different energies and nanoparticle sizes. Rahman et al [94] calculated DER values which were greater for the lower photon beams (80 kVp) and for the largest concentration (1mM). Values for GNP size of 1.9 nm were up to 24.6 (80 kVp – 1 mM) while the smallest (1.4) were for 0.5 mM – 150 kVp. Electron beams had smaller fluctuated values of DER, varied from 2.7 (6 MeV – 0.25 mM) to 4.1 (12 MeV – 1 mM).

W. Ngwa et al [89, 90] and R. I. Berbeco et al [91] calculated mDER for 6MV FFF and unflattened beam, and for different brachytherapy beams. The calculation was not based on MC code simulation, but used an analytical method based on electron tables and a model by Makrigiorgos et al [102]. The target size was 2x2x10  $\mu\text{m}^3$ , while a 100 nm size GNP was used for the calculation. Different concentrations were used in a range of 0 - 50 mg/gr for MV beams and 0 – 350 m/gr for brachytherapy sources. The calculated mDER was maximum (1.16) for the MV beams and for 50 mg/gr concentration range, while for the brachytherapy beams maximum values were calculated for a Pb-103 source and were ~20 for the maximum concentration used 350 mg/gr.

**Table 1:** Sum of the published DER values using MC techniques with information regarding the energy and the size of the source, GNP concentration or GNP size used and MC code used.

Author	energy & source	source information	target size	concentration of Au (mgAu/ gr tumor)	DER	MC codes		
S. H. Cho (2005)	140 kVp	4x4 cm <sup>2</sup>	1x1x0.15 cm <sup>3</sup>	7, 18, 30 (mgAu/ gr tumor)	2.114, 3.811, 5.601	MCNP		
	4 MV	4x4 cm <sup>2</sup>	2.4x2.4x3.5 cm <sup>3</sup>		1.009, 1.019, 1.032	EGSnrc		
	4 MV FFF				1.019, 1.044, 1.074			
	6 MV				1.007, 1.015, 1.025			
	6 MV FFF				1.014, 1.032, 1.053			
S. H. Cho et. al. (2009)	Yb-169	0.01x0.01x1 cm <sup>3</sup> (at tumor center)	3x3x3 cm <sup>3</sup>	7, 18 (mgAu/ gr tumor)	<a href="#">appendix image 1</a>	MCNP/EGSnrc/NOREC		
	I-125							
	Pb-103							
	Ir-192							
	50 kVp							
B. L. Jones et. al. (2010)	Yb-169			7 (mgAu/ gr tumor)				
	I-125							
	Pb-103							
	Ir-192							
	50 kVp							
6 MV	4x4 cm <sup>2</sup>	2x2x3 cm <sup>3</sup>						
F V. d. Heuvel et. al. (2010)	0 – 200 kVp	phantom diameter	1 mm slab	0 - 10%	<a href="#">appendix image 2</a>	MCNP		



Author	energy & source	source information	target size	concentration of Au (mgAu/ gr tumor)	DER	MC codes
M. K. K. Leung et. al. (2010)	50 kVp	GNP diameter	2, 50, 100 nm GNP	-	<a href="#">appendix image 3</a>	GEANT4
	250 kVp			-		
	Co-60			-		
	6 MV	GNP diameter		-		
	150 kVp				-, 1.4, 2.2	
	6 MeV	electron beam			2.7, 2.9, 4.0	
E. Lechtman et. al. (2011)	300 kVp	GNP diameter	1.9, 5, 30, 100 nm GNP	single nanoparticle of 2, 50, 100 nm diameter		MCNP5 / PENELOPE
	6 MV	GNP diameter				
	395 keV	GNP diameter (Ir-192 HDR)				
	93 keV	GNP diameter (Yb-169 - HDR)				
	28 keV	GNP diameter (I-125)				
	21 keV	GNP diameter (Pb-103)				
R. I. Berbeco et. al. (2010)	6 MV	-	2x2x10 μm <sup>3</sup>	0 - 50 (GNP size =100 nm)		analytical calculation
S. J. McMahon et. al. (2011)	20-150 kVp	GNP diameter (x-ray spectra)	GNP size = 2 – 50 nm	-	<a href="#">appendix image 4</a>	GEANT4-DNA
	160 kVp	GNP diameter (x-ray tube)				
Stephen J. McMahon et. al. (2011)	6 MV	GNP diameter (full linac simulation)	GNP = 2 nm	-	<a href="#">appendix image 5</a>	GEANT4-DNA
	15 MV					
W.N. Rahman et al (2009)	80 kVp	x-ray	GNP = 1.9 nm	0.25, 0.5, 1 mM	4, 20, 24.6	-
	150 kVp				-, 1.4, 2.2	
	6 MeV	electron beam			2.7, 2.9, 4.0	

#### **I.4.F DER vs. RBE and SER**

As mentioned in the previous section there are several studies trying to calculate DER when GNP are present. The desired final outcome of radiation therapy is not to increase the dose in the area of interest but the tumor cell killing. As a result, the radiobiological question arising is if there is a relation between the cell Relative Equivalent Effectiveness (**RBE**) and DER. It is of great importance what the actual effect in cell killing is, when dose is enhanced at the vicinity of different cellular and sub cellular targets.

There are a few studies [87, 92-94, 98, 99] which tried to measure or calculate DE and enhancement of cell killing when GNP were present. Energy, beam quality, GNP size and cell types dependence where aspects of the problem which these studies tried to link with the initial question.

The first study was from D. M. Herold et al [87]. In this study, the authors used gold microspheres of 1.5 - 3  $\mu\text{m}$  size. The spheres were placed inside a flask (75  $\text{cm}^2$ ) among cells and they were irradiated using a 200 kVp x-ray beam. Three different cell types (CHO-K1, EMT-6, DU-145) where used, as well as three different concentrations of GNP microspheres 0, 0.5 and

1%. The cells after irradiation were counted in order to compute their survival fraction curves (LQ model). In the same study, a toxicity study of gold microspheres versus Bismuth powder was also conducted, and the authors concluded that Bismuth is too toxic to be used as a dose enhancer. Furthermore, they also irradiated the cells with a Cs-137 source (energy = 662 keV) in order to see if there are DE effects when higher energy is used. From this study  $\alpha$ ,  $\beta$ ,  $\alpha/\beta$  values were calculated for the three different cell lines, with and without the presence of the gold microspheres. The authors also calculated a Dose Modification Factor (DMF) which was the ratio of dose without gold over dose with gold for 1, 10 and 50% of the cell survival. According to this, DMF (10%) reached values of 1.38 – 1.54 depending on the cell type, with DMF values decreasing as the percentage cell survival was reduced. DER was higher for higher concentration of gold, with the measured values (chemical dosimeter method) being 1.16 (0.5% concentration) and 1.42 (1% concentration). For Cs-137 source no DE was measured even for the highest concentration, so authors concluded that they do not expect any benefits from MV beams.

Another study calculating RBE with and without the presence of NP was by Pignol et al [21]. In this study MC simulation techniques (MCNP-4C code) were used for calculating RBE of different NP types (Iodine concentration = 1.3mg/gr and Bromine with concentration=0.85mg/gr) for different beams and for L-132 cell types. Simulated beams were 6 MV, Co-60, Ir-192 brachytherapy and a Cs-137 beam. According to this study, RBE values varied from 1.01 (6 MV and Co-60) to 1.12 (Ir-192) for Iodine, while for Bromine were almost constant (~1.02 -1.03) for all beams.

Rahman et al [94] did not calculate RBE, but the measured DER (mentioned as dose enhancement factor DEF in their study) for BAEC cells, and for energies of 80, 150 kVp and 6 and 12 MeV, when a 1.9 nm GNP is used. They placed the NP inside a 75 cm<sup>2</sup> flask containing the cells and irradiated the flask for all the mentioned energies and for four different GNP concentrations (0.125, 0.25, 0.5, 1 mM). In this study, they gave a detailed description of the geometrical setup of the flask, as well as the cell irradiation and growing process and methodology of measurement. DEF was defined as the ratio of dose given to the control cell culture (without GNP) at 90% cell survival over the same dose when GNPs are present. DEF values varied from 1.4 (150 kVp – 0.5 mM) to 24.6 (80 kVp – 1 mM), as it was mentioned in a previous section of the current dissertation. Dose delivery uncertainty was 5% for x-rays and 2% for electrons while the total error was ~20% mainly due to viability assays.

S J Jain, et al [99] calculated the Sensitization Enhancement Ratio (SER), which is the ratio of the Mean Inactivation Dose (MID) without GNP over the MID with the presence of GNP (spheres 1.9 nm size) for three different cell lines (MDA-MB-231, DU-145 and L132) and for different irradiation conditions. The methodology of the cell irradiation and measurements was similar with the previous studies mentioned [94]. Cells were placed into plates and irradiated for



different beam energies. Before the irradiation, imaging of the cells took place, when GNPs were used, in order to observe the NP uptake by the cells. For that purpose cells were frozen and 60 – 70 nm slices were cut and observed under an electronic microscope.

Regarding the irradiation, cells were placed at 35 cm<sup>2</sup> dishes and exposed for 24 hours to 0.05% GNP by mass. After that dishes were irradiated with a dose from 0 to 6 Gy. Energies used were 160 kVp (x-ray tube), 6 and 15 MV linac as well as electron beams of 6 and 16 MeV. For photon beams irradiations SSD was set to 100cm, field size to 15x15 cm<sup>2</sup>, while the plates were placed at depth of 5 cm in solid water with 6 cm of backscatter solid water plates (Gandry was set to 180°). The survival cell curve was calculated and  $\alpha$ ,  $\beta$  and  $\alpha/\beta$  parameters were extracted with and without the presence of the GNP along with their experimental uncertainty, which was much lower when GNPs were present. Generally, uncertainty of the measured  $\alpha$ ,  $\beta$  values varied from ~5 to ~2200%, but for most cases it was between 10 - 25%. The calculated SER values varied from 0.92 – 1.41 depending on the cell type and the beam quality. Except from two cases (160 kVp, DU-145 cells and 6 MeV, L132 cells), all the values were higher than 1.04, with the highest (1.41) for 160 kVp beam. The comparison between different cell types showed that the highest values were calculated for MDA-MB-231 cells while the lowest for L132. At this point, it should be mentioned that the study gave the full list of SER per energy and beam only for MDA-MB-231 cells.

McMahon et al [92, 93] used  $\alpha$ ,  $\beta$  values from already published papers to simulate (GEANT4 code) SER and RBE for different energies (6 and 15 MV and kVp beams from 20 – 140 kVp) and for MDA-MB-231 cells. GNP size varied from 2 – 50 nm while the concentration of GNP used for the experiments was 500 µgr/ ml. These studies showed the relation between macroscopic and microscopic RBE for different GNP sizes and energies. Their result for the smallest GNP size (1.9 nm) and megavoltage energies showed that the maximum SER is 1.29 (6 MV). Regarding the RBE the values varied from 1.02-1.4 for kVp beams range Table 2 below summarizes all the mentioned studies of this section.

We conducted a custom literature search in order to collect measured or calculated  $\alpha$ ,  $\beta$  and  $\alpha/\beta$  ratios for different cell types and organs versus energy [103-113]. The goals was to link differences of SER and RBE values versus energy, and explain discrepancies between the calculated and simulated DERs and the measured RBE and SER of different cell lines. Energy ranges varied from low dose rate brachytherapy sources (I-125 and Pb-103) [104, 110, 112], high dose rate brachytherapy sources (Ir-192) [108], 250 kVp x-ray sources [103, 113], external MV beams [105 - 107, 109, 111, 112]. All these studies used different cell lines, organs and tissues both from humans and animals. All the data are presented in details in Table 3 while Figure 2 shows the  $\alpha/\beta$  ratio values for different energies. X axis shows the effective energy of each source in keV.

**Table 2:** Sum of the published SER, RBE,  $\alpha$ ,  $\beta$  after experiments or MC simulations with information regarding the energy and the size of the source, GNP concentration or GNP size.

Authors	Energy	NP size	NP concentration	Cell lines	$\alpha$ water (Gy <sup>-1</sup> )	$\beta$ water (Gy <sup>-1</sup> )	$\alpha$ GNP (Gy <sup>-1</sup> )	$\beta$ GNP (Gy <sup>-2</sup> )	DE quantity
W. N. Rahman et. al. (2009)	80 kVp	1.9nm	0.125/ 0.25/ 0.5/ 1 mM	BAEC	-	-	-	-	DEF= 4/20/ 24.6
	150 kVp				-	-	-	-	DEF= - / 1.4/ 2.2
	6 MeV				-	-	-	-	DEF= 2.7/ 2.9/ 4.0
	12 MeV				-	-	-	-	DEF= - / 3.7/ 4.1
D. M. Herold et. al (2000)	200 kVp	1.5-3 $\mu$ m	0, 0.5, 1 %	CHO-K1	0.233 (+/- 0.04)	0.0569 (+/- 0.006)	0.3046 (+/- 0.05)	0.111 (+/- 0.01)	DMF=1.36/1.38/1.38
				EMT-6	0.092 (+/- 0.056)	0.0251 (+/- 0.006)	0.1932 (+/- 0.03)	0.051 (+/- 0.005)	DMF=1.64/1.54/1.50
				DU-145	0.158 (+/- 0.017)	0.0426 (+/- 0.002)	0.2593 (+/- 0.08)	0.681 (+/- 0.012)	DMF=1.48/1.43/1.33
S Jain et. al. (2011)	160 kVp	1.9nm	0.05% by mass exposure for 24h	MDA-MB-231	0.019 (+/- 0.025)	0.052 (+/- 0.007)	0.091 (+/- 0.031)	0.093 (+/- 0.011)	SER=1.41
	6 MV				0.002 (+/- 0.022)	0.079 (+/- 0.007)	0.104 (+/- 0.04)	0.098 (+/- 0.011)	SER=1.29
	15 MV				0.083 (+/- 0.027)	0.059 (+/- 0.008)	0.061 (+/- 0.05)	0.121 (+/- 0.018)	SER=1.16
	6 MeV				0.05 (+/- 0.002)	0.055 (+/- 0.008)	-0.088 (+/- 0.034)	0.128 (+/- 0.013)	SER=1.04
	16 MeV				-0.038 (+/- 0.027)	0.079 (+/- 0.008)	0.18 (+/- 0.036)	0.015 (+/- 0.012)	SER=1.35
	160 kVp			DU-145	0.019 (+/- 0.025)	0.052 (+/- 0.007)	0.091 (+/- 0.031)	0.093 (+/- 0.011)	SER=0.92
	6 MV				0.002 (+/- 0.022)	0.079 (+/- 0.007)	0.104 (+/- 0.04)	0.098 (+/- 0.011)	SER=1.13
	15 MV				0.083 (+/- 0.027)	0.059 (+/- 0.008)	0.061 (+/- 0.05)	0.121 (+/- 0.018)	
	6 MeV				0.05 (+/- 0.002)	0.055 (+/- 0.008)	-0.088 (+/- 0.034)	0.128 (+/- 0.013)	SER=1.12
	16 MeV				-0.038 (+/- 0.027)	0.079 (+/- 0.008)	0.18 (+/- 0.036)	0.015 (+/- 0.012)	
	160 kVp			L132	0.019 (+/- 0.025)	0.052 (+/- 0.007)	0.091 (+/- 0.031)	0.093 (+/- 0.011)	SER=1.05
	6 MV				0.002 (+/- 0.022)	0.079 (+/- 0.007)	0.104 (+/- 0.04)	0.098 (+/- 0.011)	SER=1.08
	15 MV				0.083 (+/- 0.027)	0.059 (+/- 0.008)	0.061 (+/- 0.05)	0.121 (+/- 0.018)	
	6 MeV				0.05 (+/- 0.002)	0.055 (+/- 0.008)	-0.088 (+/- 0.034)	0.128 (+/- 0.013)	SER=0.97
	16 MeV				-0.038 (+/- 0.027)	0.079 (+/- 0.008)	0.18 (+/- 0.036)	0.015 (+/- 0.012)	
	16 MeV								
J. P. Pignol et. al. (2003)	6MV	-	I (1.3mg/gr) Br (0.85mg/gr)						RBE= 1.01 / 1.02
	Co-60	-	-						RBE= 1.01 / 1.02
	Cs-137	-	-						RBE= 1.02 / 1.02
	Ir-192	-	-						RBE= 1.12 / 1.03
S J. McMahon et. al. (2011)	6 MV	2	-	MDA-MB-231	0.002 (+/- 0.02)	0.079 (+/- 0.007)	0.11 (+/- 0.03)	0.08 (+/- 0.01)	SER=1.29
	15 MV	2	-		0.077 (+/- 0.05)	0.071 (+/- 0.014)	0.17 (+/- 0.03)	0.072 (+/- 0.015)	SER=1.16
S J. McMahon et. al. (2011)	20 – 140 kVp	2-50nm	500 $\mu$ gr/ml	MDA-MB-231	0.019 (+/- 0.025)	0.052 (+/- 0.007)	0.091 (+/- 0.031)	0.093 (+/- 0.011)	RBE= $\sim$ 1.4 - 1.02 (GNP size 20nm)

Table 3: Sum of the published, $\alpha$ , $\beta$ and $\alpha/\beta$ parameters for different cell lines, tissues and organs.					
Authors	Energy	Cell lines	$\alpha$ water (Gy <sup>-1</sup> )	$\beta$ water (Gy <sup>-1</sup> )	$\alpha/\beta$ (Gy)
L M. GARCIA et. al. (2007)	250 kVp	CHO AA8	0.167 (+/- 0.015)	0.0205 (+/- 0.0015)	-
J Z Wang et. al. (2007)	I-125	prostate	0.15		3.1
	Pb-103				3.1
M I Koukourakis and I Abatzoglou et. al. (2007)	External MV beam		bladder		
		rectum			4
					4
J L Dumas et al (2007)	External MV beam	Esophagus tumour			10
		lung			3.5
		spinal cord			2
		heart			2.5
D J Brenner et. al. (1999)	External MV beam	prostate	0.036	0.024	1.5
D J Brenner et. al. (2002)	HDR (Ir-192)		0.026		1.2
H. D. Thames et. al. (1989)	External MV beam	vocal cord	-	-	9.9
		oral cavity/ oropharynx	-	-	6.5 - 10.3
		lung	-	-	50 -90
		cervix	-	-	13.9
		skin	-	-	8.5 (4.5 - 11.3)
		melanoma	-	-	0.6 (-1.1 - 2.5)
		liposarcoma	-	-	0.4 (-1.4 - 5.4)
HENK B. KAL et. al. (2003)	Pb-103/I-125	prostate	0.1	0.026	3.90
JIAN Z. WANG et. al. (2003)	External MV beam		0.15 (+/- 0.04)	-	3.1 +/- 0.5
A. Dasu (2007)	External MV beam/ I-125		-	-	1.5
	Pb-103/ I-125		-	-	1.49
	External MV/ brachy- beam		-	-	1.2
	Pb-103/ I-125		-	-	3.1
			-	-	3.1-3.9
	External MV beam		-	-	8.4
			-	-	1.33
			-	-	1.12
			-	-	8.3
			-	-	2.38
			-	-	2.2
J. Van Dyk, K. Mah and T.J. Keane (1989)	-	lung (pig)	-	-	3.84 (+/- 0.39)
	x-ray beam 250 kVp	mouse	-	-	3.68 (+/- 0.16)
			-	-	4.25 (+/- 0.58)
			-	-	5.11 (+/- 0.24)
			-	-	4.59 (+/- 1.83)
			-	-	6.00 (+/- 5.27)
	-		-	5.83 (+/- 0.6)	
	-		-	5.58 +/- 1.87	

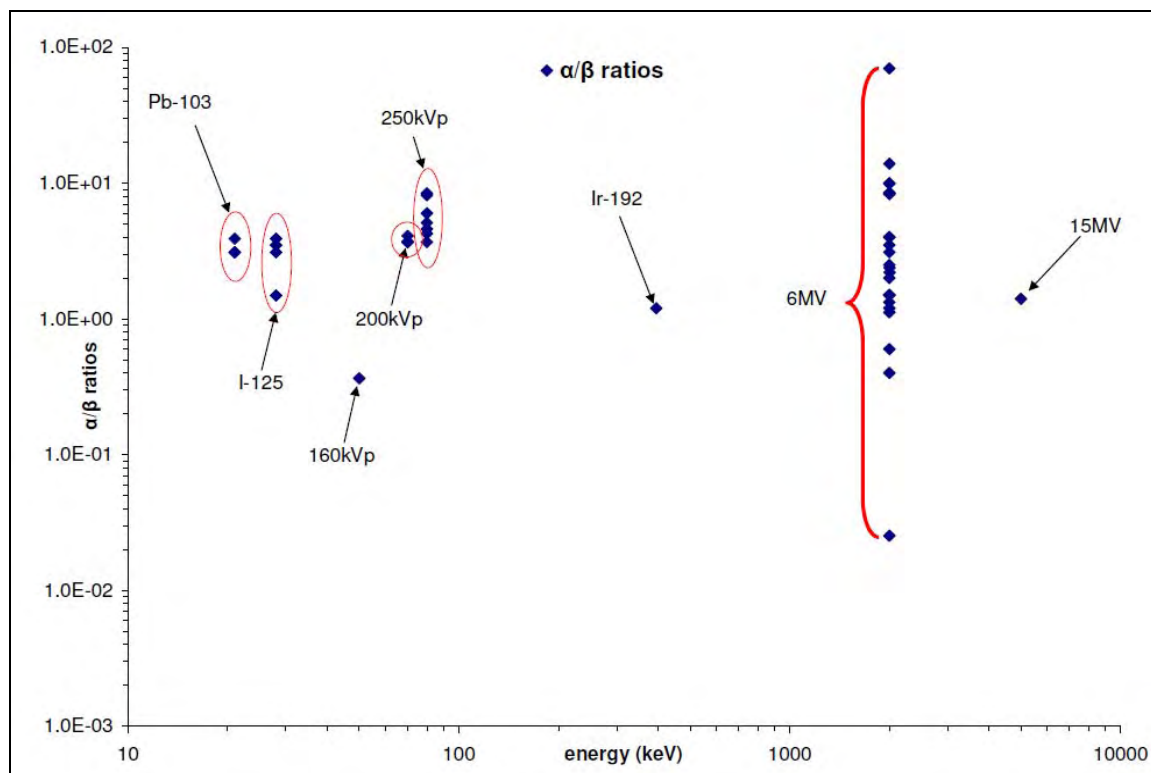


**Figure 2:**  $\alpha/\beta$  ratio data for different cell lines, tissues and organs versus energy (keV).

#### **I.4.G Imaging for tracking and localizing NP**

One of the main questions to be answered regarding NP is where they travel when they are injected into the patient's blood stream or mixed with cells in vitro experiments. Depending on the scale, the questions to be answered can be separated in macroscopic imaging of the biodistribution among tissues and in nanoscopic imaging of clusters of GNPs in single or cluster cells. This question is of great importance as the magnitude of DE might cause different outcome depending on NP position in cellular and sub-cellular space. Unezaki et al [114] showed that the cell pores do not permit the entrance of NP larger than 400 nm, while for sub-cellular targets, such as the DNA helix which has a size of  $\sim 1\text{-}2$  nm, the NP size should probably not be larger than a few nm. Moreover, it is important to know if and how NP are clustering as well as for how long NP stay in the area of interest. Clustering of GNP has been previously reported [93], but up until now there has been no extensive study shedding more light at this aspect of the problem. Knowing an effect like this, can be used to target more efficient areas of the cellular or sub-cellular space, which is of greater importance than others or more sensitive to radiation damages (e.g. DNA). Furthermore, there are some more equally fundamental questions such as the accurate targeting of the NP. This question is beyond the interest of the current review of the literature, so information about this subject will not be provided.

In order to give an answer to all of these questions, new techniques should be developed which will help imaging and tracking of NP when these are used for DE radiation therapy or imaging. Sub-cellular imaging for NP is still under development, and there are not so many publications studying the possible effects and problems of this challenging field.

Lasne et al at 2006 [115] published a paper regarding an experimental technique, based on photo thermal imaging with high intensity laser beams, in order to track GNP of 5 nm size placed in live cells. This method was basically tracking 2D trajectories of the GNP for time period of a few minutes. S.K. Cheong et al [116] used quasi-monochromatic cone /fan x-ray beam at a x-ray fluorescence CT (XFCT) of 110 kVp of focal spot size of 100  $\mu\text{m}$ . This beam was used for the irradiation of solutions containing AuNPs at 1 and 2% by weight with 1.9 nm diameter. Solutions were placed inside a small animal phantom and irradiated from different angles. All the rotational and translational stages were motorized with a minimum incremental motion of 2.19 arcsec and a resolution of  $\sim 100$  nm respectively. A macroscopic 3D reconstruction was done to image the solutions containing the GNPs. Resolution of the reconstructed image was of the order of 1 mm. J Li et. al. [117] used AuNP as an agent of functional micro CT. In the same study the authors showed images of 4 nm GNPs and their uptake in different cellular areas.

#### **I.4.H Nanodosimetry with Monte Carlo techniques**

Studies for the DE effects were increased significantly the past few years. The different therapeutic and imaging capabilities of these effects are opening a whole new area in the field of radiation therapy and imaging. The studied physical scale of these effects along with our inability to find an accurate method of measuring them is a big challenge. This challenge is even greater when methods with their own limitations, such MC techniques are being used.

MC methods are a great tool for studying the physical process of a certain system, but it must be used with caution. Model, cross sectional and physics limitations should be taken into account and always should be evaluated against independent experimental or simulated data during the benchmarking process. Cross sectional uncertainties are the most important ones as cross section data below 1 keV, for most of the codes, are only valid for water. Because of this fact, the calculation of DE should be treated with caution. Combination different codes, (e.g. CHM and track structure codes) should be handled in a similar way. Different statistical and physical parameters should be tuned, in order to have reliable results. This is not a trivial task and a lot of trial and error testing is required. On top of that, the long simulation time and the large uncertainty errors are not negligible.

Another point that should be brought to light are geometrical set up differences of the MC experiments up until now. Detailed information of the source type and distance from the target

are essential. For example, using a phase space versus using a spectrum will produce different results as the spectrum does not contain the angle distribution information of the particles. On the other hand spectrum is less noisy than a phase space and more straightforward to use, as rescaling a phase space from cm – mm scale to  $\mu\text{m}$  – nm scale might lead to errors.

A second type of studies, regarding DE, was experiments which measured directly or indirectly the enhancement effects when NP was present. A closer look reveals several difficulties and challenges. The geometrical setup and the details about irradiation techniques are the first points that should be considered. The DE effects have a range of a few  $\mu\text{m}$ , so knowledge of the exact position of the NP is essential to estimate if the measured effect can be neglected or not. Cell types are also a very important aspect of these studies. Different cell types have different dose response. Furthermore, energy is another important component that creates large variation for different results, as demonstrated in [Figure 2](#). In order to overcome all these differences, more details of the experimental set up and procedure should be mentioned using diagrams of the experimental set up.

In conclusion, it should be mentioned that many of the published studies constitute proof of principle studies, and their purpose is not to characterize basic properties in a comprehensive fashion. This is where the current work fills this gap, by being systematic and comprehensive. The DE effects and the radiobiological measured effects on tissues and cells need to be studied and reported with more details. DE effects can reach up to three orders of magnitude when MC techniques are used but the measured DE has a maximum value of  $\sim 20$  for the most extreme cases, with average values being  $\sim 1.5 - 3$  for most of the cases. Cell survival results are even more modest compared with the DE results. Cell survival curves show a benefit of a factor 5 - 30 %. These numbers reveal the need for accurate experiments with knowledge of the details of the setup and its components. Combination of the above with MC codes can be performed as long as the user retaliates the limitations and the possible problems that could arise from factors such as cross section, geometry, source type, scoring area (cube vs concentric circles), units (e.g. number of Au atoms/mgr or ionization/Gr etc). Additional challenges are the normalizations used in MC, adequate assumptions about the angular or energy distribution of electron/photons at the level of GNP, large noise, lack of experimental data for benchmarking, insufficient understanding of the relation between the track codes and the dose codes (energy scoring using some version of slowing down approximation).

## II. METHODS AND MATERIALS

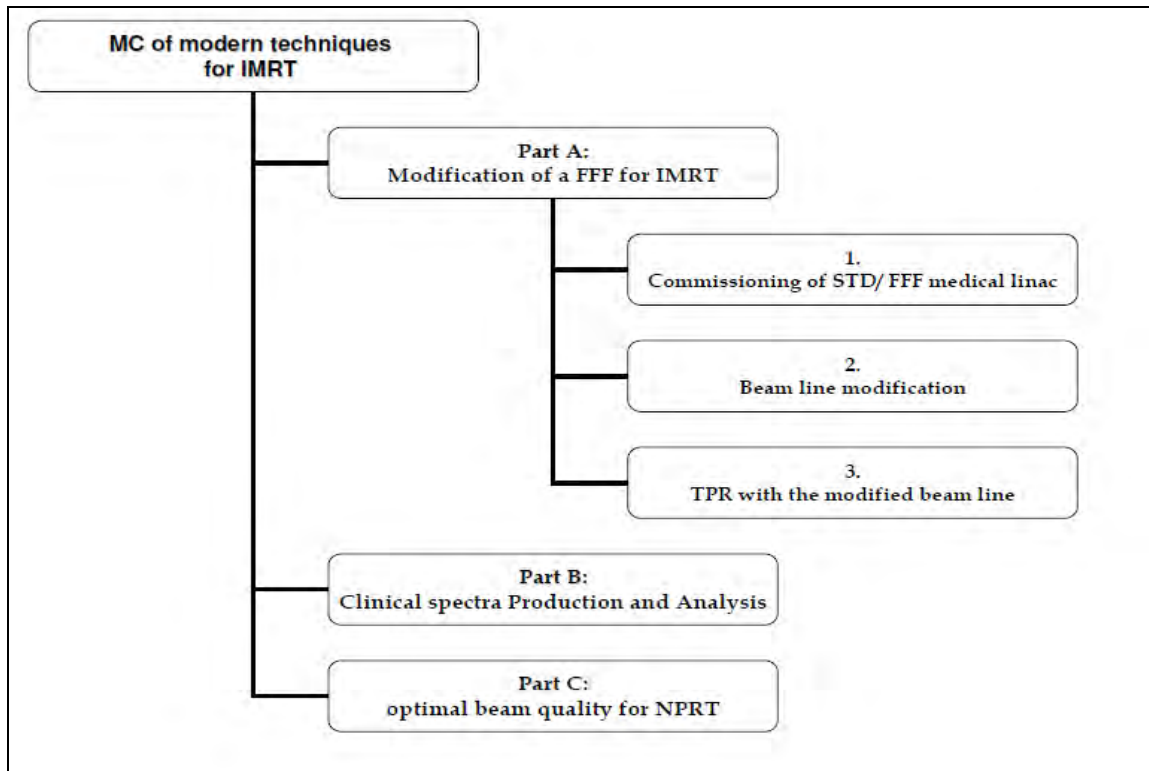


**Figure 3:** Dissertation flowchart.

### Part A: Modification of a FFF for IMRT

#### II.1. Monte Carlo simulation of the medical linac

##### II.1.A Verification of the linac model in general

A verification method for a linac is well described in the literature [118 - 154]. The extensive literature on this subject is related mainly with the many aspects and cases included in this process. Different linac types (electron, photon etc), different components of the head assembly (stereotactic cones, flattening filters, MLC etc), different techniques (VMAT, IMRT, CRT etc), different studied areas (in-field, out-of-field etc), new simulated techniques (e.g. Directional Bremsstrahlung splitting - DBS) or component modules used (e.g. DYNVMLC module for the dynamic mode delivery of Varian linacs), inaccuracies in the blue print data provided by the different manufactures etc.

If we have to define a general methodology that could be a synopsis, the following steps, at least for the case of the photon beams, are to be taken:

1] Definition of the energy and the FWHM of the e- beam hitting the Bremsstrahlung target. This is being done through matching PDD curves of MC model and measurements for a medium (e.g. 10x10 cm<sup>2</sup>) and large field size (40x40 cm<sup>2</sup>). For this step the most important information of the beam assembly are the material and thickness of the target (along with the cooling material



beneath him if exists) and the flattening filter. Another very important component for accurately simulating the current process is the opening of the primary collimator which is quite common for most of the manufacturers.

2] When the above information is matched then the changes of the “Gaussian” like shape of the flattening filter for the largest possible field size (40x40 cm<sup>2</sup>) follows for matching the field oars for different depths. Shape of the flattening filter is of great importance for an accurate simulation of the head assembly but the uniqueness of each filter even for the same linac model makes its modeling very challenging.

Besides the two mentioned steps above different steps are followed if the model is going to be used for out-of-field studies and IMRT studies, the last of which includes accurately modeling of the MLC's.

## **II.1.B MC Model verification for FFF and STD linac**

### **II.1.B.i. Commissioning flowchart**

Before giving a detailed description of the methods we provide a general overlook of this study [figure 4]. Properties of unaltered (FFF) and a modified mFFF vs. STD linac are determined in a series of MC simulations. Firstly, verification of STD linac model was done by using complete measured beam data (open and IMRT beams) of STD linac. Next, selected beam properties of the FFF linac were validated through comparison with measurements taken at the linac after removing the flattening filter. Finally, a modified mFFF linac with adjusted electron beam properties was simulated.

Specifically, as a starting point for consideration, it is being proposed an approach in which FFF linac energy is adjusted in such a way that beam penetration area on the central axis of FFF is approximately equal to those of STD linac. After matching beam penetration we calibrate FFF linac in such a way that dose output (linac calibration dose in the reference conditions per MU) is approximately equal to that of a STD linac. Calibration was done by calculating the dose ratio of FFF vs STD linac for a certain field, depth and for the same initial histories. Simultaneously, dose rate (dose per time) of FFF linac is maximized compared to STD linac as we deliver the same dose in a shorter time. That enables a more fair comparison of other beam properties, which depend on off-axis distance and play a role in IMRT optimization. We study these properties in beams modulated by dynamically moving MLC, utilizing closed MLC and sweeping gap patterns of various gap sizes. Next, we determine basic beam properties of the energy-modified FFF linac, for open and dynamically modulated beams. After that we focus on open FFF beam flatness in regards to IMRT applications. Since, flattening of photon beam profile is expected to somewhat compromise dose rate and scatter benefit of thus modified FFF (mFFF) linac we characterize them accordingly.



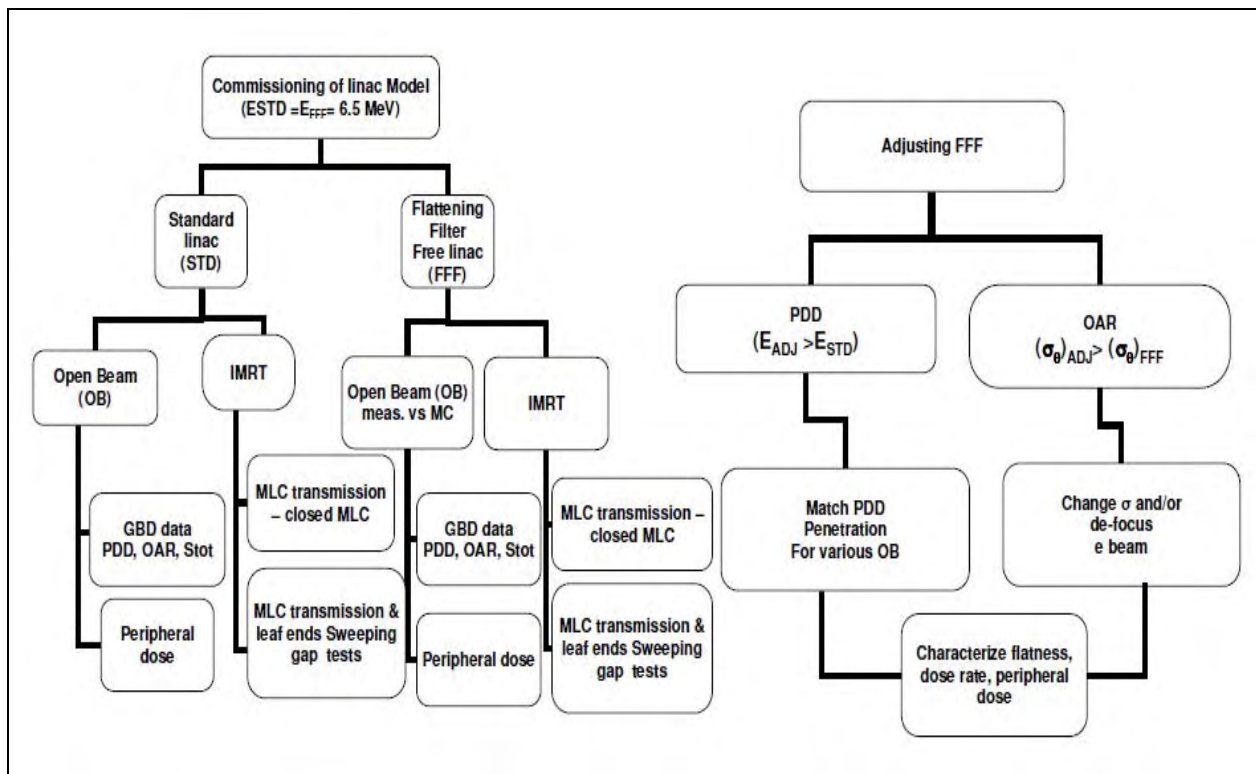


**Figure 4:** General flowchart of the commissioning tests for the verification of the STD and FFF linac for, in and out-field area and for IMRT delivery (left chart) and for the modifying FFF linac (right chart).

### II.1.B.ii. EGSnrc code simulation parameters

For this study, MC EGSnrc with BEAMnrc and DOSXYZnrc codes were used [152-154]. Simulations were performed for Varian 21EX (6 MV). The geometry and materials of the head were based on a blueprint from Varian with certain necessary modifications. Head structures included in the simulation were: target, primary collimator, Beryllium window, flattening filter, ionization chamber, secondary collimator, jaws and MLC. Cut-off energy for electrons (ECUT) and photons (PCUT) was set to 0.7 MeV and 0.01 MeV respectively and global electron cut-off (ESAVE) was set to 2 MeV. Directional Bremsstrahlung Splitting (DBS) was selected for Bremsstrahlung photons with splitting and field radius set at 40 cm, in order to cover a large area in and out of field. All EGSnrc default parameters and options were used, except for options “Bound Compton scattering”, “Photoelectron angular sampling” and “Atomic relaxations” which were set on. For “Brems angular sampling” and “Pair angular sampling” options Koch-Motz (KM) distribution was chosen.

As it is shown in previous publications [134, 147, 149] the best description of linac data can be obtained with electron beam hitting the target vertically and having a Gaussian elliptical spatial extension. According to the above standard deviation ( $\sigma_x$ ,  $\sigma_y$ ) values of the beam was set to 0.08 cm (X direction) and 0.16 cm (Y direction). Mean angular spread of beam  $\sigma_\theta$  was set to  $0^\circ$  while electron beam energy was set to 6.5 MeV.

The phantom was made of water and had size of 71x71x30 cm<sup>3</sup>. The number of histories used was set for every field size separately. Simulation goal was to keep standard deviation for the in-field area less than 1%. For the out-of-field area the calculated standard deviation was different for each field and it will be mentioned separately for each studied case. Phantom for STD linac had voxel size for X and Y axes of 0.5 cm at the flatness area, 1 cm out of field and 0.2 cm at the edges of the field. Z axis voxel size was set to 0.2 cm until depth of 3 cm and 1 cm for the rest of the phantom. FFF linac selected voxel size was 0.5 cm for X and Y axis while for Z axis was the same as for STD linac.

### **II.1.B.iii. Commissioning of STD linac**

We verified MC dose calculation for Varian 21EX (6 MV) standard machine. Verification included matching calculated data to measured beam data set provided by Varian named as “Golden Beam Data” (GBD) using the Wellhofer water tank (7020WDA). Verification data includes Percentage Depth Dose (PDD), off-axis ratio (OAR) and total scatter factor  $S_{tot}$  for different open beam (OB) field sizes (4x4, 6x6, 10x10, 15x15, 20x20, 30x30 and 40x40 cm<sup>2</sup>) and different depths ( $d_{max}$  =1.5 cm, 5 cm, 10 cm, 20 cm) and for SSD = 100cm [125]. Verification process had two steps. At first, energy of electron beam was adjusted in such a way that matches GBD for all field sizes. Secondly, we matched OAR profiles by changing spatial extensions ( $\sigma_x$ ,  $\sigma_y$ ) of the electron beam.

### **II.1.B.iv. Commissioning of model for IMRT**

For MLC modeling DYNVMLC module was used as it allows simulation of dynamic field sizes [118]. In order to verify that MLC modeled accurately the following simulations were conducted. The goal of these simulations was to match MLC transmission ( $T_{MLC}$ ) through the leaves and accurate model rounded leaf-ends. Closed MLC and sweeping gap tests (SG) were used for various gap sizes and for different fields. The set up was for SSD= 95 cm at depth of 5 cm. All measurements were done on central axis point. The selected field size for matching transmission was 12x28 cm<sup>2</sup> and for sweeping gap tests (SG) was 10x10, 12x28 and 14x28 cm<sup>2</sup> for gap sizes  $G = 1, 5, 10$  and 20 mm. Two different MLC moving test patterns were simulated. First pattern had starting and ending point of gap centers at the edges of the field (leaves half-inside-half-outside of the field). For the second pattern gap centers started outside the field and ended outside. A graphical representation of the two patterns is presented in figure 5 below.

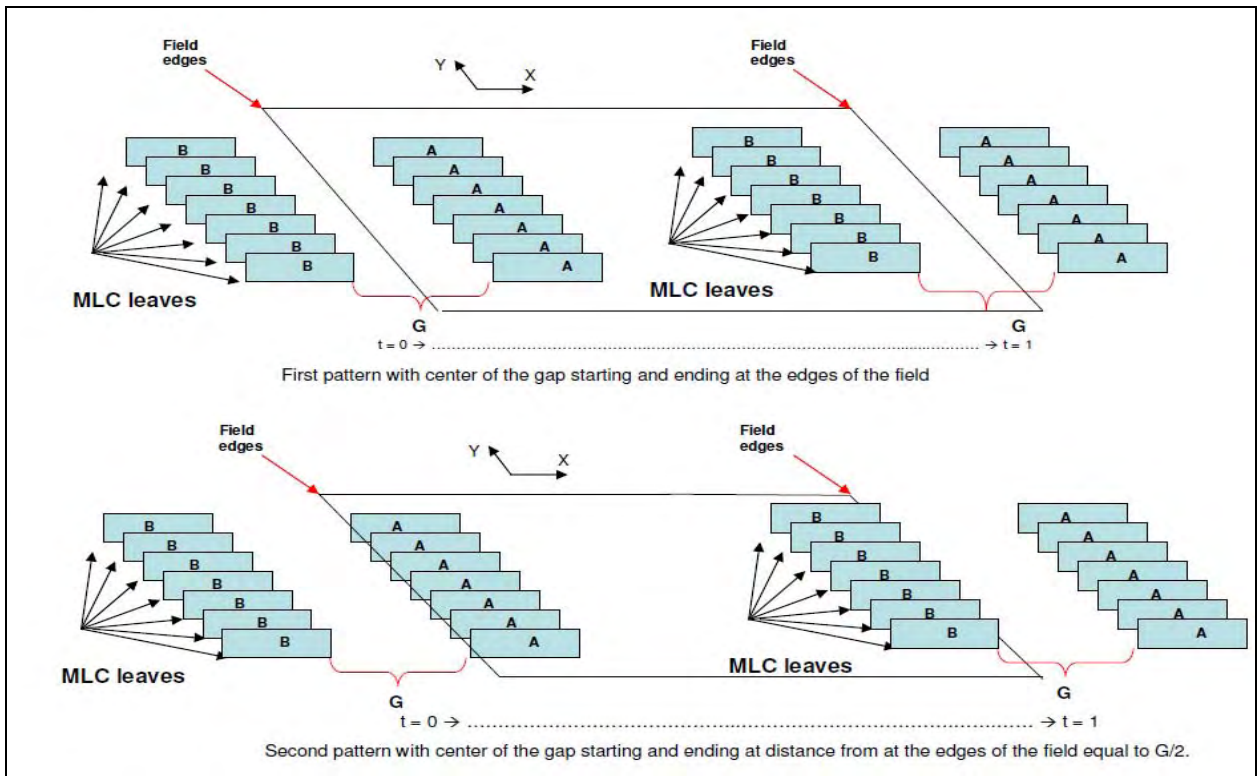


**Figure 5:** Pattern with center of the gap starting and ending at the edges of the field (upper image). Pattern showing the center of the gap starting and ending at distance from at the edges of the field ( $= G/2$ ) (lower figure).

Quantification of MLC transmission, for the above ML patterns, was made by calculating dose ratios for closed MLC  $R_{cMLC}$  and for SG tests  $R_{SG}$ , which were given by the equation below [159], while the whole model was based to previous published methodology [158-161]:

$$R_{MLCtest} = \frac{D_{MLCtest}(x=0, y=0, c_x, c_y, d)}{D_{OB}(x=0, y=0, c_x, c_y, d)} \quad (6)$$

where  $(c_x, c_y)$  are the field size dimensions,  $d$  is the depth and  $MLC_{test}$  signifies either closed MLC (cMLC) or sweeping gap (SG) tests and OB is open beam. These ratios are expressing dose between close MLC and moving MLC, in dynamic mode, with dose for OB and they have field size and depth dependence. In order to match transmission through the leaves several simulations were conducted using different leaves densities and interleaf air gaps. Simulation showed that MLC density of  $17.5 \text{ gr/cm}^3$  and interleaf air gap of  $0.0065 \text{ cm}$  matched transmission between MC and experimental data.

#### II.1.B.v. Commissioning of model for out-of-field area

In order to match peripheral dose (PD) and jaw, transmission for STD linac measurement were taken. These measurements were compared with MC simulations. Experimental measurements were made for field sizes  $1 \times 1 \text{ cm}^2$ , with MLC parked and MLC forming a field of  $1.2 \times 1.2 \text{ cm}^2$ . For

larger fields (6x6, 10x10, 15x15 and 30x30 cm<sup>2</sup>) measurements were made with MLC parked. For these measurements a solid water phantom of 30x60x15 cm<sup>3</sup> with measurement points at depth of 5cm and for SSD 95 cm was chosen. Measurements were made with ionization chamber (Exradin Model A12) for five out-of-field points (selected according to the field size). Dose to each point was normalized to the central dose for 30x30 cm<sup>2</sup> field (for field sizes 6x6 – 30x30 cm<sup>2</sup>) and 10x10cm<sup>2</sup> field (for 1x1 cm<sup>2</sup>) both irradiated by STD linac.

#### **II.1.B.vi. Monte Carlo model verification of FFF linac**

After verifying STD linac, flattening filter was removed from the simulation in order to simulate FFF linac. Data for FFF linac, including PDD, OAR and  $S_{\text{tot}}$  for all field sizes and depths, were simulated with the same set up (SSD=100 cm) used for STD linac.

Measurements for different field sizes (4x4, 6x6, 10x10, 15x15, 20x20, 25x25 and 30x30 cm<sup>2</sup>) were made for FFF and STD with the use of ionization chamber and MatriXX (IBA Dosimetry GmbH, Schwarzenbruck, Germany). For these measurements carousel holding the flattening filter had to be rotated and positioned in such a way that we would had an empty slot in the path of the beam. Inside that empty slot, as it was noticed and suggested [44], there is a 2 mm Cu plate covering the hole of the slot. The purpose of that Cu plate is to protect the ionization chamber, which is below the flattening filter, and reduce surface dose [44]. Experimental measurements were made for SSD=95 cm, for depth of 5 cm and for Y axis. For all the measurements a solid water phantom was used with dimensions of 30x60x15 cm<sup>3</sup>. The raw data measured by MatriXX detector was corrected using an accurate correction scheme presented in the literature [74].

In order to verify in-field measurements, for FFF beam, field sizes 4x4, 10x10, 15x15, 20x20 and 25x25 cm<sup>2</sup> were measured with MatriXX and compared with MC simulation results. Measurement setups were similar with the one described in the above section regarding PD dose measurements with ionization chamber.

For out-of-field regions two set of measurements took place. The first set was for fields 6x6, 10x10 and 15x15 cm<sup>2</sup> for both flattened and unflattened modes. Six points of measurements were chosen for each field size and linac. The first point was on the central axis and the last was almost 10cm away from the edges of the field. All points were normalized in such a way that 100% of the dose is delivered at the center of each field. From those measurements dose ratios FFF/STD were calculated for MC and measurements (ionization chamber and MatriXX). Also, dose ratios STD/FFF were calculated for the measurements vs MC as an extra method, which validated the accuracy of the MC model.

The second set of measurements was only for STD linac and only ionization chamber was used. Measured field sizes for this set up were 1x1, 6x6, 10x10, 15x15 and 30x30 cm<sup>2</sup>. Five points of measurement were chosen starting a few cm from the edges of the field (dependent on the filed

size) and ending at about 20 to 30 cm depending on the field size. Dose of each point was divided with a central STD linac dose measurement of a 30x30 cm<sup>2</sup> field (for field 6x6 – 30x30 cm<sup>2</sup>) and 10x10 cm<sup>2</sup> field (for 1x1 cm<sup>2</sup>) in order to have a common normalization between all points and fields. For field 1x1 cm<sup>2</sup> 50x10<sup>6</sup> initial histories were used with 10x10<sup>9</sup> histories in DOSXYZnrc. For the rest of the fields 2.5x10<sup>6</sup> initial histories were used with 2x10<sup>9</sup> histories in DOSXYZnrc. For the larger fields statistical uncertainty was below 2% until 30cm from the central axis. For small fields statistical uncertainty was smaller than 15% for all fields even until 25 cm distances from the center of the field.

## **II.2. Beam line modification**

### **II.2.A Modifying the energy of a FFF linac**

Simulations were made in order to find a higher energy (adjusted  $E_{ADJ}$ ) for FFF linac which matches PDDs of STD and FFF linac for different field sizes (6x6, 10x10, 15x15 and 20x20 cm<sup>2</sup>). All simulations were made for SSD of 100cm. In order to study how FFF linac dose rate will change the new energy dose ratio of FFF and mFFF linac versus STD linac was calculated at the center of the field (depth  $d=5$  cm and SSD=95 cm). For all the above results same initial histories were used (5x10<sup>6</sup>).

### **II.2.B Flattening of FFF beam by de-focusing the electron beam**

After adjusting the energy of the electron beam, electron beam properties were altered in order to improve flatness of FFF linac. Two different types of electron beam modifications were performed. Firstly, electron beam spatial dimensions were increased ( $(\sigma_x, \sigma_y)$  values). Sigma values of  $2x(\sigma_x, \sigma_y)$  and  $4x(\sigma_x, \sigma_y)$  of the initial value were tested. Following, mean angular spread of the electron beam was increased ( $(\sigma_{\theta x}, \sigma_{\theta y})$ ) and tested using all the combinations of the above different spatial spread. Mean angular spreads of  $\sigma_{\theta x} = \sigma_{\theta y} = 0^\circ, 5^\circ, 10^\circ$  and  $14^\circ$  were used. For values over  $14^\circ$  seems to be a conflict with conical opening of the primary collimator leading to suboptimal dose at the edges of the field.

In order to quantify possible loss of dose rate (so decrease in treatment time) for different angular spread values ( $0^\circ, 5^\circ, 10^\circ$  and  $14^\circ$ ), field sizes  $c$  (6x6, 10x10, 15x15, 20x20, 30x30 and 40x40 cm<sup>2</sup>) and depths  $d$  ( $d = 1.5, 5, 10, 20$  cm) a dose rate ratio  $R_{dose\ rate}$  was calculated.  $R_{dose\ rate}$  is the ratio of open beam doses of mFFF linac (with adjusted energy and with de-focused electron beam) to dose of STD linac for the same irradiation conditions. Ratio value referred to a certain field size and depth, and it is defined at the central axis ( $x=y=0$ ) as:

$$R_{dose\ rate} = \frac{D_{mFFF}(x=0, y=0, c, d)}{D_{STD}(x=0, y=0, c, d)} \quad (7)$$

Definition (7) was modified in order to characterize peripheral dose differences between STD linac and mFFF linac. Peripheral dose characterization has to be defined for off-axis points (x,y). In those cases, we defined a peripheral dose ratio  $R_{PD}$ , which quantified the dose of FFF linac for certain depth and field size, vs. dose for STD linac for the same irradiation conditions:

$$R_{PD} = \frac{\langle D_{mFFF}(x, y, c, d) / R_{dose\ rate} \rangle_{PD}}{\langle D_{STD}(x, y, c, d) \rangle_{PD}} \quad (8)$$

In equation (8) an effective (e.g. average) value of PD doses for mFFF and STD linac were used in order to characterize both linacs with only one parameter. In definition (8) dose  $D_{mFFF}$  of  $R_{PD}$  ratio is divided by  $R_{dose\ rate}$  to re-normalize it to the central axis dose. For the current study average PD is calculated for each field starting a few cm out of the treatment field. The starting point depends on the treatment field (e.g. 5 cm from the center for a 6x6 cm<sup>2</sup> field) and for fields  $\leq 10 \times 10$  cm<sup>2</sup> expands until 25 cm distance from the center, while for larger fields goes until 35 cm from the center.

### **II.2.C Unflatness of FFF linac**

In order to characterize the lack of flatness of FFF linac, for various depths (d) and field sizes (c) and for in-field areas, we define a convenient off-axis dose ratio  $R_{unif}$  of STD dose to FFF dose for the same (d,c) values. In addition, we model this ratio for the in-field area by using the formula:

$$R_{unif} = \frac{\frac{D_{STD}(x, y, d, c)}{D_{STD}(0, 0, d, c)}}{\frac{D_{mFFF}(x, y, d, c)}{D_{mFFF}(0, 0, d, c)}} = 1 + b |r|^n \quad (9)$$

Parameters (b,n) slightly depending on the field size and depth:  $(b = \beta(1 + \beta_0 c + \beta_1 d), n = \gamma(1 + \gamma_0 c + \gamma_1 d))$ ; r is the radius ( $\sqrt{x^2 + y^2} = r$ ). Fitting of this model function to data was performed in Mathematica (version 7.0).

Evaluation of the above formula and its parameters was performed by comparing open beam and sweeping gap profiles of FFF and STD linac with the ones produced by the formula. Sweeping gap tests measured for field sizes 10x10 and 14x28 cm<sup>2</sup> and gap sizes of G=10, 20 mm.



## II.3. Treatment planning study with the mFFF linac

### II.3.A General Concept

In IMRT the photon flux above the MLC does not need to be flat - since IMRT is capable of adjusting beamlet weights of beam of arbitrary flatness using inverse planning optimization. The question is if for FFF linacs that possess extreme non-uniformity across the beam IMRT can efficiently compensate for the flux differences. In section I.3.C i the published literature regarding FFF linac and IMRT studies were discussed. As it was mentioned planning IMRT studies involving STD and FFF comparison have been reported for different sites with others being in progress know that new beam lines (e.g. TrueBeam from Varian) are out in the market. Noteworthy, published literature, until recently, has not addressed the problem of IMRT for off-axis targets or for large targets, or targets further away from the isocenter. Recently, this problem was recognized in a treatment planning optimization paper [62] where new optimization algorithms had to develop in order to be more compatible with the Gaussian shape of the FFF dose profile.

However, based on the planning studies reported in References 54, 63 and 64, which show just a few examples for limited type of targets and plans, a claim can be made that these examples are by no means exhaustive, and they miss an important class of IMRT plans, which may not be deliverable on FFF. Therefore, it is not possible to answer all questions one may have under a closer look at the problem based on the published literature without additional work. Some of these questions relate to the effective dose rate benefit of FFF and to the effective peripheral dose benefit, the latter not being studied in the planning studies [54, 62-66].

Furthermore, it needs to be observed that for larger targets, which tend to be more complex, the effective MLC gaps of IMRT fields can be very small, the MU's are large and doses from MLC transmission and MLC scatter are large. Dose from MLC scatter contributes not only inside the field but also to the areas outside of the field. At the present time, the beam properties of IMRT plans on FFF linacs are not completely known. Considerable decrease of OB dose, for off-axis points for such cases, may be more difficult to be adjusted in IMRT optimization for FFF linacs (because the inverse planning is already difficult for the standard linac). One study [62] shows that inverse planning optimization produces very inefficient (large MU) plans for more complex sites such as H&N. The reasons of this might be due to the optimization algorithm or other limiting factors related to basic beam properties, which we attempt to characterize from that perspective.

Thus, unfortunately, the information reported in the treatment planning papers is not sufficient to reach a final conclusion about FFF- beam properties in IMRT (nor VMAT, which was not even attempted). Open beam properties of FFF were thoroughly studied by MD Anderson group, but

applications to IMRT to a lesser degree – for instance, one case of prostate plan was reported without sufficiently detailed information on the target (e.g. prostate only or prostate plus nodal extensions, which lead to much larger treatment volume, and make optimization much more difficult).

To support the above observation the following study was made by us. An explicit formula was created takes IMRT maps optimized for the standard linac and converts them to MLC motion patterns deliverable on FFF linac without re-optimization. Next, to determine the resulting properties of MLC motion, dose rate and dose distribution for both linacs. For that reason EGSnrc model for STD, FFF and mFFF was used to study dosimetric properties of 3 IMRT plans for various treatment sites (2 pelvises/ 1 prostate + LN). STD and FFF linacs were commissioned in Eclipse planning system after matching PDD and MLC properties of the two linacs by increasing the energy of the FFF linac by 2 - 2.5 MeV. Clinical IMRT plans for STD were converted to plans deliverable on FFF without re-optimization using a straightforward formula derived for the purpose of this study. STD and FFF IMRT plans had clinically equivalent DVH properties for target and somewhat similar though different DVH's for normal organs and remaining body (due to different STD/FFF beam properties). Comparative analysis of MLC leaf speeds, effective dose rates and scatter properties within normal organs and body was performed for STD/FFF.

STD-IMRT field maps were converted to FFF maps using a field-dependent correction function  $F(x, y | x_1, x_2, y_1, y_2, d)$ , thanks to which FFF-MLC leaf positions were calculated in a deterministic fashion without re-optimization. FFF-IMRT was compared to STD-IMRT plans by evaluation of MLC leaf speeds, effective dose rates and patient scatter.

### **II.3.B Treatment planning commissioning for FFF/ mFFF linac**

Commissioning of the Eclipse treatment planning had to be done for using the treatment planning for the above study. Data from the modified linac were imported in the TPR while the mFFF linac was calibrated to deliver the same dose at references conditions (10x10 cm<sup>2</sup> field size, depth 10 cm in water phantom with STD linac. All the calculations were made by using pencil beam algorithm and not AAA. Several phantom studies were done, using cylindrical water structures and compare with similar MC simulation in order to verify that the commissioning was done properly.



### **II.3.C Modification function**

After commissioning the new linac in Eclipse several phantom studies were made for different cylindrical geometries (different width and size), in order to extract the correction function  $F$ , which was used to modify the MLC openings when mFFF was being used. The final test was to plan and re-run the selected plans for three different cases each: STD, mFFF, mFFF  $\times$   $F$  correction function. The plans were selected according to two criteria. How often these cases occur in the clinical practice and the size of the used fields.

For that reason a typical prostate case (5 IMRT fields) was selected (relative small fields) as well as 2 pelvis cases (7 fields divided into two sub-fields each) due to the size of the treatment field used.

For the modification of the MLC fields the following methodology was used. MLC files, containing the control points of the dynamic MLC fields (dMLC) were extracted from the treatment planning. MLC opening were corrected according with the  $F$  function and new modified MLC files (mMLC) were imported again in the treatment planning. After that step the dose was recalculated by using the mFFF linac and the mMLC files. For the output analysis, dose profiles and DVH's were compared for both target and organ at risk between the conventional (STD) plan and the modified one (mFFF).

## **Part B: Clinical spectra production and analysis**

### **II.4. Clinical spectra**

#### **II.4.A Clinical scenarios for photon spectra**

Energy fluence photon spectra were obtained for different cases in order to investigate the potential dependence on the following factors: field size, depth, distance from the CAX of the field, IMRT versus OB fields, and split IMRT fields. These dependences were compared for a linac head assembly with and without the flattening filter.

Spectra were calculated in air at the surface of the phantom, in a homogeneous water phantom and in water with bone or lung inserts. For the homogeneous water phantom the scalar fluence was calculated at depths of 2 cm, 10 cm and 20 cm. In the case of the heterogeneous phantom, lung or bone inserts having a thickness of 10 cm and 5 cm, respectively, were placed at 5 cm and 10 cm depth in water. Spectra were calculated at depth of 20 cm for both heterogeneous cases. The spectra in the heterogeneous phantom were compared to their counterparts in the homogenous water phantom at a depth equal to the water equivalent depth.

Simulated field sizes were 3x3, 5x5, 10x10 and 14x28 cm<sup>2</sup>. Dynamic sweeping gaps (SG) representing IMRT fields of various MLC transmission content were simulated only for 10x10 cm<sup>2</sup> and 14x28 cm<sup>2</sup> field sizes. For the 10x10 cm<sup>2</sup> field the gap sizes used were 10 mm and 20 mm,

and for 14x28 cm<sup>2</sup> field the selected gaps were 1 mm, 5 mm, 10 mm and 20 mm. All the simulated cases are listed in [Table 4](#).

**Table 4:** Clinical scenarios considered at phantom surface (air) depths in water 2, 10 and 20cm and water equivalent thickness (wet) for lung and bone. Simulations done both for FFF and STD cases are marked with (+)

		depth in water (cm)					
	field size (cm <sup>2</sup> )	air	2	10	14.75 (wet for lung)	20	21 (wet for bone)
water phantom	3x3 (OB)	+	+	+	+	+	+
	5x5 (OB)	+	+	+	+	+	+
	10x10 (OB)	+	+	+	+	+	+
	10x10 (SW 10mm)	+	+	+	+	+	+
	10x10 (SW 20mm)	+	+	+	+	+	+
	14x28 (OB)	+	+	+	+	+	+
	14x28 (SW 1mm)	+	+	+	+	+	+
	14x28 (SW 5mm)	+	+	+	+	+	+
	14x28 (SW 10mm)	+	+	+	+	+	+
	14x28 (SW 20mm)	+	+	+	+	+	+
phantom with bone or lung	3x3 (OB)					+	
	5x5 (OB)					+	
	10x10 (OB)					+	
	10x10 (SW 10mm)					+	
	10x10 (SW 20mm)					+	
	14x28 (OB)					+	
	14x28 (SW 1mm)					+	
	14x28 (SW 5mm)					+	
	14x28 (SW 10mm)					+	
	14x28 (SW 20mm)					+	

Scalar fluence versus energy  $\Phi(E)$  and scalar energy fluence versus energy  $\Psi(E)$ , were calculated for different areas within and outside of the beam over a 1x1 cm<sup>2</sup> region of interest. The relationship between the two fluence distributions is given by:

$$\Psi(E) = E \Phi(E) \quad (10)$$

For each phase space coordinate, the spectra were calculated at three different locations of ROI: on the CAX, 2 cm out-of-field and 4 cm out-of-field [[Figure 6a](#)]. The spectra were analyzed in various forms: raw data without normalization, data normalized to the total area under the spectral curve, and raw spectra divided by the average dose within the particular region of interest.

In order to reduce the MC variance in out-of-field zones the following technique was used: In the case of square fields spectra were calculated at four centrally symmetric areas having the same distance (c) from the central axis and located at coordinates (0,c), (0, -c) and (c, 0), (-c, 0). The spectrum used for the analysis was the average of the spectra at the four areas [[Figure 6c](#)]. For the 14x28 cm<sup>2</sup> field the calculation area was increased from 1x1 cm<sup>2</sup> to 1x4 cm<sup>2</sup> [[Figure 6d](#)].

In clinical practice when the treatments sites are large (e.g. pelvis, or head and neck) it is common to split the IMRT field into two separate subfields for the purpose of dynamic MLC delivery [Figure 6b]. In the particular figure MLC are moving along x-axis, the directly irradiated sub-field is the one on the left and the out-of-field one is the right one. Therefore, in such cases the tumor located at the center of the left sub-field after irradiation of both sub-fields (left and right) will be partially irradiated with the direct beam and partially with the out-of-field radiation.. Hence, we present results for irradiation involving two similar abutting 10x10 IMRT fields (SG =10 mm) and compare them to results obtained for a single IMRT field at the central axis.

The incident photon energy ranged from 10keV to the maximum nominal energy of the beam (6.5 MeV). Energy binning was linear with 65keV increments for the whole spectrum. A second set of data was obtained for with different binning: every 2 keV for energy range from 1 keV – 100 keV, every 20 keV for energy range from 100 keV – 1000 keV, and every 200 keV for the rest of the energies. The second data set was used to provide a better energy resolution for the lower part of the spectrum. Spectra planes were placed at the center of the dose voxel and each spectrum was also correlated to its dose value in analysis of the data.

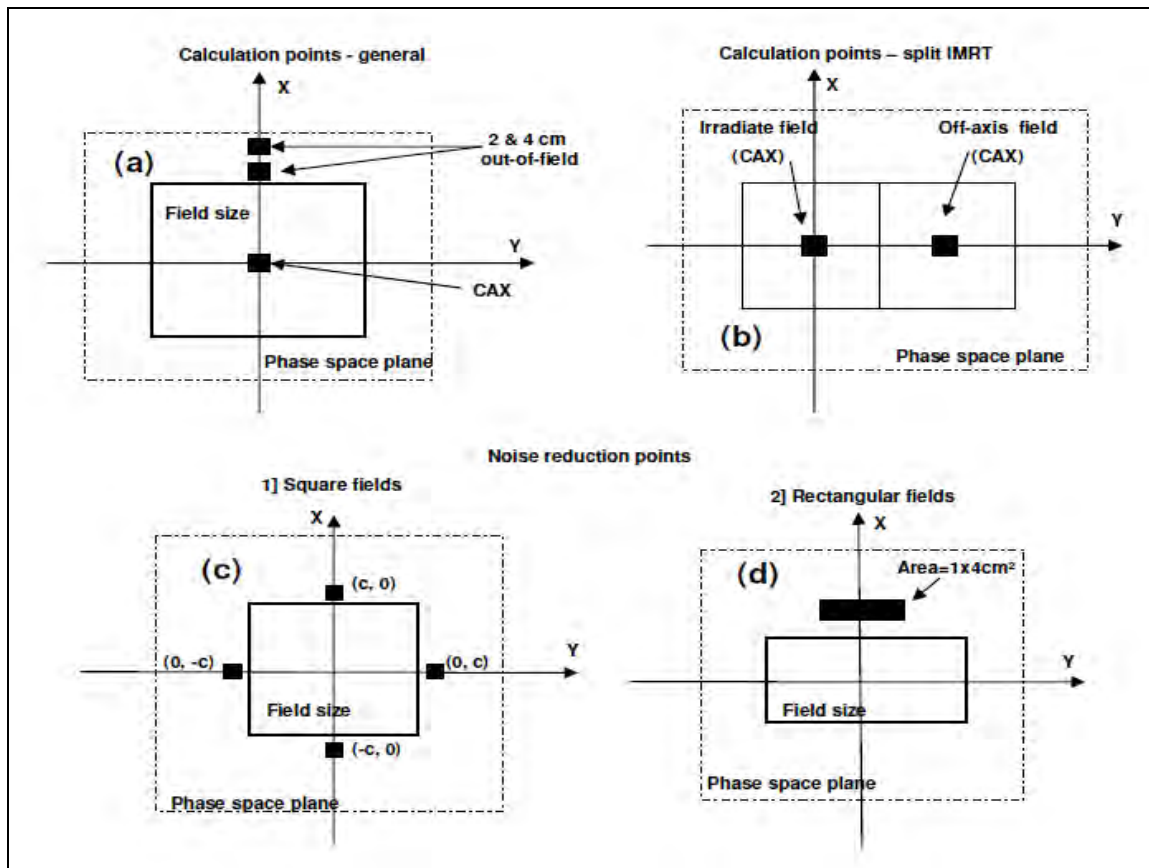


**Figure 6:** Data analysis diagram: (a) areas of spectral calculation per phase space, (b) spectra calculation for split IMRT field. Noise reduction diagrams for square fields (c) and rectangular fields (d).

## II.4.B Spectrum-weighted dose metrics

The spectrum may change significantly depending on the irradiation and beam conditions. Therefore, the impact of the beam spectrum on the dose depends on the specific application. For instance, one might be interested in the response of radiographic film under different irradiation conditions. Below we will define two simple metrics that will be helpful in the assessment of such impact: an energy-dependent dose perturbation (dose enhancement or suppression) factor,  $m(E)$ , and an effective dose perturbation factor,  $M$  for the entire spectrum. Similar metrics have been used in the past for various purposes, but they require to be redefined in view of the goals set herein. Using these two metrics and the differences between them for various irradiation conditions (e.g.  $M(\text{cond}) - M(\text{cond}_{\text{ref}})$ ,  $m(E, \text{cond}) - m(E, \text{cond}_{\text{ref}})$ ), we discuss the impact of spectral changes on the dosimetry of selected materials such as radiographic film (Kodak type AA), scintillators (gadolinium oxysulfide -  $\text{GdO}_2\text{S}_2$ ) and gold (Au) employing mass-energy absorption coefficients available in NIST tables [162].

Consider heterogeneity embedded in water phantom, which is exposed to a photon fluence of  $\Phi(E)$ . Two simple metrics of dose perturbation (enhancement or suppression) may be defined due to the presence of the embedded medium: a differential metric  $m(E)$ , which is energy-dependent, and an integral or effective metric,  $M$ , which are related as:

$$M = \int_0^{\infty} m(E) dE. \quad (11)$$

In practice, the upper limit of the above integral may be replaced by the maximum energy of the incident particles,  $E_{\text{max}}$ , assuming there is no up-scattering. For megavoltage Linacs this condition is satisfied. For a material of different composition than water (which may be an aqueous mixture or solution, denoted here by the letter  $Z$ ), inserted in a water phantom (denoted by  $w$ ), the differential metric is the ratio of the energy-dependent dose in material  $Z$  versus the total dose in water at the same spatial location,  $r_0$ , in the absence of material  $Z$ :

$$m(r_0, E) = \frac{D_Z(r_0, E)}{D_w(r_0)}, \quad (12)$$

and

$$M(r_0) = \frac{D_Z(r_0)}{D_w(r_0)} \quad (13)$$

where  $D_Z$  and  $D_w$  are the total doses summed over all energies in the spectrum in material  $Z$  and in water without the presence of  $Z$ , respectively:

$$D_Z = \int_0^{\infty} D_Z(E) dE \quad \text{and} \quad D_w = \int_0^{\infty} D_w(E) dE. \quad (14)$$

Since the spatial location is fixed, it can be dropped from the notation to preserve clarity. In charged particle equilibrium (CPE) the dose may be computed using the collisional kerma:

$$D(E) = E\Phi(E) \frac{\mu_{en}(E)}{\rho} = \Psi(E) \frac{\mu_{en}(E)}{\rho} \quad (15)$$

where  $\Psi(E) = E\Phi(E)$  is the energy fluence and  $\mu_{en}/\rho$  is the mass-energy absorption coefficient. Hence in CPE the integral and differential dose perturbation metrics may be written as

$$M = \frac{D_Z^{CPE}}{D_w} = \frac{\int_0^{E_{max}} \Psi_Z(E) [\mu_{en}(E)/\rho]_Z dE}{\int_0^{E_{max}} \Psi_w(E) [\mu_{en}(E)/\rho]_w dE} \quad (16)$$

and

$$m(E) = \frac{D_Z(E)^{CPE}}{D_w} = \frac{\Psi_Z(E) [\mu_{en}(E)/\rho]_Z}{\int_0^{E_{max}} \Psi_w(E) [\mu_{en}(E)/\rho]_w dE}, \quad (17)$$

respectively. In the above formulae, the upper limits of the energy integrals are replaced by the maximum energy of the incident particles,  $E_{max}$ .

A simplification may be afforded by the assumption that if the electron density in material Z is not substantially different from that in water, the photon spectra in these materials will also not differ substantially, hence  $\Phi_Z(E) \sim \Phi_w(E)$  and the subscripts for  $\Psi_Z(E)$  and  $\Psi_w(E)$  in equations [16] and [17] may be dropped. A similar argument can be made for the case when material Z is a thin solid embedded in the water phantom, as the fluence is continuous across the interface of Z and w. Under this assumption [eq. 16, 17] holds. Strictly speaking the quantities, which we refer to as metrics M and  $m(E)$  are not exactly dose ratios. They are approximately primary dose ratios under conditions of CPE and when the primary collision kerma can be used to represent the energy deposition. Therefore, we refer to them as metrics of dose effects rather than true dose ratios.

## Part C: Clinical spectra production and analysis

### II.5. DER for clinical spectra - optimal beam quality for NPRT

#### II.5.A General Methodology – spectral reconstruction methods

Photon spectra for a wide range of different clinical beams were obtained using the EGSnrc MC code model described in one of the above sections. These spectra, incident on a water phantom, were folded into dose kernels determined for a series of monoenergetic beams to obtain the DER for the spectral beam. The monoenergetic DER functions were derived for energies ranging from 11 keV to 6500 keV using GEANT4 MC and CEPXS/ONEDANT deterministic (DT) radiation

transport codes [35, 36, 14, 15]. By summing the monoenergetic DER kernels with weights representing the clinical beam spectra, the DER may be obtained for arbitrary beam quality. The monoenergetic DER kernels are denoted by  $DER(x,E,s)$  and the reconstructed total DER for spectral beams by  $DER(x,q,s)$ , where  $x$  is the distance from the GNP surface to the point of interest in water,  $E$  is the energy of the monoenergetic beam,  $s$  is the GNP size, and  $q$  is a beam quality parameter. Note that although the term “dose-enhancement-factor” has been used in several studies [31, 89-91], it is not uniformly defined in the published literature [32, 75-78, 89-91]. In this study DER represents the ratio of dose when nanoparticles are present to the dose when only water is present  $DER = D_{GNP}/D_{water}$ , which depends on several clinical factors impacting the beam quality ( $q$ , which includes energy), the distance from the surface of the GNP ( $x$ ), and the GNP thickness ( $s$ ). In this way, for each ( $s$ ) an energy dependent DER kernel was obtained.

In the analysis, the spatial dependence of DER with respect to various potential cellular and sub-cellular targets was considered. Specifically, ranges from a few nm to 2  $\mu$ m were examined, corresponding to various cellular target sizes: DNA chain (1-2 nm), cell membrane (10 nm), and entire endothelial cells (1-2  $\mu$ m). This two step approach with different codes for macroscopic and microscopic scales has been adopted in various other publications [31, 76 and 78].

### **II.5.B Deterministic and Monte Carlo simulations**

The GEANT4 code was tested against experimental and other reference data. We used this code for computations in the microscopic scales. CEPXS/ONEDANT was developed by Sandia and Los Alamos National Laboratories and it has been extensively tested and applied to radiotherapy problems in the past [14, 15]. We used it for computations in the nanometer and micrometer ranges. In order to ensure that the transition from microscopic to nanoscopic analysis is correct, further verifications of the CEPXS/ONEDANT code were performed against GEANT4 and published data for EGSnrc, GEANT4 and MCNP5 simulations.

Calculations of DER were performed for two GNP thicknesses (10 nm and 100 nm), for the monoenergetic and selected spectral beams, and for four different depths in water (0 (surface), 2, 10 and 20 cm). Calculations of spectral beams at different depths were used to verify the aforementioned methodology, which was subsequently applied to about 480 spectral cases ( $q=4$  field sizes 3x3 - 14x28 cm<sup>2</sup>, 4 depths 0 - 20 cm, 2 linac types with and without the flattening filter, open beam (OB) vs. IMRT and split-IMRT, 4 MLC gap sizes 1-20 mm, 3 different areas of interest per case in/ out-of-field). The linac (Varian 6EX), which was used for the spectral production, was simulated using the EGSnrc code with and without flattening-filter (STD and FFF, respectively) for both in- and out-of-field areas [60].

Figure 7 shows a schematic overview of the cellular target geometry and the GNP location. Both



GEANT4 and CEPXS/ONEDANT were tested against each other. CEPXS/ONEDANT was used to generate high spatial resolution and energy discrimination  $DER(x, E)$ , while GEANT4 yielded lower resolution  $DER(x, E)$  for selected energies. The vast amount of cases in combination with the time limitations of GEANT4 simulations makes practically impossible to generate  $DER$  for the cases reported by relying on MC simulations. The required computation time is many orders of magnitude greater than that using DT simulation. In relatively simple geometries, such as seen in the case of nanoparticles, the deterministic approach has several advantages over the MC technique: much faster calculation times, no random noise, and accurate cross sections down to 100 eV and sub-nanometer spatial resolution, limited only by computer memory and simulation refinements. Thus the monoenergetic dose kernels from CEPXS/ONEDANT had high spatial resolution and no noise, contrary to GEANT4 kernels.

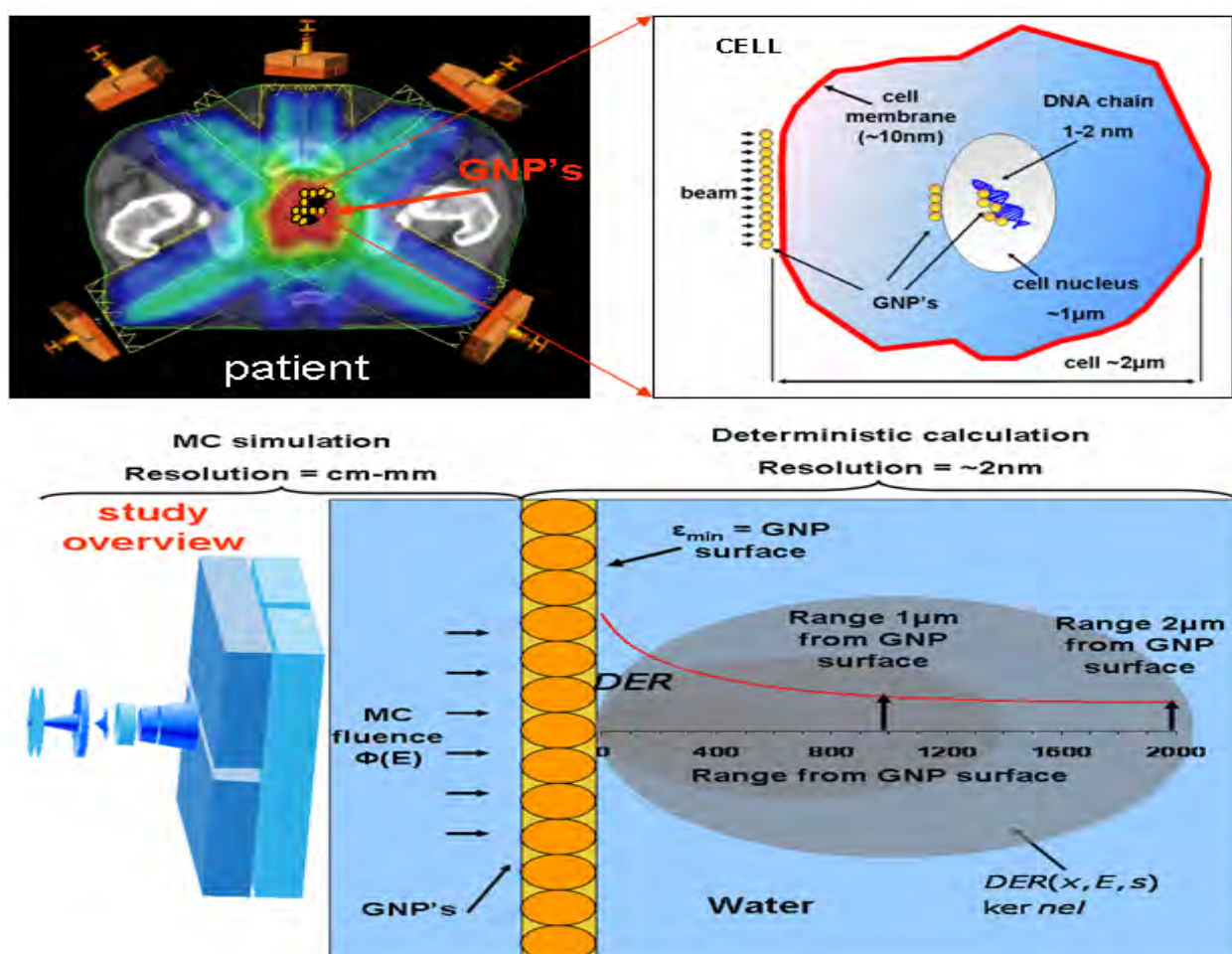


**Figure 7:** Schematic representation of GNP aggregating in the treated macroscopic volume (upper-left) and a single cell (upper-right) and located near different potential cellular targets (membrane, nucleus and DNA). Lower part shows a schematic representation of  $DER(x, q$  and  $s)$  computed for monoenergetic spectral cases.

## III. RESULTS

### Part A

#### III.1. Monte Carlo simulation of the medical linac

##### III.1.A MC Model verification for FFF and STD linac

###### III.1.A.i. Commissioning of STD linac

Blueprint information provided by Varian and published parameters were used as a starting point for STD linac. After that, adjustments were made to reach an agreement between GBD and MC data. PDDs [figure 9a], OARs [figure 10] and  $S_{\text{tot}}$  [figure 9b] were measured for SSD=100 cm (SSD=95 cm for  $S_{\text{tot}}$ ) and for OB field sizes starting from 4x4 to 40x40 cm<sup>2</sup>. For all the data comparison has been done with GBD in depths of  $d_{\text{max}}$ =1.5, 5, 10 and 20 cm. The maximum difference for all the in-field points between GBD and MC was below 1-2%. Figure 8 shows the drawing of the linac model as were extracted from EGSnrc code.

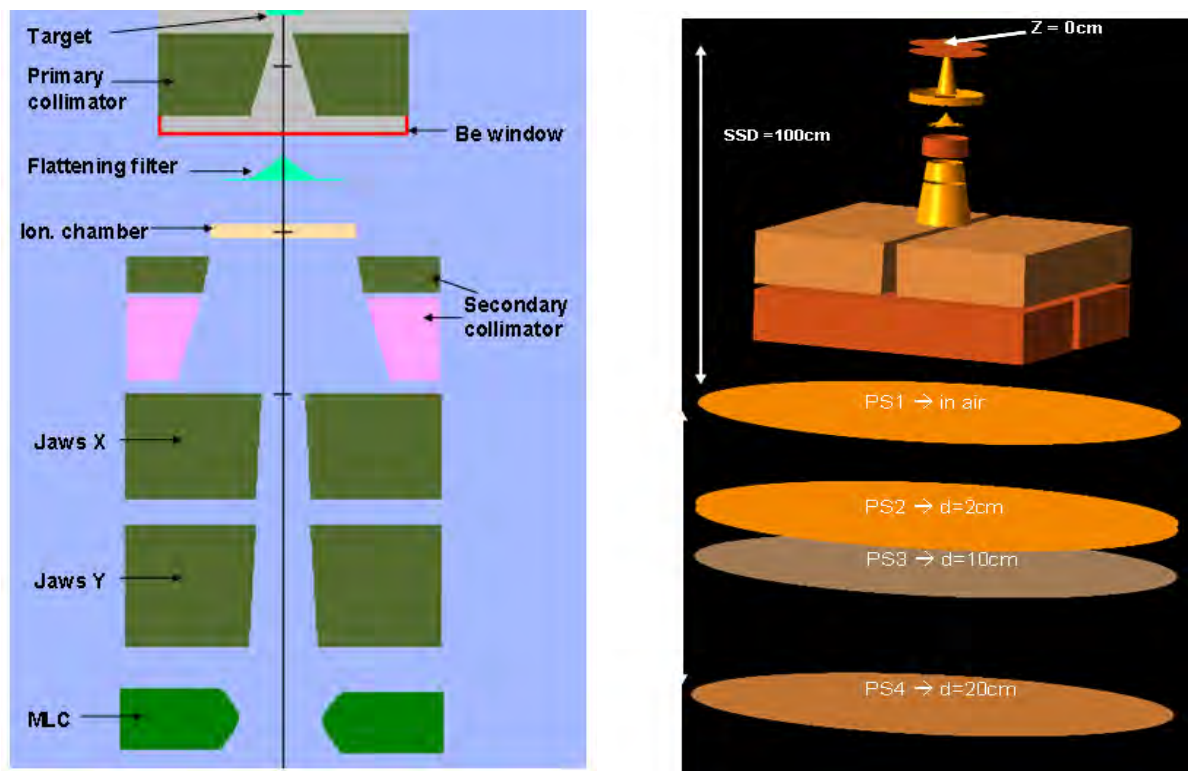


**Figure 8:** Graphical representation of the linac MC model at the x-z plane showing the different simulated components of the head assembly (left). On the right figure the same model is shown in 3D for an SSD = 100 cm set up. In the same figure (right) the planes of phase space scoring are shown.



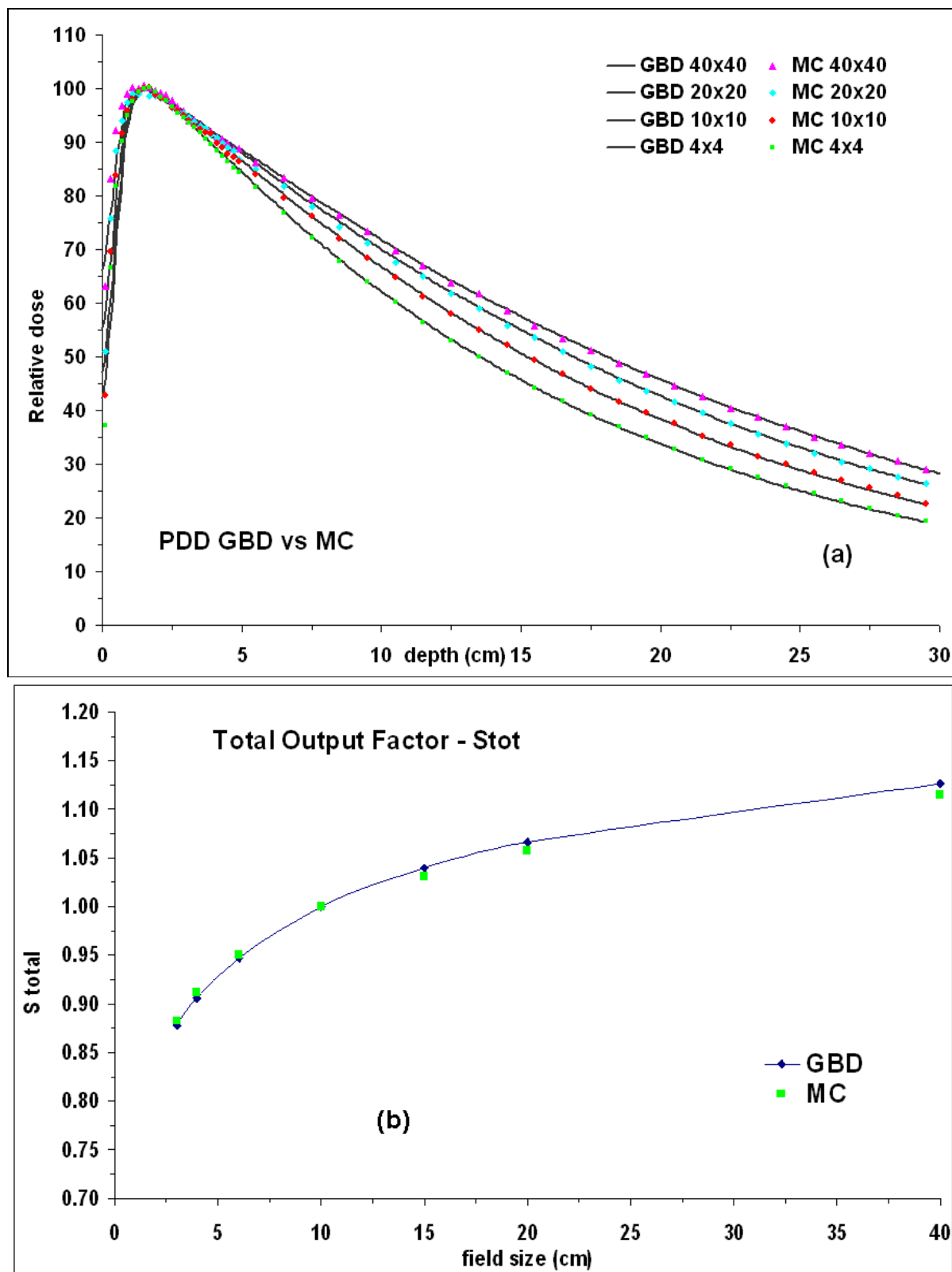


**Figure 9:** a] PDD comparison of GBD vs. MC simulation for various field sizes , b] Output Scatter factor comparison of GBD measurements and MC simulation results for field sizes of 3x3 – 40x40 cm².

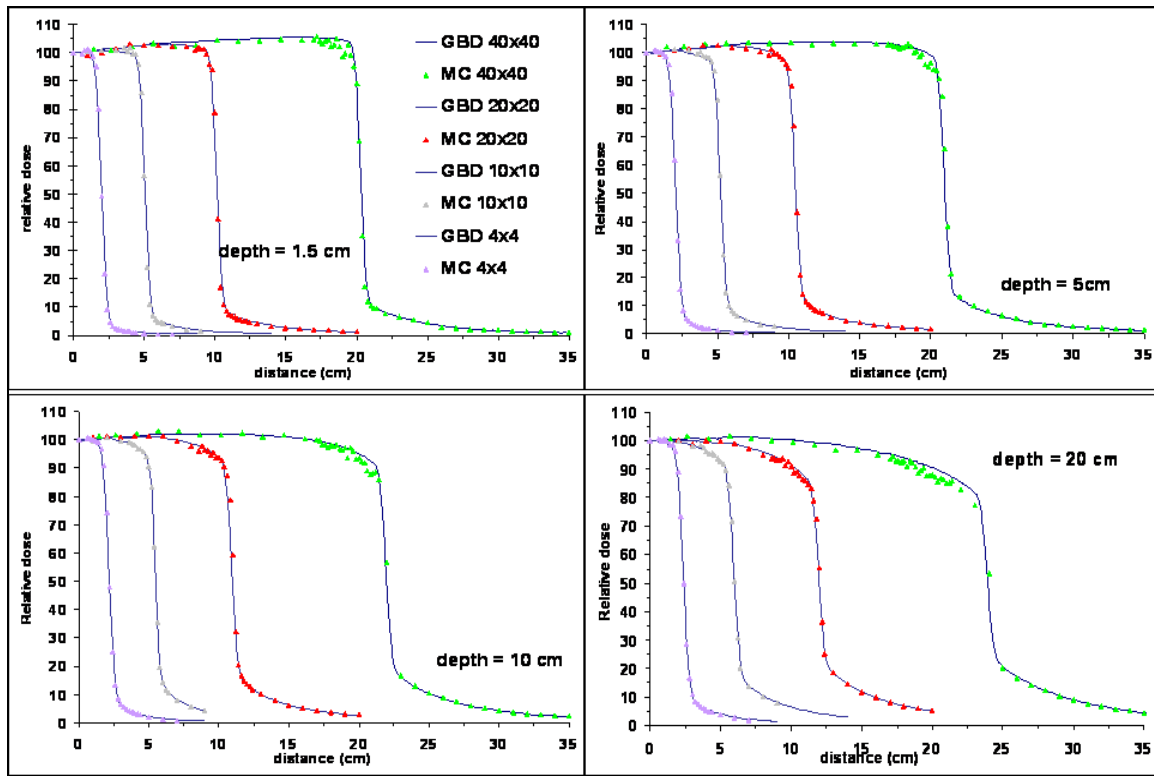


**Figure 10:** OAR comparison of GBD vs MC simulation for various field sizes [4x4 – 40x40 cm<sup>2</sup>] and depths [dmax=1.5 cm, 5, 10 and 20 cm].

### III.1.A.ii. Commissioning of model for IMRT

As it was reported in the literature [159] transmission through the MLC has a field and depth dependence and can be expressed by a dose ratio ( $R_{cMLC}$ ) between close MLC and OB according to the formula:

$$R_{cMLC} = T(d) \times (1 + \beta(d) \times c_{eff}^2) \quad (18)$$

$$c_{eff} = \frac{(1 + k) \cdot c_x \cdot c_y}{k \cdot c_x + c_y} \quad (19)$$

where,  $T(d)$  is the direct MLC transmission,  $\beta(d)$  is an MLC scatter parameter and  $c_{eff}$  is an area of an effectively square field, which is defined by the field dimensions ( $c_x, c_y$ ) and collimator exchange factor  $k$ .

Measured MLC transmission was  $T_{exp} = 0.0174$  for a 12x28 cm<sup>2</sup> field size at SSD = 95 cm and depth of  $d = 5$  cm. MC transmission for the same field size, depth and distance from the source was  $T_{MC} = 0.0173$ . Histories were chosen in order to keep statistical uncertainty below 1% in the voxel of measurement. Comparison between simulated and calculated value show that the selected density and interleaf air gap are matching with 0.57% difference.

As mentioned in II.1.B.iv two different sweeping gap patterns were tested. Calculated dosimetric gap ( $\Delta G$ ) for the first sweeping gap pattern (leaves half-inside-half-outside of the field) was 0.147 cm. The same value calculated with MC data was 0.089 cm (10x10 cm<sup>2</sup>) field and 0.114 cm (14x28

cm<sup>2</sup>). For the second pattern (leaves all-out of the field)  $\Delta G$  was calculated for two field sizes (10x10 and 12x28 cm<sup>2</sup>). Measured dosimetric gap for that pattern was 0.147 cm (10x10 cm<sup>2</sup>) and 0.154 (12x28 cm<sup>2</sup>). Calculated  $\Delta G$  derived from MC was 0.099 cm (10x10 cm<sup>2</sup>) and 0.097cm (12x28 cm<sup>2</sup>) respectively. **Figure 11** shows the comparison between ionization chamber measurements and MC simulation for all testes field sizes, gap sizes.

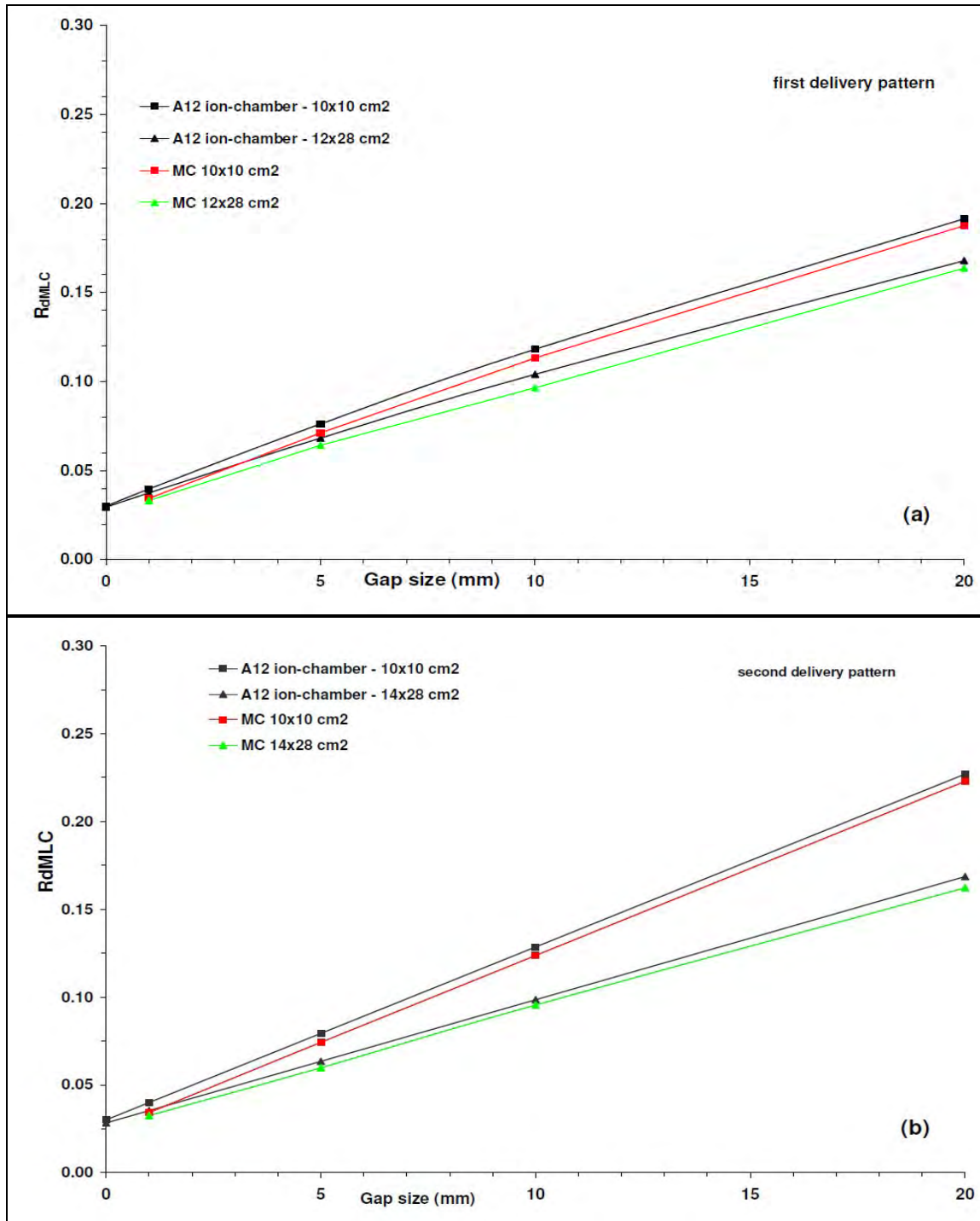


**Figure 11:** Comparison between MC and experimental data (ionization chamber A12) for dynamic sweeping gap tests **a)** first delivery pattern, **b)** second delivery pattern, of different gap and field size.

### III.1.A.iii. Commissioning of model for out-of-field area

For validating jaw transmission simulated and measured dose were compared at 5 different points. Those points were located in different out of the field distances. Open beam area forming a  $1 \times 1 \text{ cm}^2$  was chosen with MLC parked and forming a field  $1.2 \times 1.2 \text{ cm}^2$ . Jaws density was determined to be  $17.5 \text{ g/cm}^3$ . Simulated results both for STD and FFF linac agreed with measurements when MLC were forming a field of  $1.2 \times 1.2 \text{ cm}^2$ . The only disagreement existed for a point 22 cm from the center. That point was close to the physical end of MLC so there was an increase in dose as measurement results show in that area. EGSnrc simulates cylindrical geometries and cannot accurately model the physical back boundary of the modules used for modeling jaws and MLC. In order to match peripheral dose points affected by the back boundaries of collimator structures, component modules used in the simulation extended by adding more material in their back boundaries. Because of that code could not accurately calculate dose in that point which no material was present.

Peripheral dose validation of STD linac showed that the maximum difference between measurements and MC is 10% for all points of measurement up until 30cm from the center of the field. After 30cm distance MC seems to underestimate dose 50% to 250%.

### III.1.A.iv. Commissioning of FFF linac

FFF linac data (PDD, OAR and  $S_{\text{tot}}$ ), for different field sizes and depths, were simulated with the same set up (SSD=100 cm) as the one used for STD linac. **Figure 12a** shows PDDs for different field sizes. A  $40 \times 40 \text{ cm}^2$  and  $4 \times 4 \text{ cm}^2$  fields for STD linac were added for comparison reasons. **Figure 12b** shows OAR profiles in comparison with a  $40 \times 40 \text{ cm}^2$  profile of STD linac (depth of 5cm). In the same plot measurements with MatriXX for a  $10 \times 10 \text{ cm}^2$  field were added as an extra way of verification of FFF linac model. **Figure 12c** shows  $S_{\text{tot}}$  (SSD =95 cm and depth of 5 cm) for FFF linac in comparison with the  $S_{\text{tot}}$  of STD linac.

Ionization chamber measurements showed that dose rate of FFF linac increases by a factor of about 2.1, in the case of a  $10 \times 10 \text{ cm}^2$  field size and at depth of 5cm (SSD=95 cm). Calculation of the same factor, derived from MC, was 1.9 under the same irradiation conditions.

Same simulations were made for the first sweeping gap pattern and for FFF linac with STD energy and modified energy. Transmission decreases by about 13.0% after removing flattening filter and resumes its original value after modification of the electron beam energy. All the changes described above also affect sweeping gap results. Results show that  $R_{\text{SG}}$  ratio values for FFF linac are lower than the ones for STD linac. Energy modifications increase  $R_{\text{SG}}$  values to their original (STD linac) value. All  $R_{\text{SG}}$  described changes (1<sup>st</sup> pattern,  $14 \times 28 \text{ cm}^2$ ) are plotted in **figure 12d**. Statistical uncertainty due to simulation noise was less than 1.4% for all calculated ratios

and for the voxel of measurement. Table 5 summarizes T and  $\Delta G$  values for all three types of linacs: STD, FFF and mFFF.

Comparison between simulations and measurements show that agreement for in-field points are below 2% for all the fields. For out-of-field points differences between MC and measurements varies with field size and distance from the center of the field. For fields large than 6x6 cm<sup>2</sup> it is 5-16%. Discrepancies are increased as we go to larger fields and bigger distances. The largest differences were found for field 1x1 cm<sup>2</sup>, with MLC parked, and larger fields for points further than 30 cm from the edges of the treatment field (180 - 250%). A more detail analysis of those discrepancies is provided in the discussion section. All the PD measurements for FFF and STD linac are showed in figure 13a (1x1 cm<sup>2</sup> field) and figure 13b (6x6 to 30x30 cm<sup>2</sup>) below.

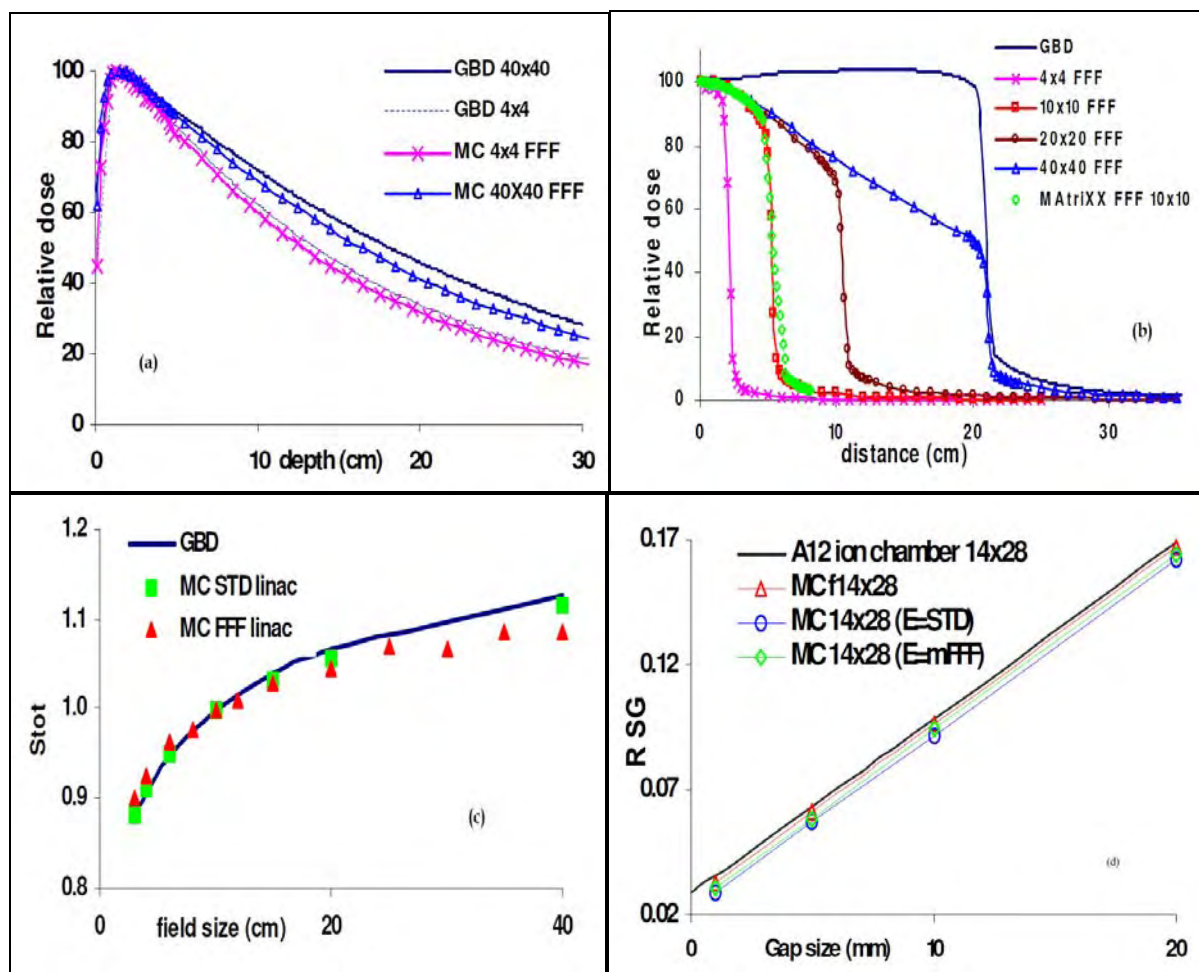


**Figure 12:** Comparison between Golden Beam Data (GBD) and Monte Carlo (MC) FFF linac simulation: (a) PDDs (field sizes 4x4 and 40x40 cm<sup>2</sup>) (b) OAR (field sizes 4x4, 10x10, 20x20, 40x40 cm<sup>2</sup> and depth of d=5 cm). MatriXX measurements for a 10x10cm<sup>2</sup> were added (c) Stot, SSD = 95 cm depth d = 5 cm. (d) Sweeping Gap ratio RSG comparison for different gap sizes (field 14x28 cm<sup>2</sup>), between measurements and MC simulation (STD, FFF and mFFF linac).



**Table 6:** T and  $\Delta G$  values for STD and FFF linac with E=ESTD and E= mFFF.

<i>Transmission</i>		<i>Dosimetric gap - Pattern I</i>	
		linac	$\Delta G$ (10x10) (mm) $\Delta G$ (14x28) (mm)
linac	T value		
Measured STD (E=E <sub>STD</sub> )	0.0174	Measured STD (E=E <sub>STD</sub> )	0.147    0.148
MC STD (E=E <sub>STD</sub> )	0.0173	MC STD (E=E <sub>STD</sub> )	0.089    0.114
FFF (E=E <sub>STD</sub> )	0.0151	FFF (E=E <sub>STD</sub> )	0.055    0.036
FFF (E=E <sub>ADJ</sub> )	0.0173	FFF (E=E <sub>ADJ</sub> )	0.079    0.087
		<i>dosimetric Gap - Pattern II</i>	
		linac	$\Delta G$ (10x10) (mm) $\Delta G$ (12x28) (mm)
		Measured STD (E=E <sub>STD</sub> )	0.147    0.154
		MC STD (E=E <sub>STD</sub> )	0.099    0.097

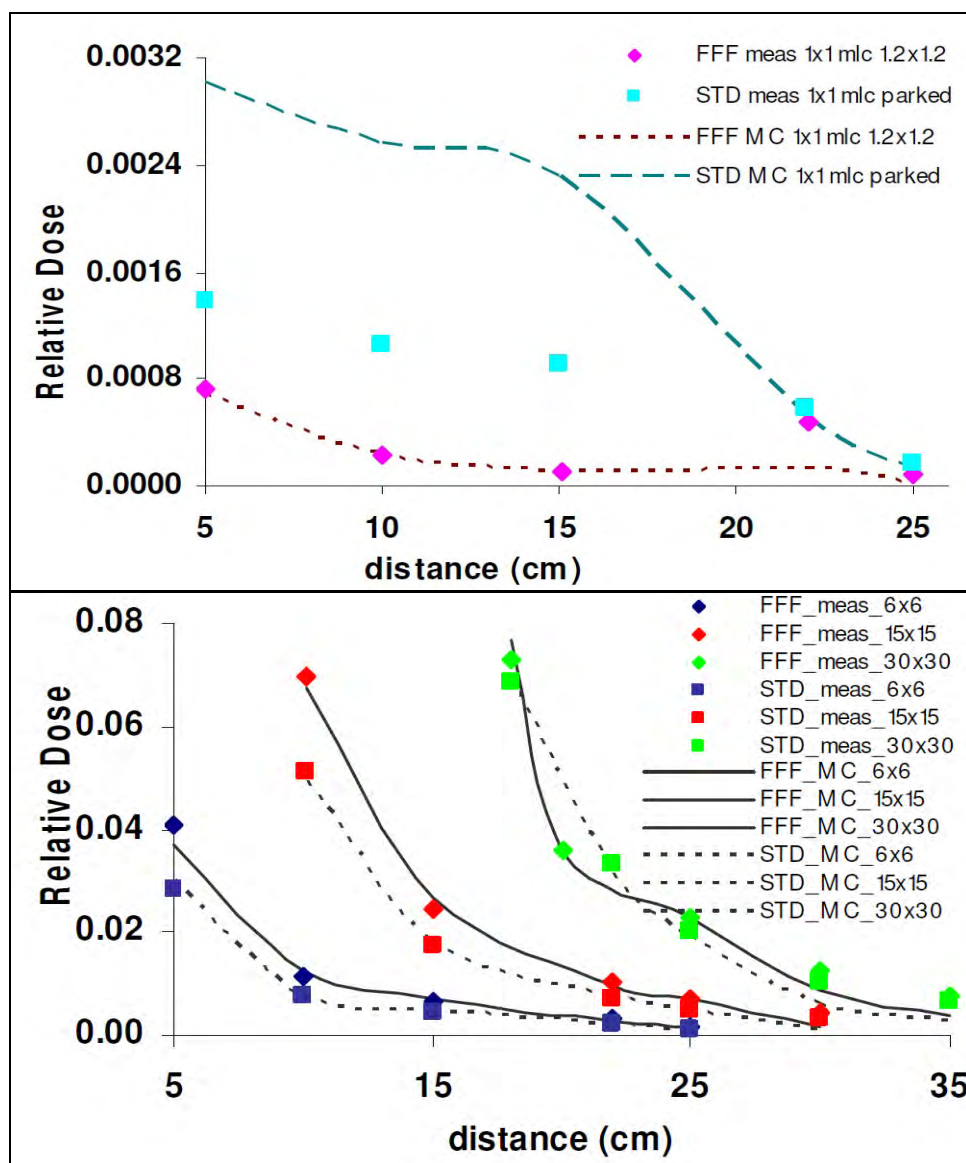


**Figure 13:** (a) Comparison between ionization chamber and MC for 1x1 cm<sup>2</sup> field, with MLC parked and MLC forming a field 1.2x1.2 cm<sup>2</sup> (depth of 5cm and SSD =95 cm). All the data were divided with central axis measurement of a 10x10 cm<sup>2</sup> field, (b) comparison between ionization chamber and MC for peripheral dose points (depth of 5 cm and SSD = 95 cm), normalized on the central axis measurement of a 30x30 cm<sup>2</sup> field. Data show both FFF and STD linac.

## III.2. Beam line modification

### III.2.A modifying the energy of a FFF linac

According to the results, in order to match accurately FFF with STD PDD curves, the modified energy should be slightly varied with field size. For small and medium size fields (up to 15x15 cm<sup>2</sup>) is about 8.0 MeV and for larger field sizes (up to about 30x30 cm<sup>2</sup>) it is about 8.5 MeV (Figure 14). For very large fields (40x40 cm<sup>2</sup>) the modified energy has to be increased even more, however, it can be assumed that in practice the nominal energy is 8.0-8.5 MeV. Increasing energy changes dose ratio between STD and FFF linac. Dose ratio increased from 1.9 (energy 6.5 MeV) to around 3.5 (energy 8 MeV) and 4 (energy 8.5 MeV). Because of the even larger dose rate the benefit in treatment time is even larger (Table 7).

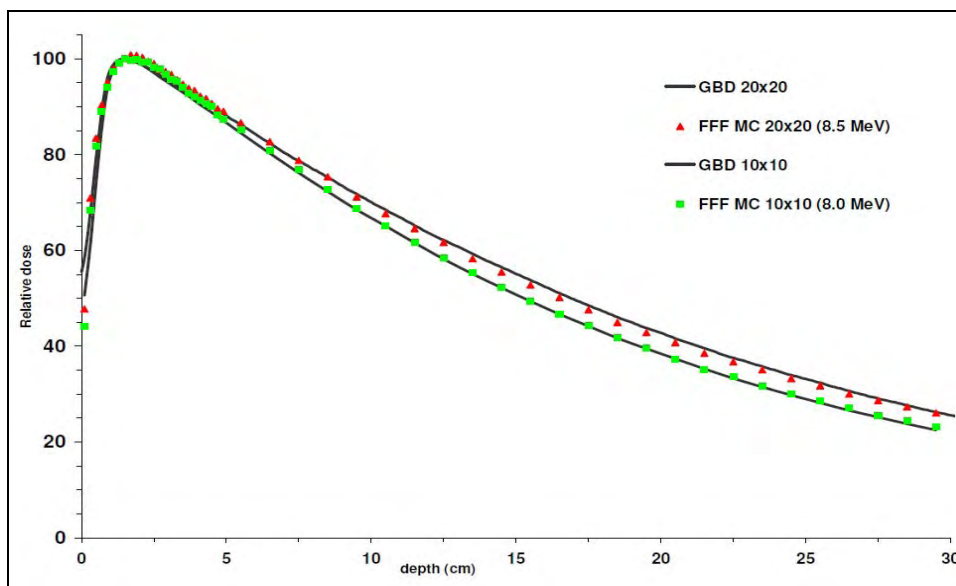


**Figure 14:** Penetration matching for STD and FFF linac for different field sizes. For smaller and medium field sizes (until 15x15 cm<sup>2</sup>) the modified energy is 8 MeV and 8.5 MeV for larger field sizes.

**Table 7:** Dose ratios for STD energy and modified.

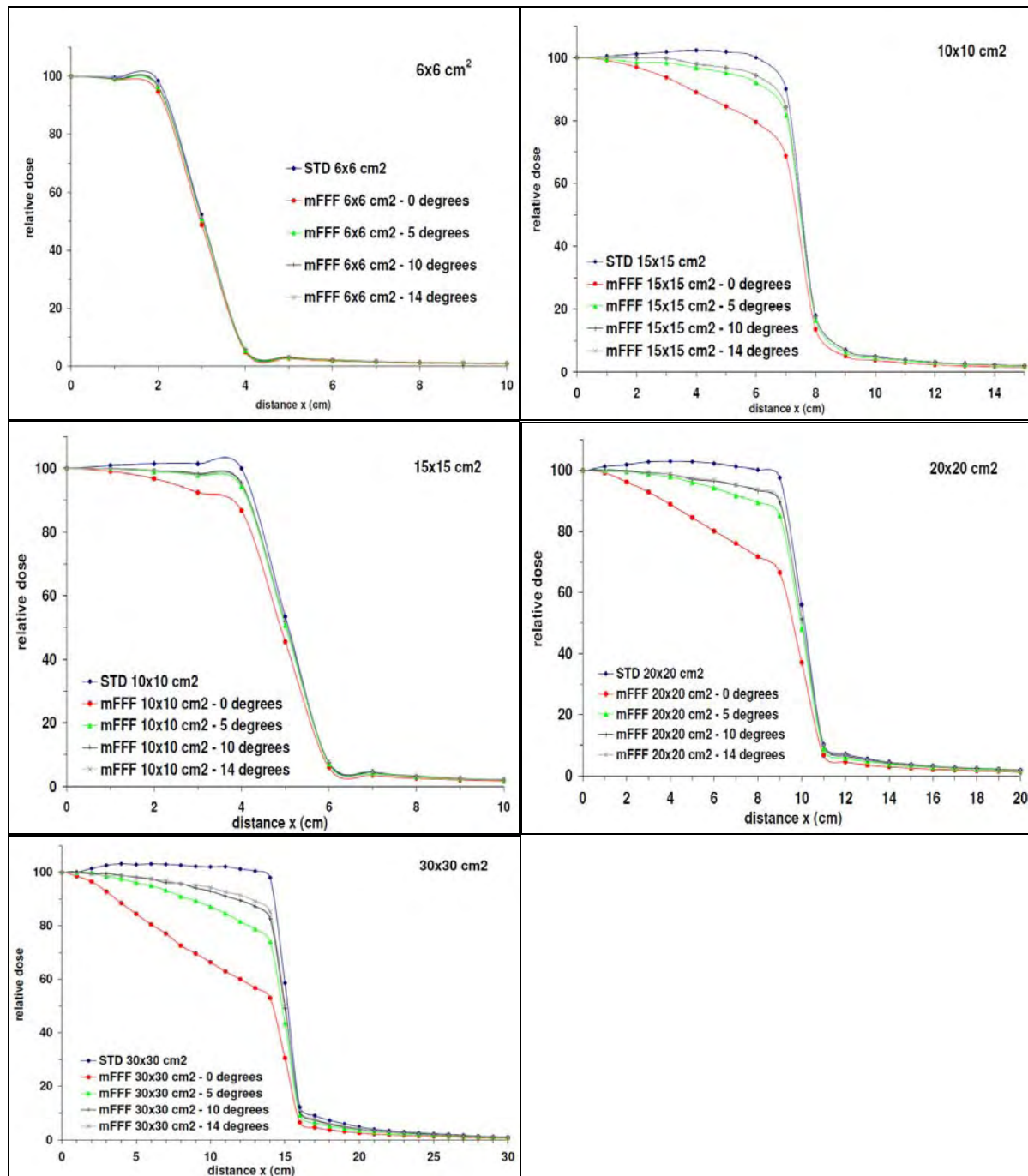
Field size (c <sub>x</sub> xc <sub>y</sub> )	FFF <sub>E=STD</sub> / STD	mFFF/ STD
6x6	1.9 (E=6.5 MeV)	3.6 (E= 8 MeV)
10x10	1.9 (E=6.5 MeV)	3.5 (E= 8 MeV)
15x15	1.9 (E=6.5 MeV)	3.4 (E= 8 MeV)
20x20	1.9 (E=6.5 MeV)	4.1 (E= 8.5 MeV)

### III.2.B Flattening of FFF beam by de-focusing the electron beam

For the adjusted energy the spatial and angular spread of the electron beam hitting the target changed (field sizes 6x6, 10x10, 15x15, 20x20 and 30x30 cm<sup>2</sup>). Different combinations of spatial spread values 2 x (σ<sub>x</sub>, σ<sub>y</sub>), 4 x (σ<sub>x</sub>, σ<sub>y</sub>) and angular spread values σ<sub>θx</sub>= σ<sub>θy</sub>= 0°, 5°, 10° and 14° were tested. Profile flatness of FFF linac is insensitive to changes of (σ<sub>x</sub>, σ<sub>y</sub>). For values over 2 x (σ<sub>x</sub>, σ<sub>y</sub>)

flatness area gradient increases as electron beam spatial dimension becomes so large that it is effected by the primary collimator.

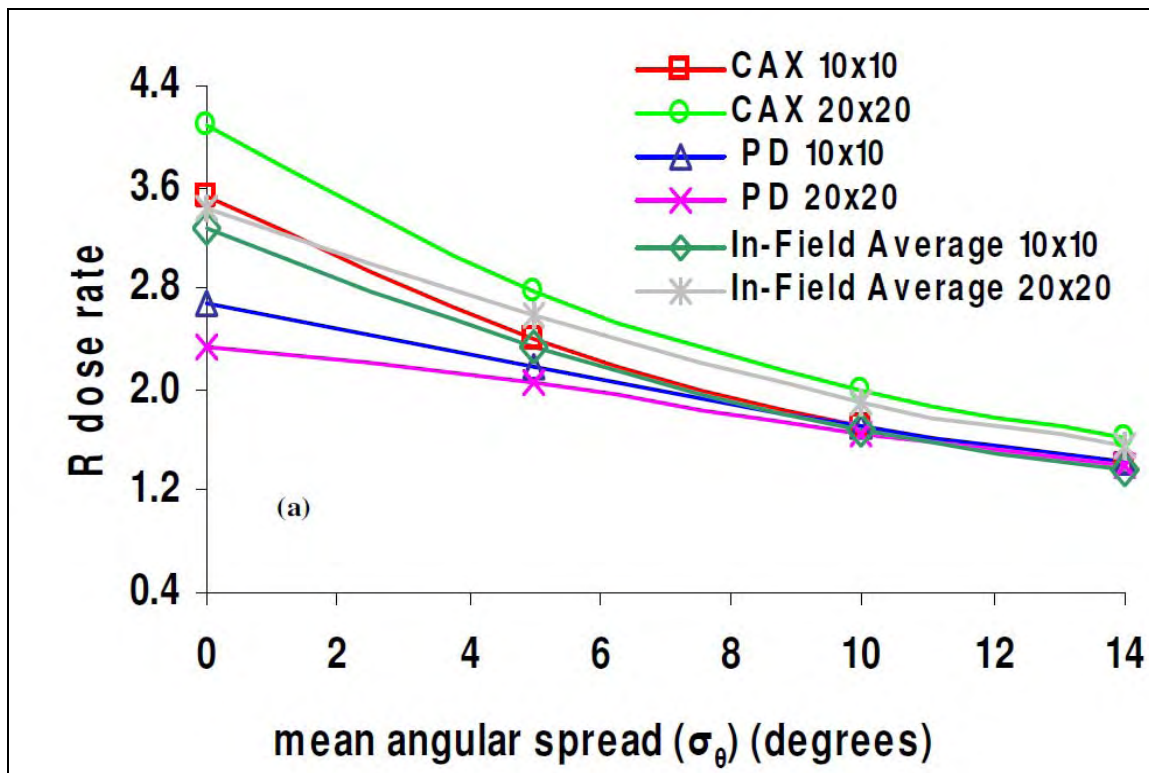
By increasing mean angular spread ( $\sigma_{\theta_x}$ ,  $\sigma_{\theta_y}$ ) of the electron beam, photon beam flatness improves [Figure 15]. This beneficial flattening of the beam depends on field size and energy, as energy varies slightly with different field sizes. Figure 15 shows that spread  $\geq 14^\circ$  affects the edges of the field. According to this figure dose at the edges of the field (point 10cm from the center) is almost 20% lower than dose for spread of  $10^\circ$ . The reason for that is that values of this spread angle is close to the opening of the primary collimator.



**Figure 15:** OAR comparison for different mean angular spread values (0 -  $14^\circ$ ) of the e-beam (field sizes 6x6 - 30x30 cm<sup>2</sup>, depth of 5 cm, SSD = 100 cm).



For field sizes below 6x6 cm<sup>2</sup> there is no practical difference between different angular spread values. It can be claimed that no flattening is needed for such small fields. Moving to larger field sizes (larger than 10x10 cm<sup>2</sup>) non-zero values of mean angular spread have to be used (over 5°) in order to achieve a better flatness. However, while the mean angular spread angle increases, dose rate decreases and peripheral dose increases. Thus, the question is how to keep the benefit of dose rate (treatment time) in an FFF linac. Figure 16a shows how  $R_{\text{dose ratio}}$  changes with mean angular spread at the center of the field and in peripheral dose area. This ratio has only energy and field size dependence and practically remains the same for different depths. In figure 16a two different groups of lines are observed one for fields smaller than 15x15 cm<sup>2</sup> and one for fields larger than 15x15 cm<sup>2</sup>. The reason for that is the fact that two modified energies were used 8 MeV (fields ≤15x15 cm<sup>2</sup>) and 8.5 MeV (fields >15x15 cm<sup>2</sup>). Plots depict that about 50% benefits in dose rate at the central axis can be obtained even for a 20x20 cm<sup>2</sup> field size with spread of 10°. In the plot (Figure 16a) an average dose rate ratio of the in field area was calculated for each field size and for different angular spreads. The calculated data are presented for fields 10x10 and 20x20 cm<sup>2</sup>, showing how dose rate vs angular spread change in comparison with the dose rate on the central axis. Average in field dose rate seems to be smaller than the central axis one.



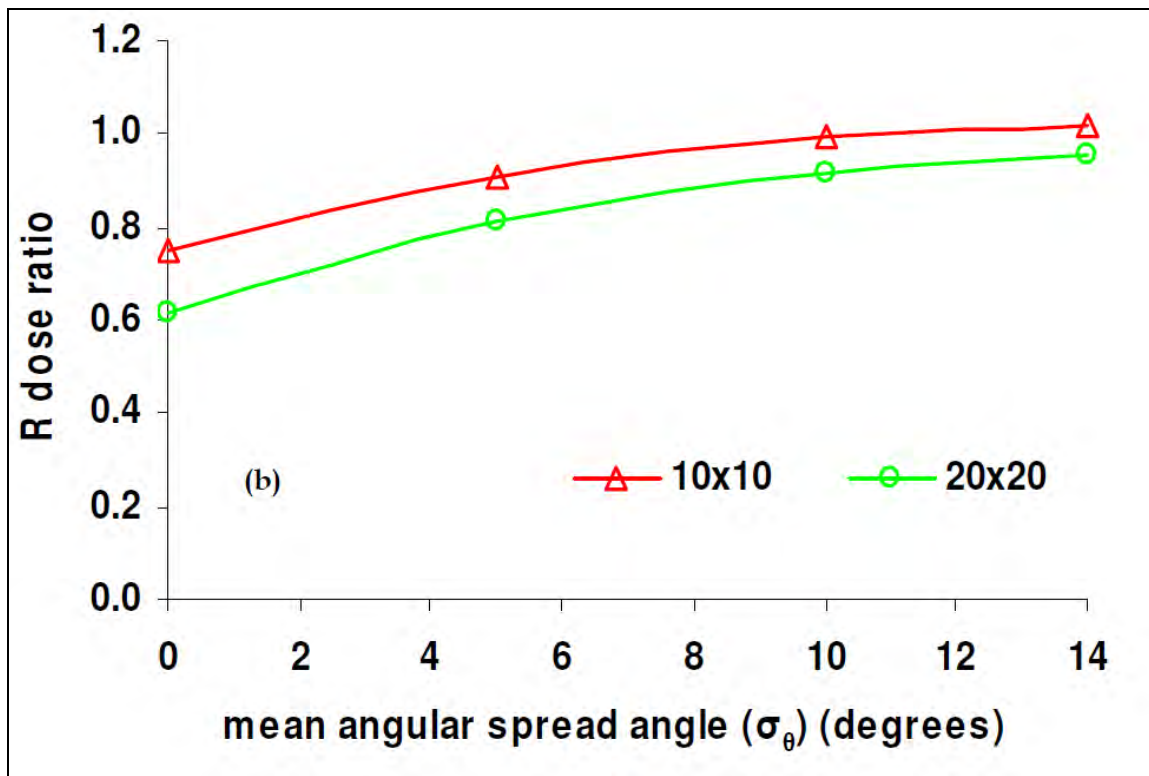


**Figure 16:** (a) Decrease in dose rate in the center of the field and in average in field area and in the peripheral dose region as mean angular spread increases, for different field sizes and for both modified energies (8 and 8.5 MeV) at depth of 5 cm and for SSD = 95 cm, (b) peripheral dose ratio increase with increase of mean angular spread angle, for the same irradiation conditions (same dose at the center of the field) and for both modified energies (8 and 8.5 MeV) at depth of 5cm and for SSD = 95 cm.

**Figure 17a** (fields' 10x10 and 30x30 cm<sup>2</sup>) shows how PD changes with field size and angular spread for STD and mFFF linac. Data are normalized in such a way that maximum dose is delivered at the center of the field. According to the figure it is clear that PD dose for mFFF linac with angular spread of 0° is smaller than STD linac. Also plots show that as  $\sigma_\theta$  increase PD approaches dose of STD. As we move to larger field sizes maximum  $\sigma_\theta$  value, that can be used, increases. The same data are presented in **figures 17b** but with a different way. In that figure no normalization has been applied in order to show how increase of  $\sigma_\theta$  affects peripheral dose with field size. According to the figure increasing mean angular spread decreases peripheral dose. That is expected as according to  $R_{\text{dose ratio}}$  calculations increasing value of  $\sigma_\theta$  decreases dose rate, so less dose is delivered in these areas for the same irradiation time and delivered dose. **Figure 16b** shows how  $R_{\text{dose ratio}}$  changes with mean angular spread and field size when we deliver the same dose in the center of the field for both STD and mFFF linac. The plot shows two different groups of data because two adjusted energies were used. The difference between those data and the ones presented in **figure 16a** is the way of normalized. **Figure 16b** shows data normalized in the central axis (CAX). A more detailed analysis will take place at the discussion section regarding these graphs.

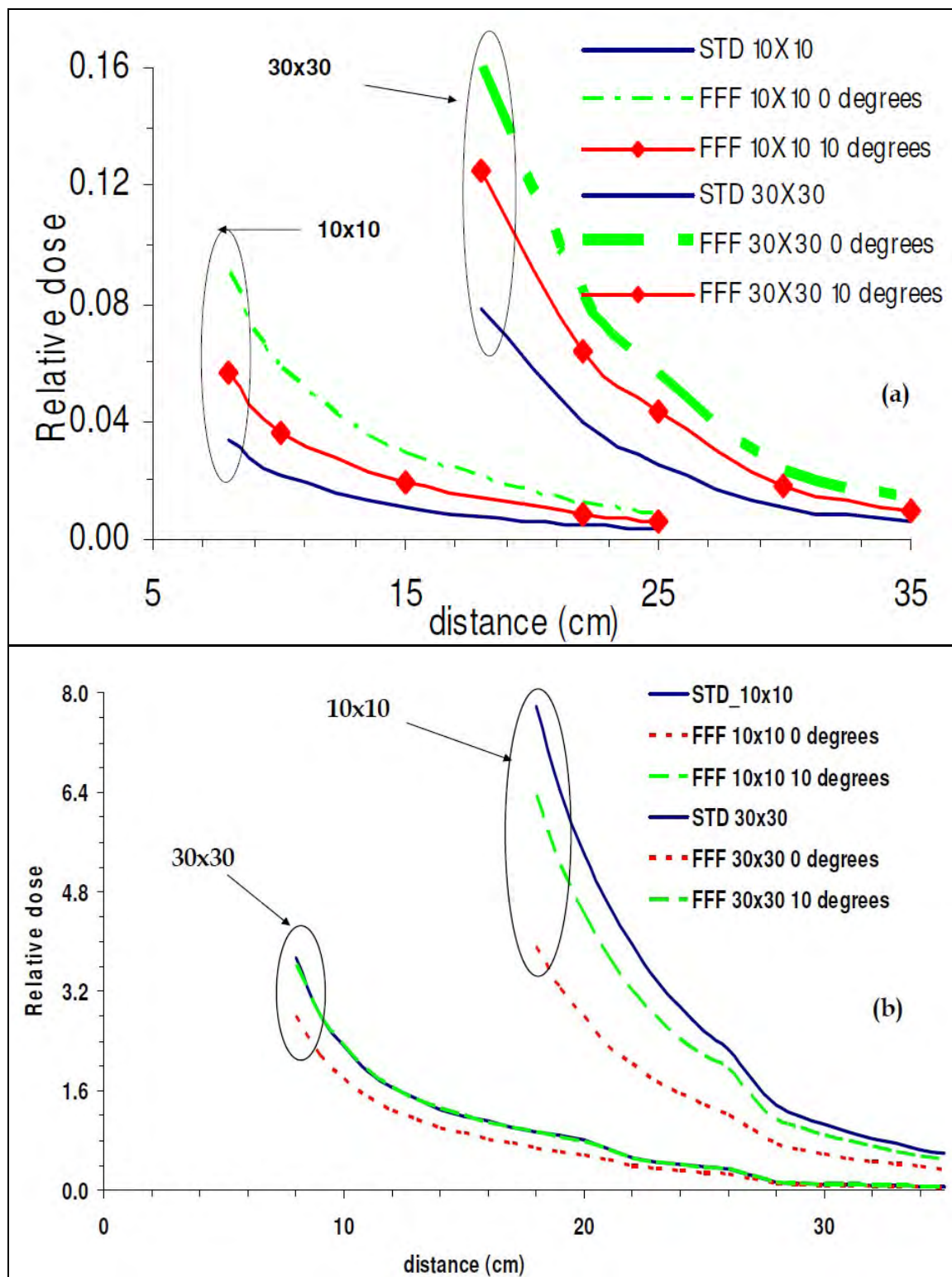


**Figure 17: (a)** decrease PD benefit with increase of the mean angular spread for field sizes 10x10 cm<sup>2</sup> and 30x30 cm<sup>2</sup> for depth of 5 cm and for SSD = 95 cm (same dose delivery at the center of the field) **(b)** PD comparison between STD linac and mFFF linac with different  $\theta$  values (0°-10°) for field 10x10 and 30x30 cm<sup>2</sup> (depth 5 cm, SSD = 95 cm). Data were normalized in such a way that maximum dose is delivered at the center of the field.

### III.2.C Unflatness of FFF linac

In order to characterize beam flatness for FFF linac vs STD linac a heuristic formula was used [Equation 9], which describes both open beams and sweeping gap fields for all depth and field sizes and for the in field area. Table I below summarizes the numerical values of the parameters ( $\beta, n$ ). Regarding open fields the formula accuracy is within about 1% for all fields and depths. Inaccuracies of around 2-3% exist only for smaller field sizes (6x6 cm<sup>2</sup>) but these fields already have flat enough profiles. For the cases of the sweeping gap tests (fields 10x10 cm<sup>2</sup> and 14x28 cm<sup>2</sup>) and gap sizes of G=10, 20 mm formula has accuracy of 2-3% due to larger noise in the MC data.

**Table 8:** Parameters values for  $R_{unif}$  function

Parameter	Value
$\beta$	0.013
$\beta_0$	0.023
$\beta_1$	0.021
$\gamma$	1.603
$\gamma_0$	$36.68 \times 10^{-4}$
$\gamma_1$	$23.83 \times 10^{-4}$

Figure 18 shows a graphical example how the infield dose ratio between FFF and STD profiles was calculated. Figure 19 shows comparison between the theoretical formula and the calculated ratio for various field sizes and depths.

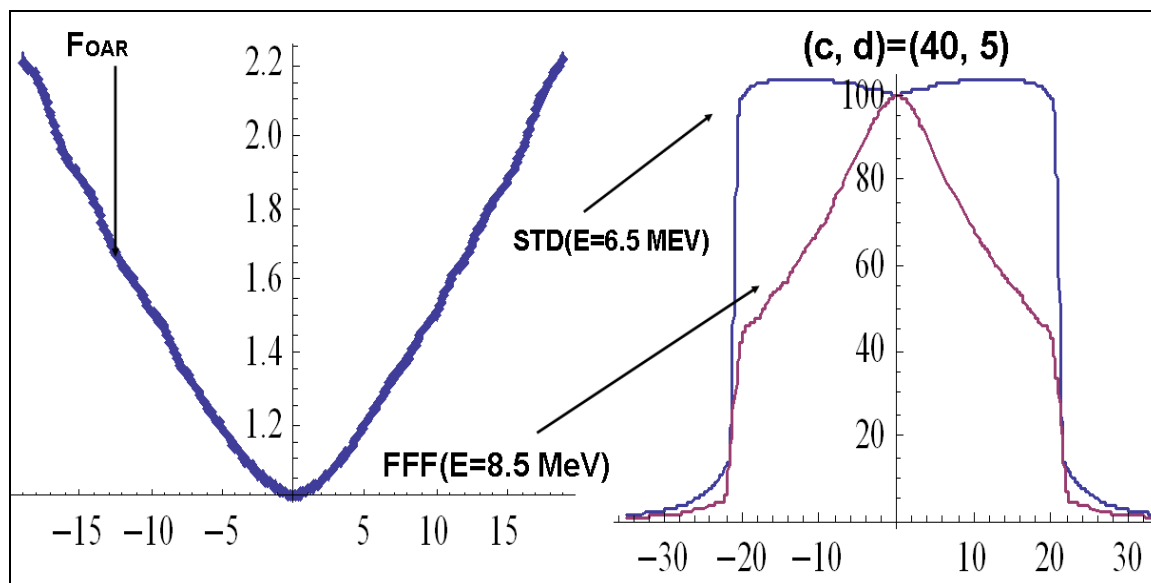


**Figure 18:** Example of the dose ratio between FFF and STD linac for a 40x40 cm field and for depth of 5 cm in water.

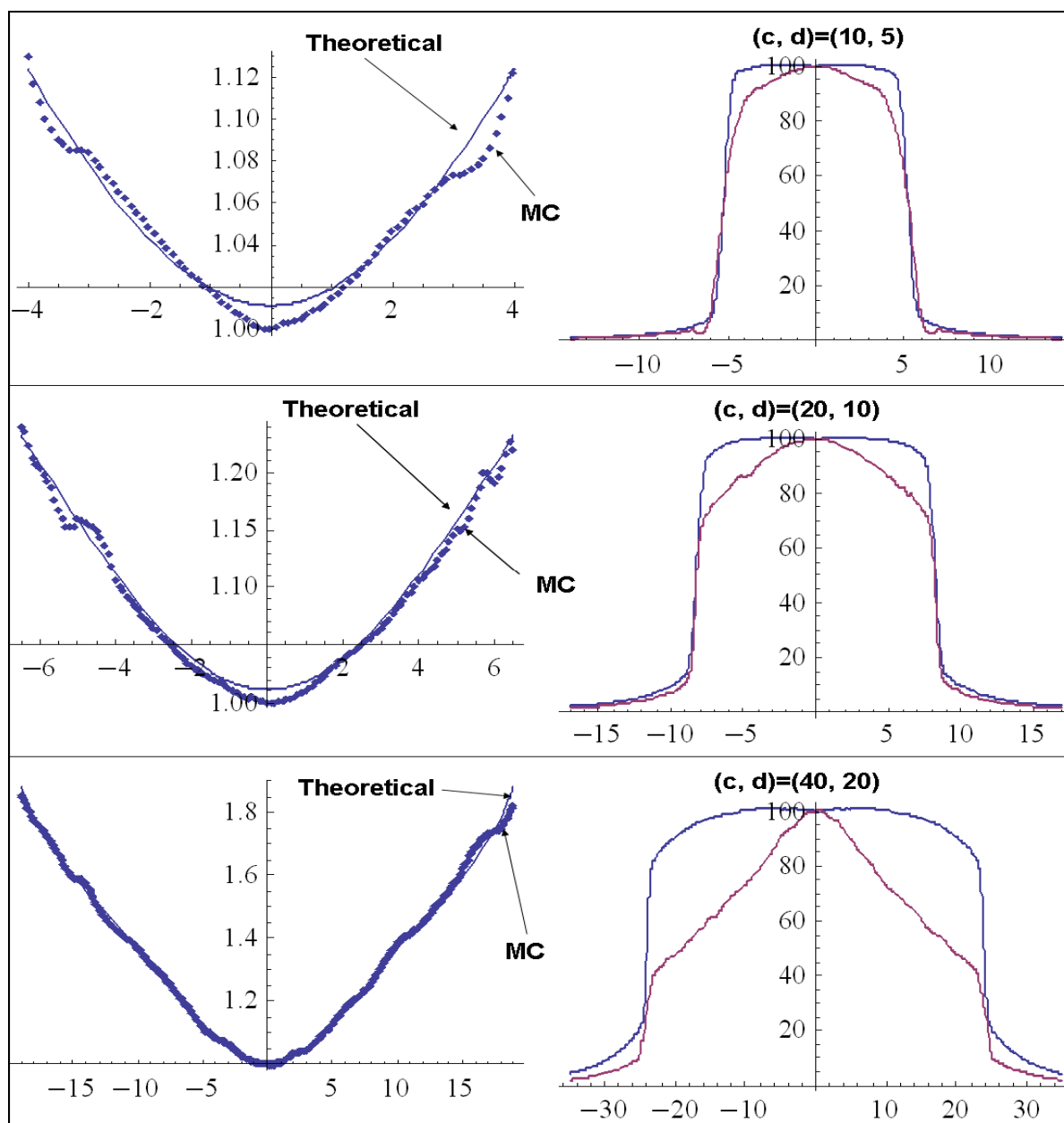


**Figure 19:** Comparison between theoretical formula  $F_{OAR}$  and calculated ratio of STD and FFF linac for different depths  $d$  and field sizes  $c$ . Field of 10x10 cm<sup>2</sup>, depth of 5 cm (upper), field of 20x20 cm<sup>2</sup>, depth of 10 cm (middle), field of 40x40 cm<sup>2</sup>, depth of 20 cm (lower).

### III.3. Treatment planning study with the mFFF linac

#### III.3.A Treatment planning commissioning for FFF/ mFFF linac

Modified data (PDD, OAR, Scatter factor tables, diagonal profiles) were imported in Eclipse treatment planning (E-TPR). A comparison of dose profiles for the mFFF linac calculated from Eclipse for a water phantom versus MC simulations for the same geometry. Aim of this study is to check that data manipulation from Eclipse was reproducing the same results as MC simulation. **Figure 20** summarizes these tests for different field sizes and for depth of 10 cm.



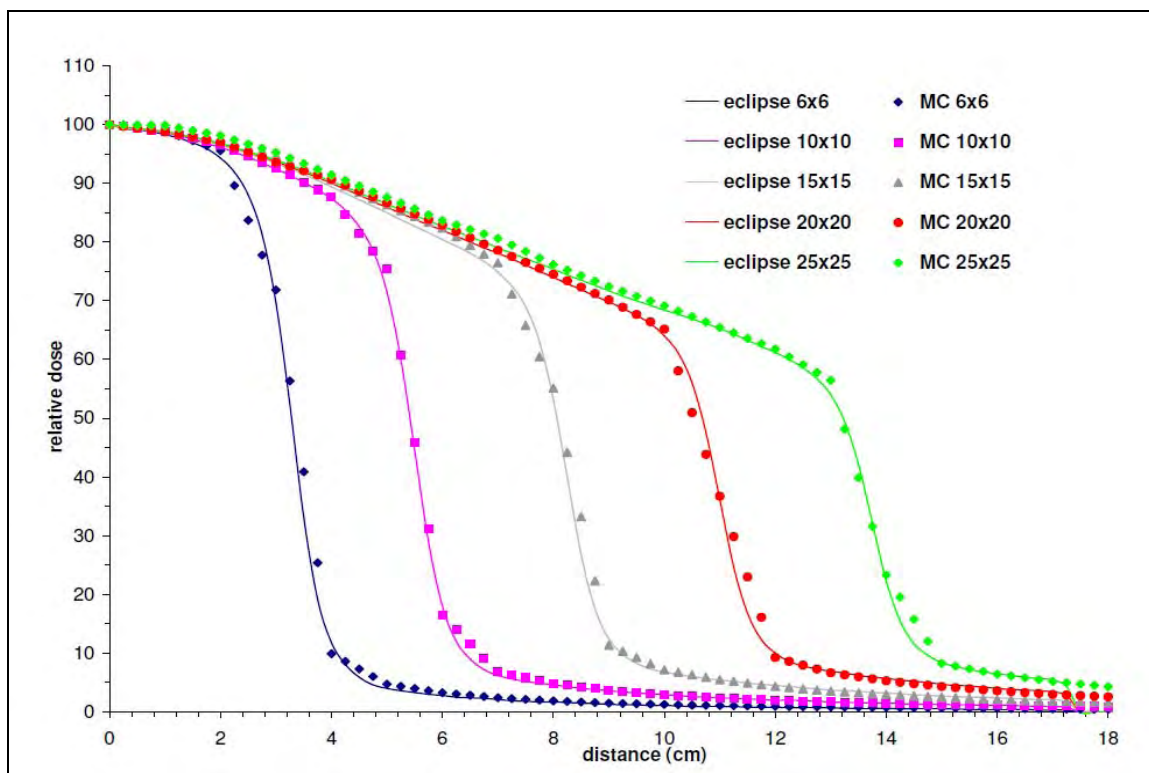


**Figure 20:** Eclipse versus MC simulation profiles at depth of 10 cm in water phantom and for various treatment fields.

The next step was to test the mFFF linac for IMRT optimization plans. For that reason simple cylindrical geometries were created and 5, equal distributed fields, with couch at zero were created. Four different cylinders were used with 5 and 10 cm radius and with 10 and 30 cm height (figure 20). For the same dose coverage average MU increased:

10 cm cylinder: 105 MU  $\rightarrow$  134 MU ( $\sim 28\%$ )

30 cm cylinder: 104 MU  $\rightarrow$  193 MU ( $\sim 85\%$ ), So the effective dose rate was decreased.

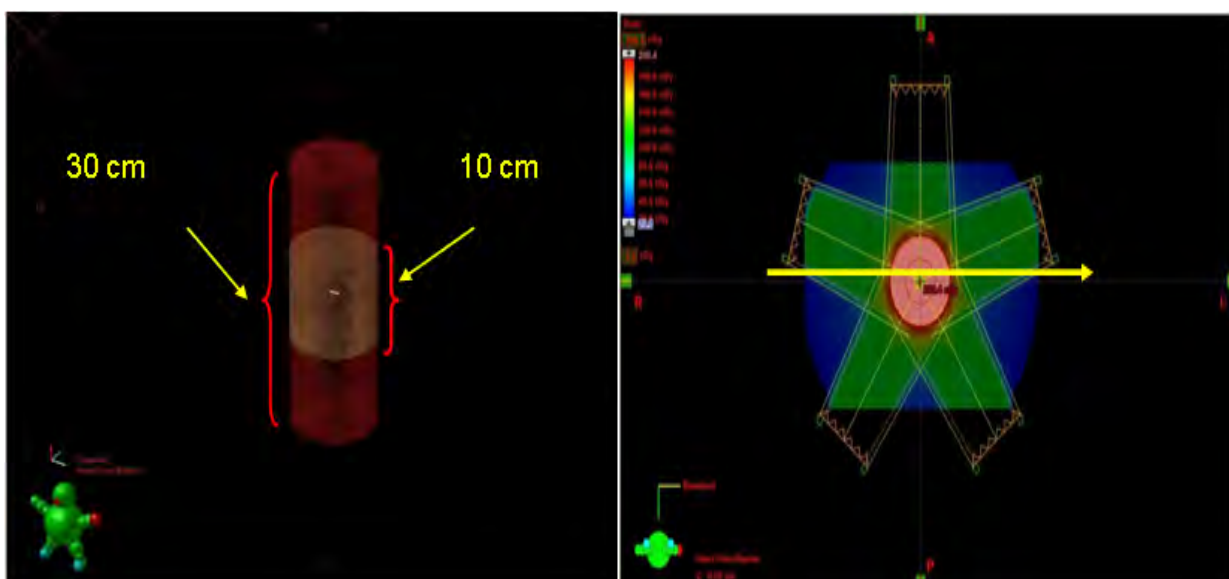


**Figure 21:** 3-D representation of the cylinder used for testing without the fields (left) and with the fields using a different view (right).

### III.3.B Modification function

As it was described in an earlier section of the current dissertation the above cylindrical geometries were used to extract the correction function between the mFFF linac and the STD one. For that purpose dose profiles from open beam fields, dynamic sweeping gaps and IMRT plans were extracted and a dose ratio between STD dose and mFFF dose was obtained. The reason that this was done in Eclipse was that smoother data can be obtained. A graphical representation of the above can be summarized in the following figure (figure 22).

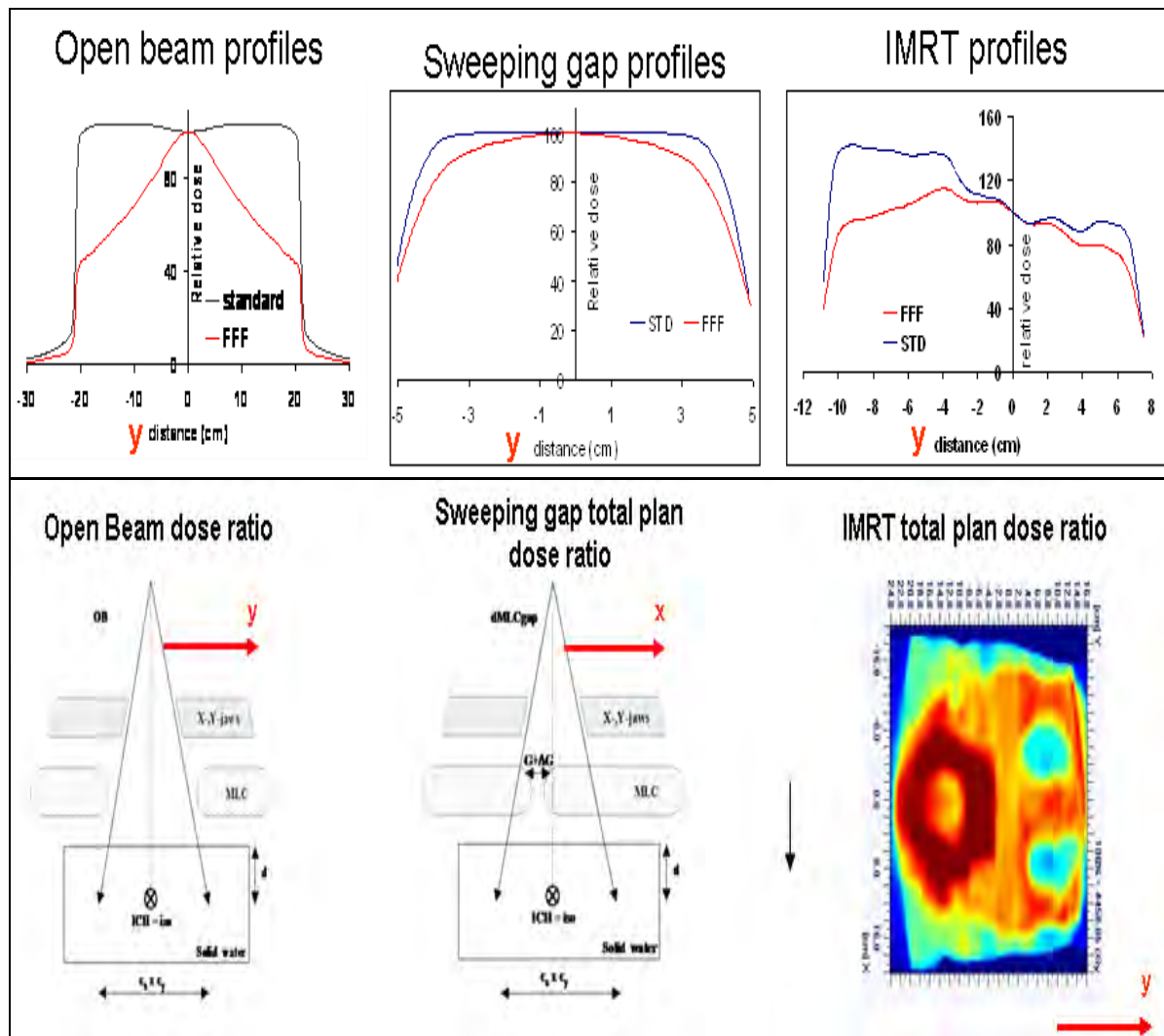


**Figure 22:** Dose ratios for different delivery patterns.

At this point it has to be mentioned that the aim of this part of project A2 is to identify any simple approached that can shed light on how to compensate low dose rate at off-axis points. For trying to give an answer to this problem a Fluence (F)-correction method was introduce. Fluence of each IMRT field is corrected according to STD-to-FFF dose ratio:

- 1] Scatter effects are assumed to be secondary compared to primary dose effects
- 2] Open, sweeping gap and IMRT fields and IMRT plans are studied

3] PTV receives the same dose level in FFF and STD IMRT

4] Same MU for FFF

5] Modified FFF fluence:  $F(x,y) \times \Phi(x,y) \approx \Phi(\text{STD})$ , where  $(x,y)$  = BEV coordinates

The resulting F-function for y axis had the form:

$$F(u,v) = 1 + 0.022r^{1.43/2} \quad (20)$$

Where  $(u,v)$  are the new spatial coordinates and  $r$  is the radius from the center of the field. For X-axis non-uniformity is less than for Y-axis because the contribution from opposed fields gives more or less uniform dose along beam line (figure 23 – left). Another reason is that more fields lead to more uniformity in axial planes so the F-function is different for X axis (figure 23 - right):

$$F(x) = 1 + (\text{slope} < 0.022)x^{1.43} \quad (21)$$

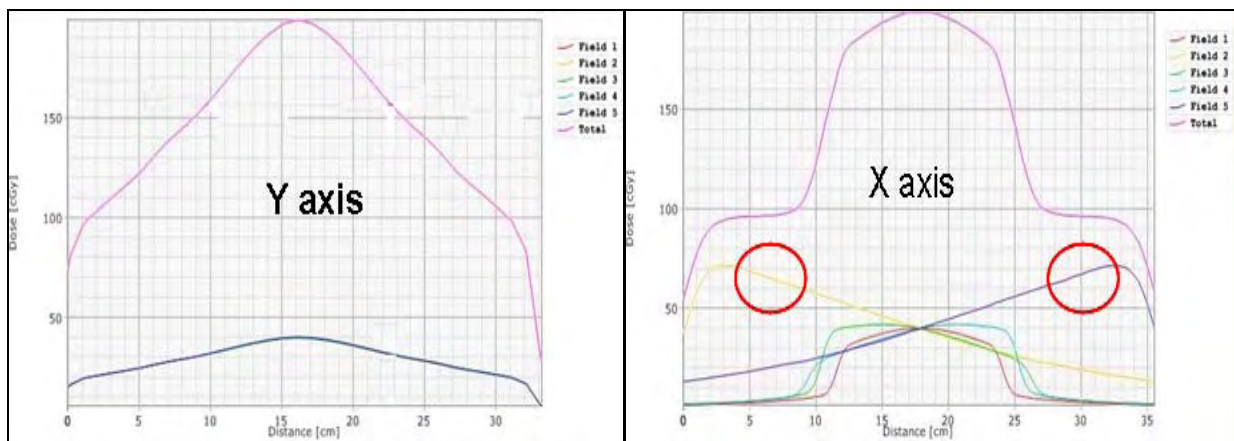


**Figure 23:** Y (left) and X (right) dose profiles of the mFFF linac used to extract the F-function.

### III.3.C Modification function application

The modification function was used to correct the MLC positions of different patient plans which were already treated. MLC positions were recalculated by opening the MLC according to the F-function and without re-optimize the plan for the mFFF linac. MU gap center was kept the same as for the STD linac while the MU gap size was increased according to the F-function as. A pelvis patient plan and a prostate case were tested. Three different MLC correction cases can be distinguished.

1] For smaller PTVs and points close to the isocenter MLC motion does not change a lot (figure 24 – upper).

2] For points further away MU-gap increases considerable and for MU=0 or MUmax there are some truncation problem (figure 24 – middle).

3] For certain locations leaf speed > max or even infinity. Trajectory is flexing in such a way that we would need to introduce MU in between different control points to allow some leaves to



move at max velocity. Another solution is to introduce time before  $\mu=0$  and after  $\mu=1$  (increase total time or MU) ([figure 24 - lower](#)).

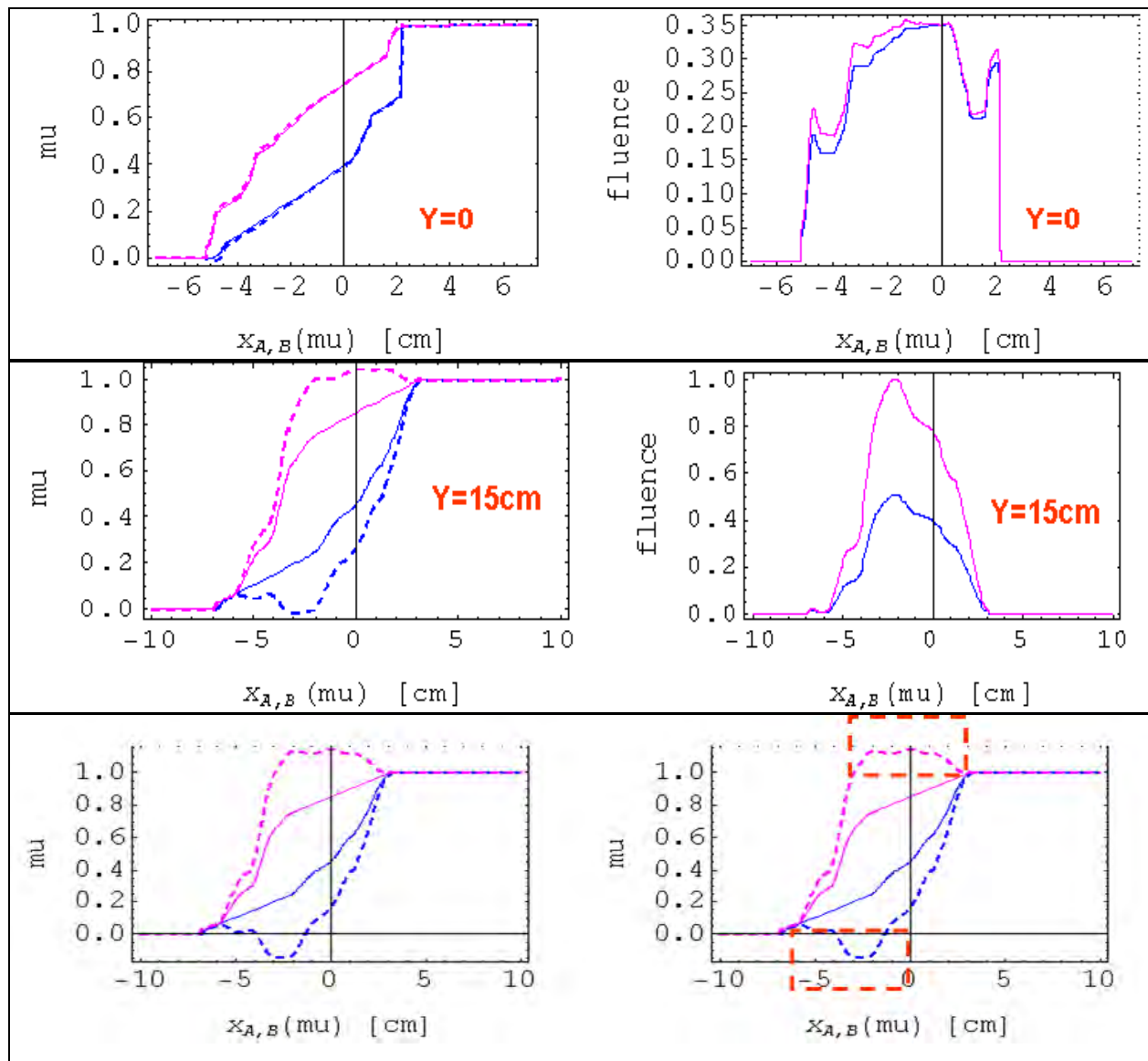


**Figure 24:** Different MLC corrections for different points from the center of the field, at the center (**upper**), for  $y=15$  cm (**middle**) and for points  $>20$  cm (**lower**). Y axis in these plots shows the MU delivered (mu) while x axis represent the spatial distance  $x$  between two opposite leaves A, B.

PTV coverage by using the above method for a prostate case can be shown in [figure 25](#) below, showing the DVH for the mentioned case. In the figure the under dosage area is circled with green (upper figure). While figure on the lower part shows a 3-D representation of the tumor with the underdosed areas highlighted with arrows.



**Figure 25:** DVH comparison between STD plan and mFFF plan for the PTV area (**left plot**). Underdosed areas were identified for the PTV (**right plot**).

## Part B

### III.4. Clinical spectra

#### III.4.A Clinical scenarios for photon spectra

In this section we show spectra for the various irradiation conditions listed in [Table 4](#). We sort the spectra into four categories: inside the field, outside of field, IMRT and heterogeneous media.

##### III.4.A.i. Spectra variations inside the irradiated field

[Figure 26a](#) shows spectral changes with depth for FFF vs STD linac. The main features present for both linac types were the increase of the lower part of the spectrum ( $< 200$  keV) and decrease of the high part of the spectrum ( $> 1$  MeV) with depth. Comparison between FFF and STD linac showed that FFF was softer compare to STD spectrum while for FFF spectrum the intermediate area, between 200 keV and 1 MeV, was almost flat. In terms of absolute numbers the lower part of the spectrum was  $\sim 10\%$  higher for FFF linac (100 keV bin) but the relative increase from the surface of the phantom until depth of 20 cm was  $\sim 120\%$  less than the one of STD linac. That means that the lower part of the spectrum undergoes a larger difference with depth in the case of a STD linac.

Comparison of the spectra for the same depth but for different field sizes at CAX showed softening of the spectrum with increasing field size ([figure 26b](#)). The magnitude of  $\Psi(E)$  increased by up to a factor of 2 as we decreased field size from  $10 \times 10$  cm<sup>2</sup> to  $3 \times 3$  cm<sup>2</sup> ([figure 26b](#)). The peak of the  $\Psi(E)$  spectra appeared at different energies and it had different height for different conditions. Depending on the conditions, in the case of STD the maximum shifted from approximately 1.5 MeV to 2 MeV. Trends were similar for the FFF spectra but here the maximum shifted from approximately 1 MeV to 1.5 MeV. The FFF spectrum was softer, with a shift in the

energy of its peak by (0.5 MeV). Another difference between FFF and STD spectrum was that FFF spectrum was practically the same for field sizes larger than 10x10 cm<sup>2</sup> at the CAX of the field. Regarding energies below 200 keV trends were similar with the ones described for depth dependence.

Beyond the effects of field size and application-related variations in the spectrum, there were a number of features related to the fact that the simulated photon beam incident on the water phantom had scattered components and other artifacts originating in the structural elements in the linac head and in the flattening filter. The most prominent feature was the ubiquitous annihilation peak at  $E = 511$  keV, which was more obvious for shallower depths and smaller field sizes due to less scatter and harder spectrum with more high-energy particles.

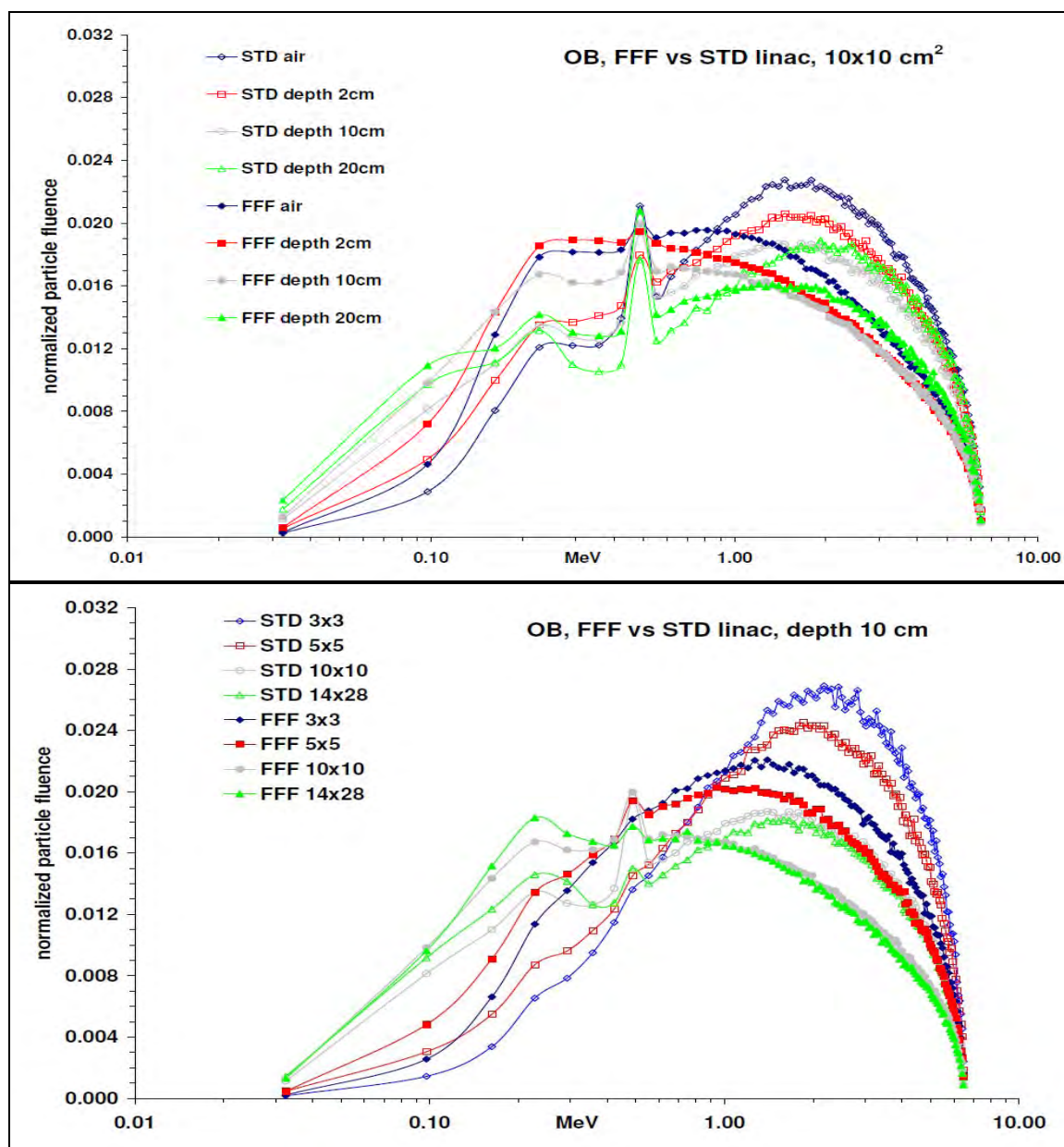


**Figure 26:** Spectral variation comparison of FFF vs STD linac inside the field for different depths (figure 2a - field size = 10x10 cm<sup>2</sup>) and different field sizes (figure 2b - depth = 10cm) for open beam (OB).

### III.4.A.ii. Spectra variations outside the irradiated field

Photon energy spectra were also determined for out-of-field areas and compared to the CAX data (figure 27). Out-of-field spectra changed significantly with distance from the field edge and that change was larger with depth. At out-of-field positions the beam lacks the uncollided primary component, and it had contribution only from head leakage and scatter radiation. As we move away from the CAX the scatter contribution increased and it became the dominant component of the radiation field. Scatter radiation consists of lower energy photons and this was the reason that aforementioned shifting of the spectrum was observed.

Out-of-field spectra of FFF vs STD linac mainly differentiate below 200 keV and above 500 keV. For the lower area FFF spectrum peak value was ~10% higher than STD linac. In the area between 200 keV – 500 keV spectra were practically the same. Above these energies FFF spectrum was progressively lower than STD with relative difference vary from 17% (550 keV) to 75% (1.5 MeV), while at the very high part of the spectrum (>3 MeV) these differences were decreased but still remained above 20%. As mentioned previously, in the case of FFF beam the overall spectrum was softer than the flattened one. Consequently, the FFF beam had a higher component of low-energy particles as we move away from the treatment field.

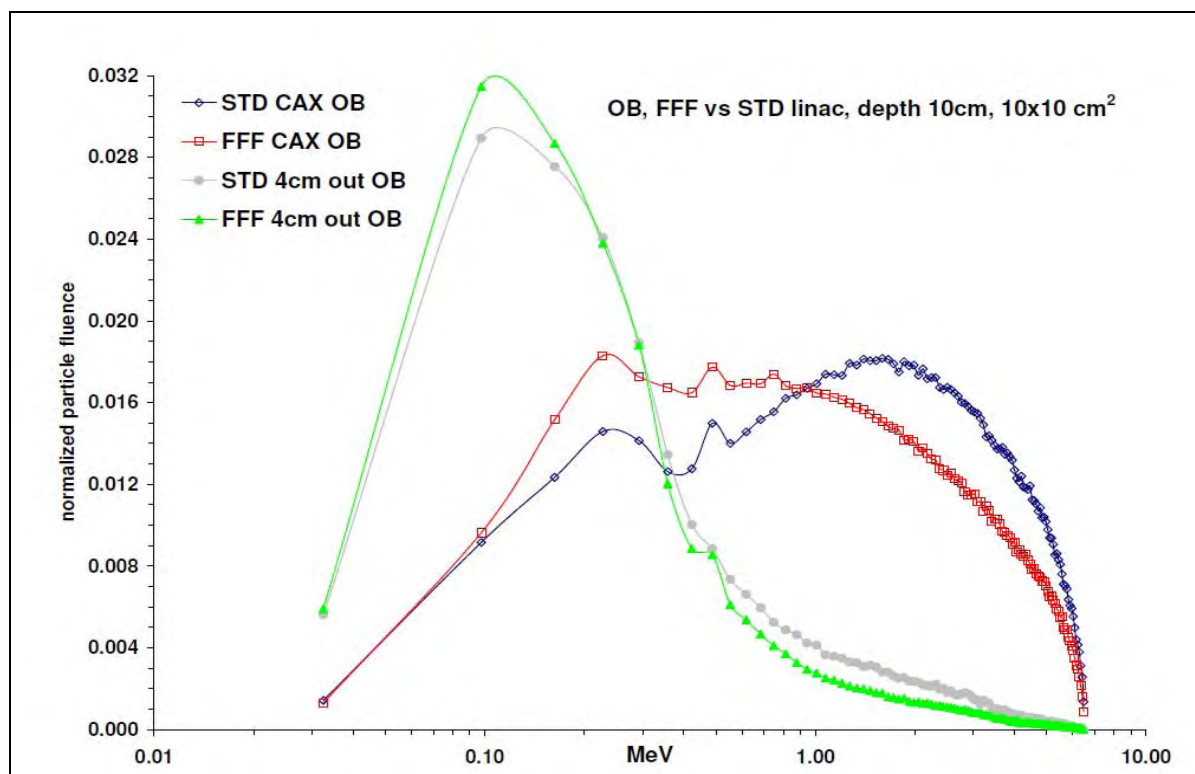


**Figure 27:** Spectra variation in and out of field for open beam (OB) between STD and FFF linac for the case of a 10x10 cm<sup>2</sup> at depth of 10 cm.



### III.4.A.iii.Spectra variations for IMRT fields

A comparison was performed for OB fields versus dynamic IMRT fields (dynamic sweeping gaps - SG). Different widths of SG were simulated in order to investigate the potential effect of MLC-induced hardening and scatter on beam spectra. The overall behavior of IMRT beam spectra was similar to that of open beam (figure 28). For both conditions, OB and SG, there is a shift of the spectra towards lower energies as we move away from the CAX. The comparison between CAX dynamic-IMRT (dIMRT) spectra and OB showed that there was a softening in the case of dIMRT delivery due to the presence of the MLC leaves in the beam. Softening can be noticed in the lower ( $>200$  keV) and higher ( $> 1$  MeV) spectral regions where the spectrum shifts towards lower energies. The opposite effect can be noticed in the case of out-of-field spectra in the low energy region.

Although spectral differences between OB and IMRT are small, it was noticeable that the low energy portion of the spectrum had a higher area under the curve for the OB versus the MLC, owing to the attenuating effect of the latter. Out-of-field IMRT spectral effects between STD and FFF linac were following similar patterns and behavior were practically the same for the lower part of the spectrum with FFF to be  $\sim 5\%$  larger than STD linac. For the high energy part of the spectrum FFF linac had lower than STD by  $\sim 15 - 20\%$ .

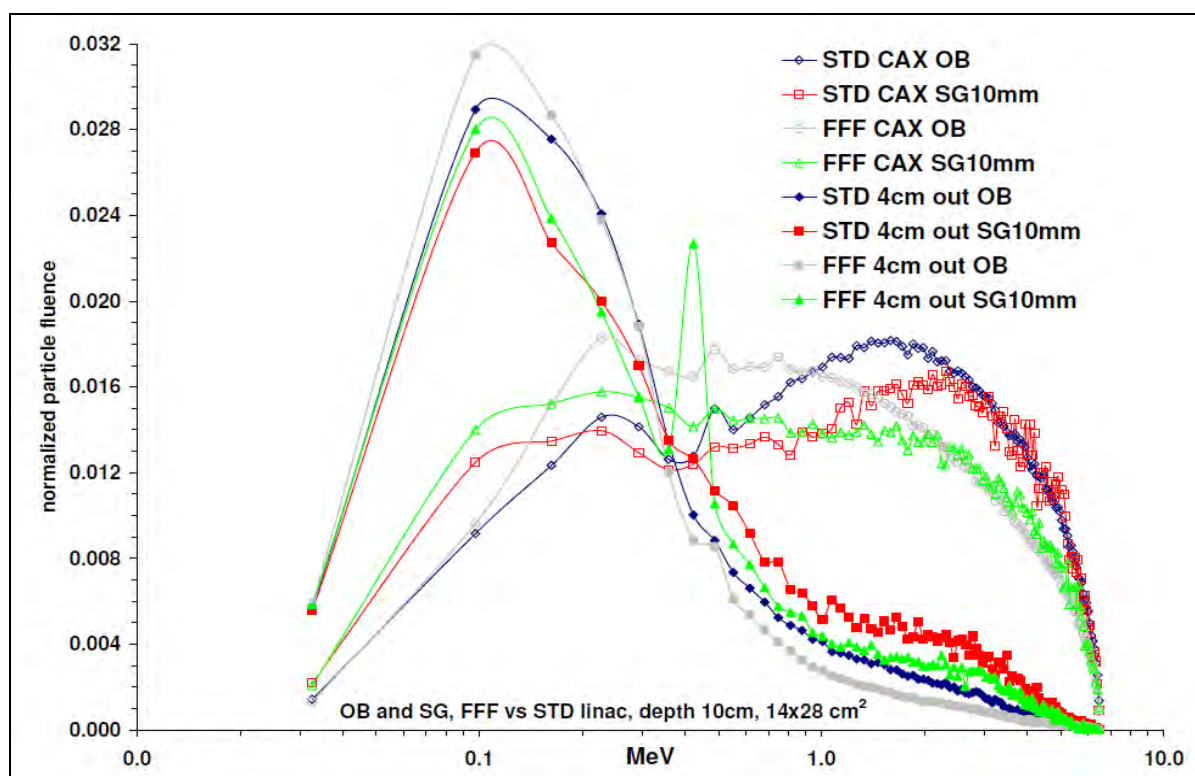


**Figure 28:** Spectra variation in and out of field for open beam (OB) and dIMRT (SW10mm) fields between STD and FFF linac for the case of a 14x28 cm<sup>2</sup> at depth of 10 cm.

Spectral differences for SG larger than 10 mm were considered to be negligible as the opening of the SG was large and the scatter from the MLC surfaces did not significantly change the overall spectra compared to the OB. As the SW size was decreased, the spectrum progressively became harder as the transmitted and attenuated photons through the MLCs became more dominant compare to the contribution of laterally scattered photons inside the phantom. The same effect was also presented for the out-of-field spectra. Despite the shift of the spectra towards lower energies there was a significant increase in the flux for energies larger than 1MeV due to similar effects.

FFF beams were affected to a lesser extent for larger SG compared to the STD case, as there was already a large contribution from phantom scatter and from the lower energy radiation in the primary beam. FFF linac had a lower mean energy and it can be attenuated more as the SG decreases (low energy photons were absorbed more by the MLCs) or as the distance from the CAX increases (larger phantom scatter due to larger number of lower energy particles of the beam). Hence, the hardening of the beam was more pronounced relative to a STD linac.

Finally, comparison was also performed between irradiation involving two split IMRT subfields ( $10 \times 10 \text{ cm}^2$  – SG 10 mm) and a single IMRT without split (figure 6b). The comparison showed that the contribution of the out-of-field dose of the second IMRT sub-field on the CAX of the first one results in an overall softer and flatter spectrum for STD linac but in the case of FFF linac the split IMRT and the IMRT are practically producing the same results as the increase at the lower energy area was o more than 7% while for STD was between 50 and 200% (figure 29).

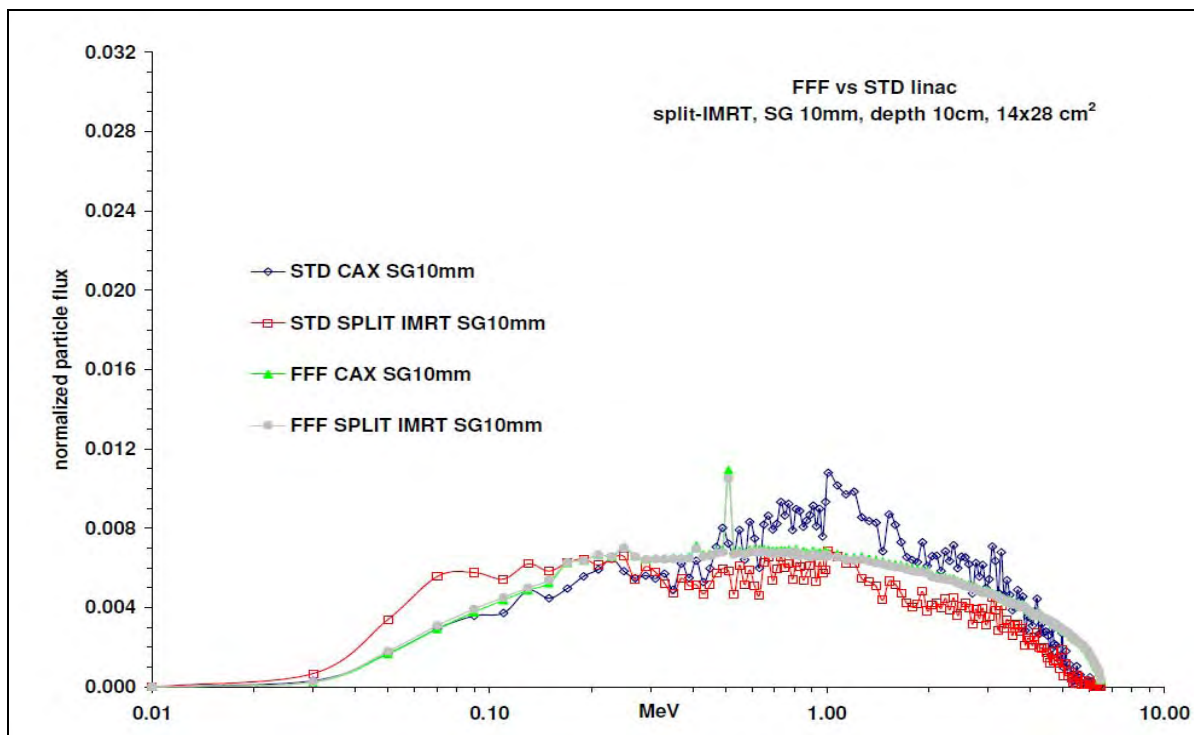


**Figure 29:** Spectra variation in water for STD and FFF IMRT field ( $10 \times 10 \text{ cm}^2$  – SG 10 mm –  $d=10 \text{ cm}$ ) versus split IMRT field for the same field size, depth and sweeping gap size.

#### III.4.A.iv.Spectra variations due to heterogeneities

The impact of heterogeneities (bone and lung) on photon beam quality was studied with and without the flattening filter. Figure 30 shows spectral differences between lung insert (10 cm), bone (5 cm) insert, and water without inserts inside the field for an open STD beam with 10x10 cm<sup>2</sup> field size. As mentioned in the methods section, lung and bone spectra were calculated at 20 cm depth. In order for the heterogeneity conditions to be comparable to water without inserts, water equivalent depth was calculated for lung and bone cases. The spectra were calculated at the depth in water where the percent-depth-dose (PDD) was the same as that in the lung and bone phantom cases. In the case of lung insert that was 14.75 cm and in the case of bone insert it was 21 cm. Comparison of the three cases (lung, bone and water equivalent) shows that when the spectra are normalized to the total area under the curve lung produces a harder spectrum than bone. This may be due to the fact that the photons scatter less and are attenuated to a smaller degree in air (lung) than in bone at the same water equivalent depth. The removal of the flattening filter significantly affects the out-of-field spectrum of the lung heterogeneity. Compared to the STD case, there is a 40% increase in photon fluence in the low energy region due partially to the lack of the filter and the commensurate reduction in PE absorption, and partially to the low density of the lung.

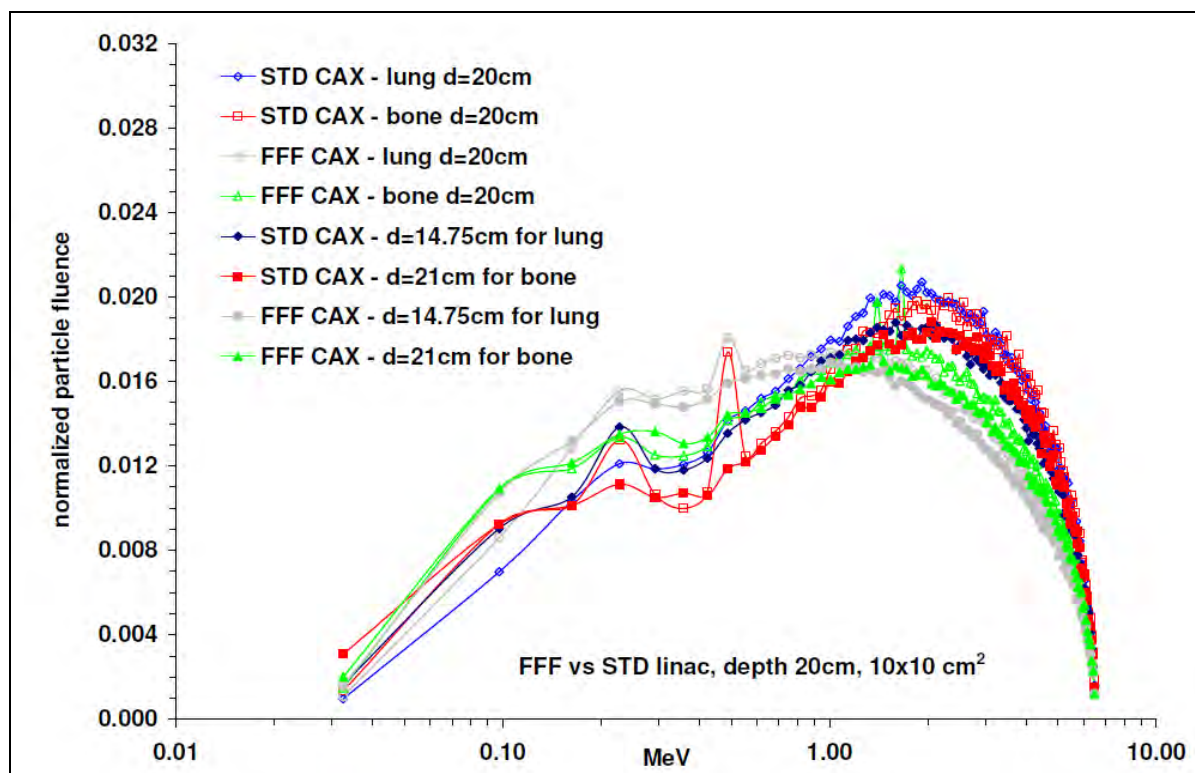


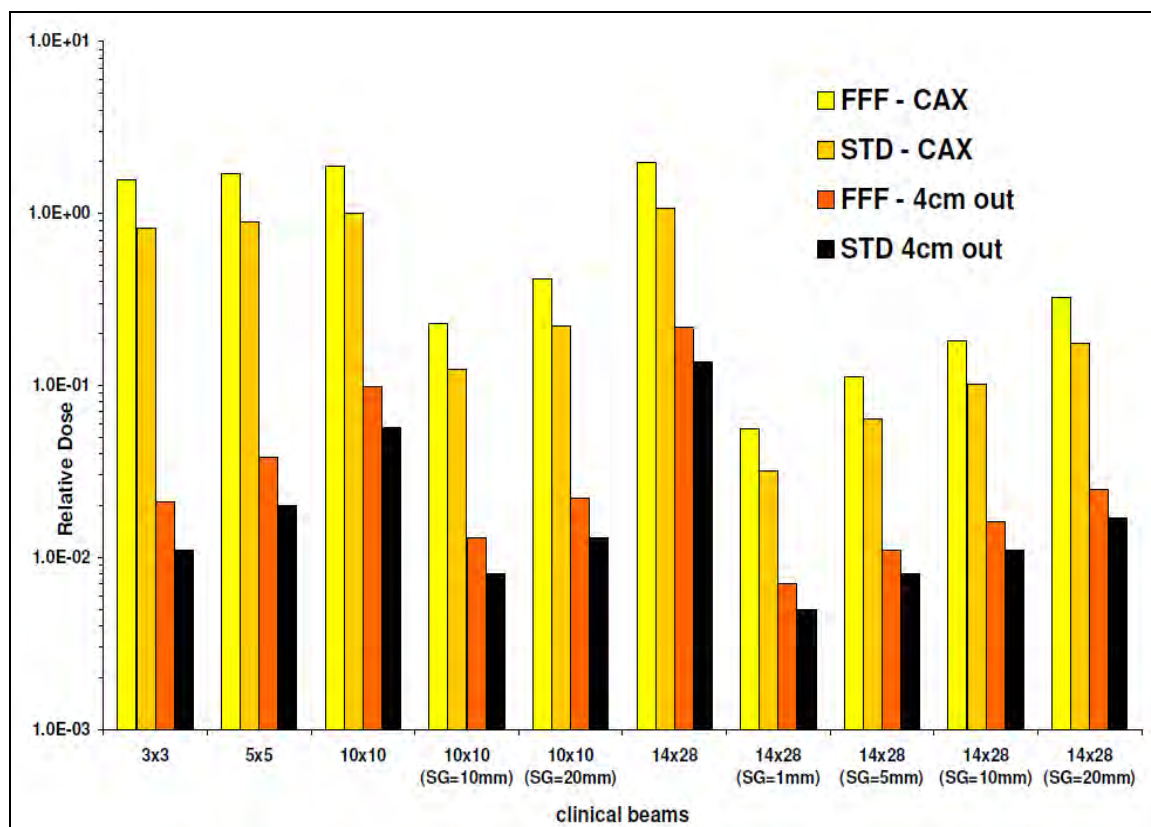
**Figure 30:** Spectra variation for STD and FFF (10x10 cm<sup>2</sup> – OB - d=20 cm) in homogenous phantom and phantom with 10 cm lung or 5 cm bone for the same conditions.

### III.4.B Spectrum-weighted dose metrics

In this section, doses arising from the various spectra are analyzed. The impacts of the differential effects seen in the beam quality are also explored.

#### III.4.B.i.Dose variations

In clinical practice the most important physical parameter is the dose. Doses were computed at the same spatial locations as the spectra. Figure 31a and 31b shows a bar chart in semi logarithmic scale of the doses in all simulated cases, computed at the central axis and at 4cm out of field, and normalized to the dose value of a 10x10 cm<sup>2</sup> open STD beam field at depth of 10 cm in water. The calculated percentage uncertainty by EGSnrc was not larger than 1.3% for the case of STD linac for 4 cm out of field. The dose for FFF linac is larger by a factor of 2 as there is an increased dose rate after removing the flattening filter for the same beam current incident on the linac target. The dose inside the field, as expected, is approximately one order of magnitude larger than out-of-field for both linac types. However, spectral comparison shows that there is a large increase in the low-energy segment of the particle spectrum as we move away from the CAX.





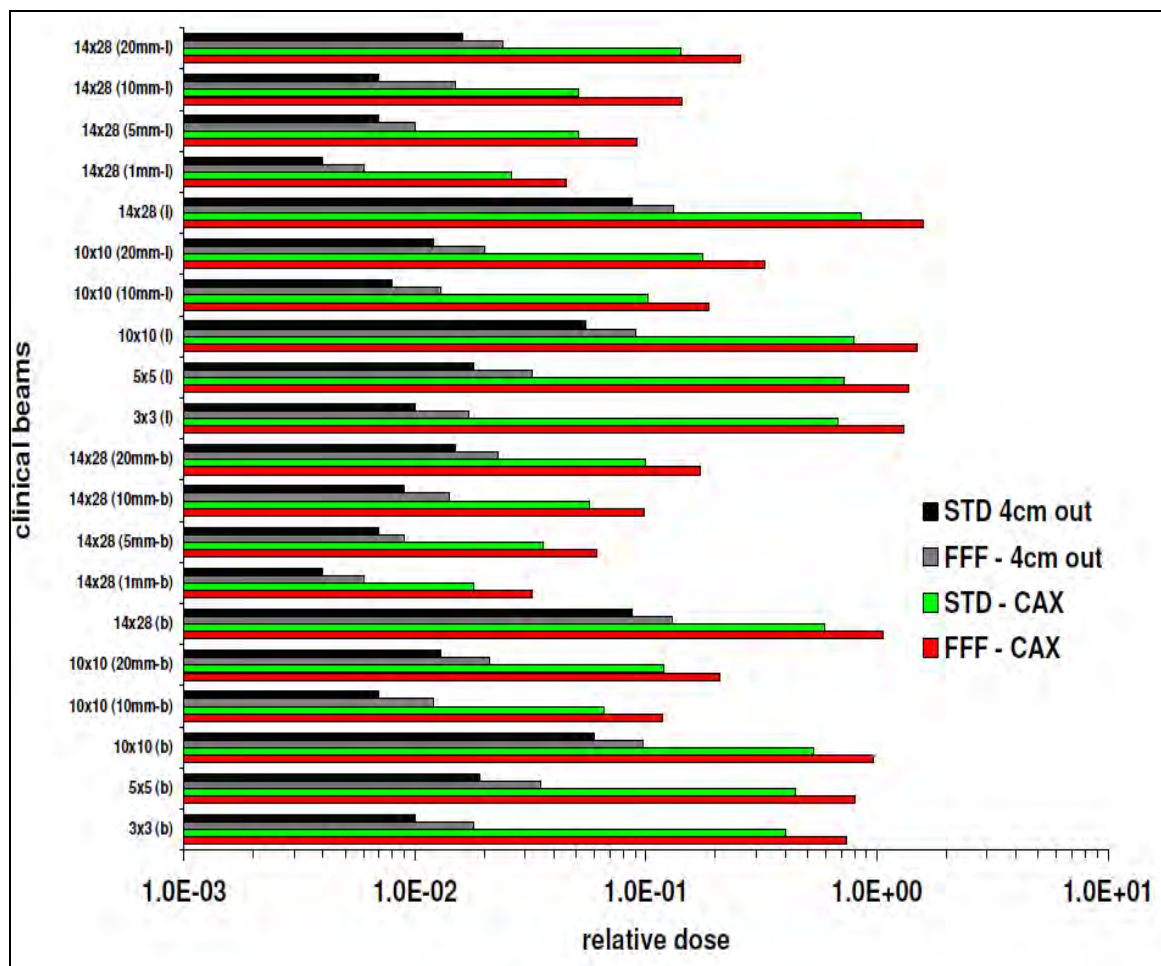


**Figure 31: a)** Bar chart of dose for all the simulated cases at depth of 10cm and for FFF and STD linac. Each bar group contains 4 bars (2 for STD and FFF linac and 2 for CAX and 4cm out of field area). All the doses are normalized to the dose at depth  $d=10$  cm of a  $10 \times 10$  cm<sup>2</sup> STD linac. Symbol (b) stands for bone, (l) for lung [figure 31b] while values in mm are the size of the dynamic sweeping gap for each field size. Groups without brackets are representing open beam.

#### III.4.B.ii. The impact of beam quality on the dose

As it was mentioned the spectrum depends on the beam conditions, which impacts the dose deposition. Presence of heterogeneities may have a further significant impact on the dose. Other than normal anatomic features, such heterogeneities may include surgically inserted metals (e.g., a thin plate) or a film dosimeter in the water phantom. In an attempt to evaluate the impact of the spectrum on the dose with or without heterogeneities, two dose metrics,  $m(E)$  and  $M$ , defined in methods and material section. In considering  $m(E)$  and  $M$ , in addition to their absolute values, the important features are their tendencies and the impact of the differential effects between various irradiation conditions or various depths. The effective dose perturbation factor  $M$  increases with the electron density of the material thus it is larger for higher  $Z$  and lower energies. In the case of FFF linac PE absorption dominates because the effective beam energy is lower by about 2 MV compared to the STD linac. Figure 32 shows how the ratio of

$[\mu_{\text{en}}/\rho]_z / [\mu_{\text{en}}/\rho]_w$ , which is related to  $m(E)$  via Eq. 17, of a given material Z to water w changes with energy.

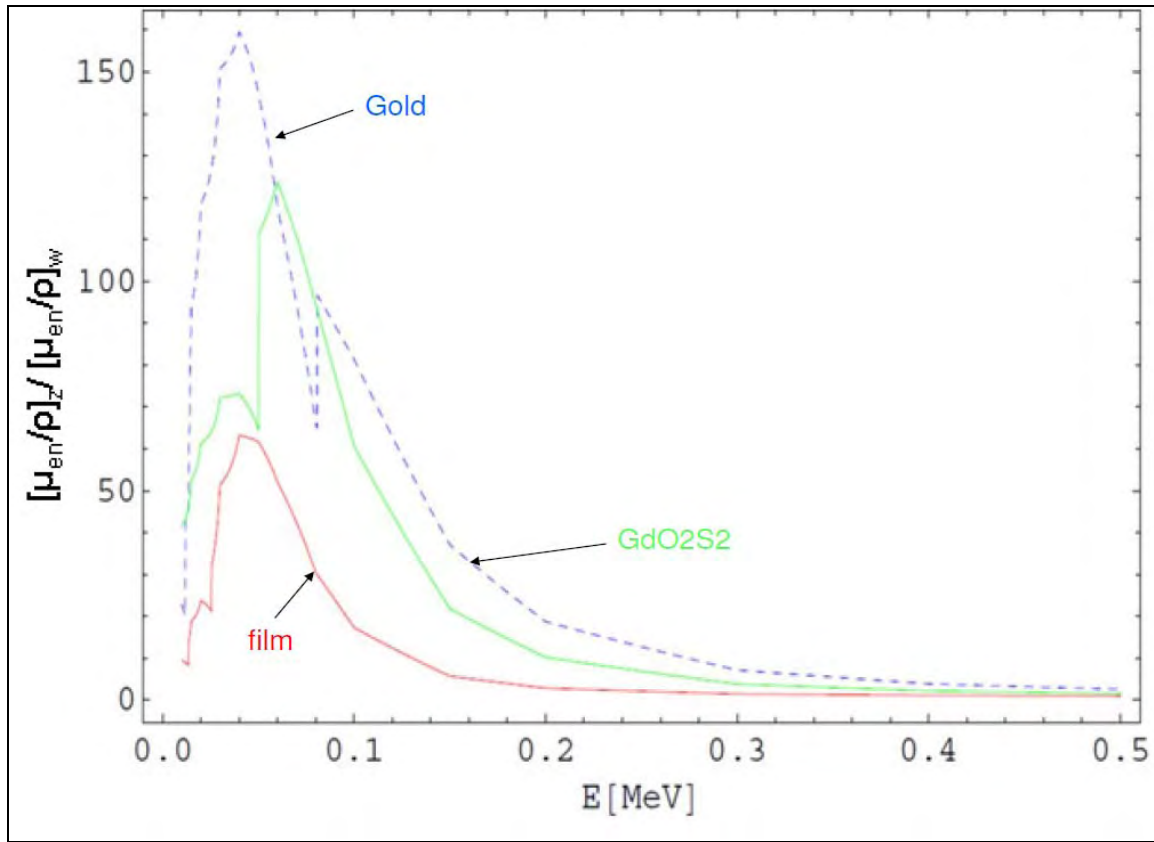


**Figure 32:**  $[\mu_{\text{en}}/\rho]_z / [\mu_{\text{en}}/\rho]_w$  ratio for three different materials: gold, gadolinium oxysulfide ( $\text{GdO}_2\text{S}_2$ ) and film (Kodak AA) for energy range 10 keV – 500 keV.

The effective dose perturbation metric  $M$  increased with depth, field size and  $Z$  of the material while the values for FFF linac were larger compare to STD besides a few cases. A similar trend was observed for IMRT versus OB spectra. Figures 33a and 33b shows  $M$  values for all studied cases and for both linac types: FFF (figure 33a) and STD (figure 33b) and for the three mentioned materials gold,  $\text{GdO}_2\text{S}_2$ , film. Maximum values for both linacs were for gold, out of field areas and split IMRT. Differences between both linacs varied with case and material. The smallest differences were found in case of film. FFF linac had in average for all cases 11.3% higher values for  $M$  while for gold was 21.5% and for  $\text{GdO}_2\text{S}_2$  was 25%. The largest differences between the two linacs, in respect of the material, were calculated for out of field  $M$  values where FFF had a higher value of at least 30%.

When the energy dependent metric  $m(E)$  was evaluated for a dosimetric film exposed to STD  $10 \times 10 \text{ cm}^2$  open beam spectra at different depths ( $d = 2, 10$  and  $20 \text{ cm}$ ), it appeared that the metric was mostly sensitive for energies below  $\sim 200 \text{ keV}$ . This can be demonstrated better in Figure 34, which shows calculated values of metric  $M$  with depth for three different spectral ranges: whole

spectrum ( $E_{\min}$ ,  $E_{\max}$ ), and partial integration in the ranges ( $E_{\min}$ , 200 keV) and (200 keV,  $E_{\max}$ ). The spectrum remains practically the same for energies above 200 keV. The calculated difference for the M metric comes from the spectral area below 200 keV.

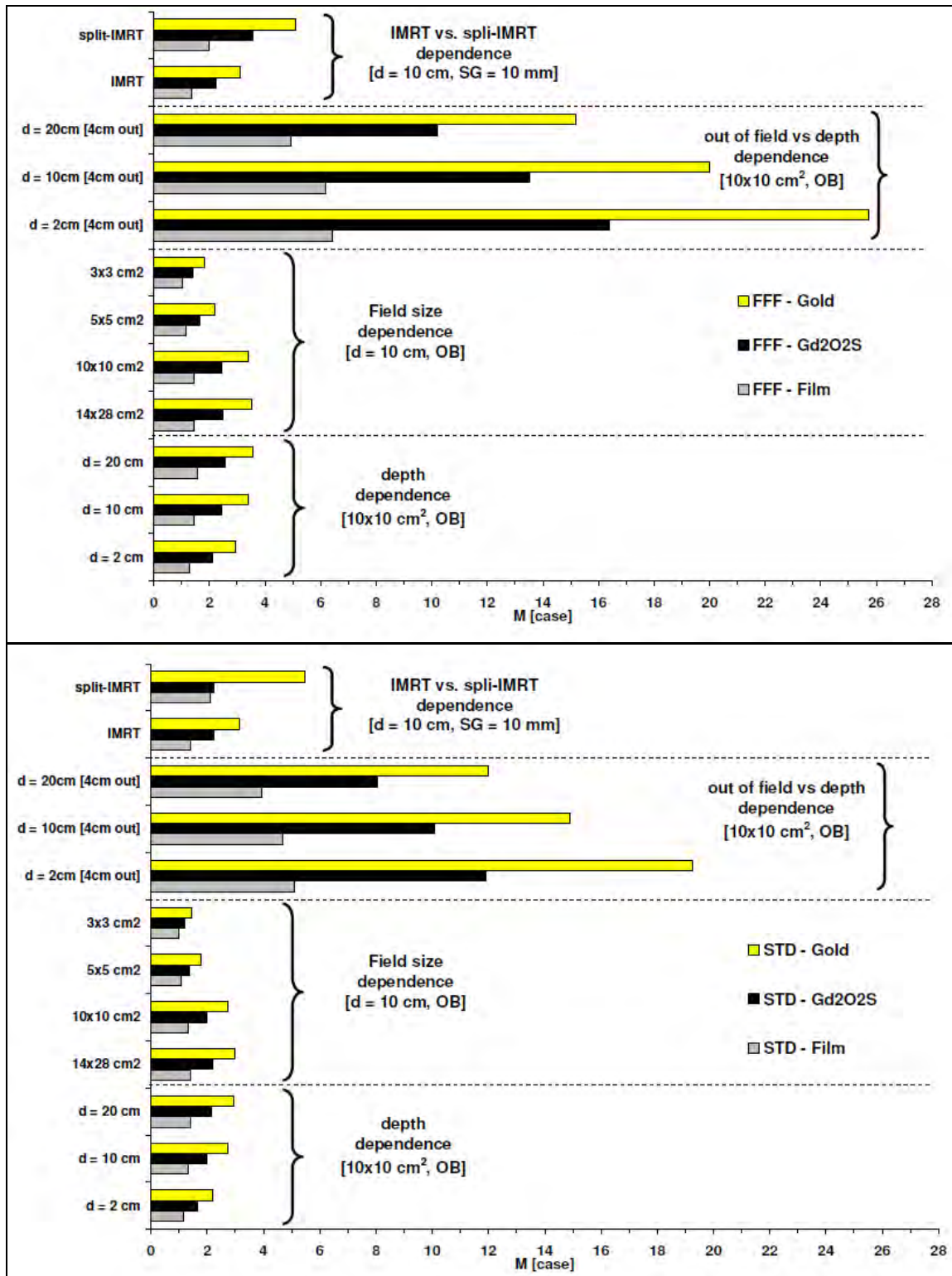


**Figure 33:** M metric for different clinical spectra for FFF (upper figure) and STD (lower figure) linac for the case of gold plate, Kodak film (AA) and gadolinium Oxysulfide ( $GdO_2S_2$ ).

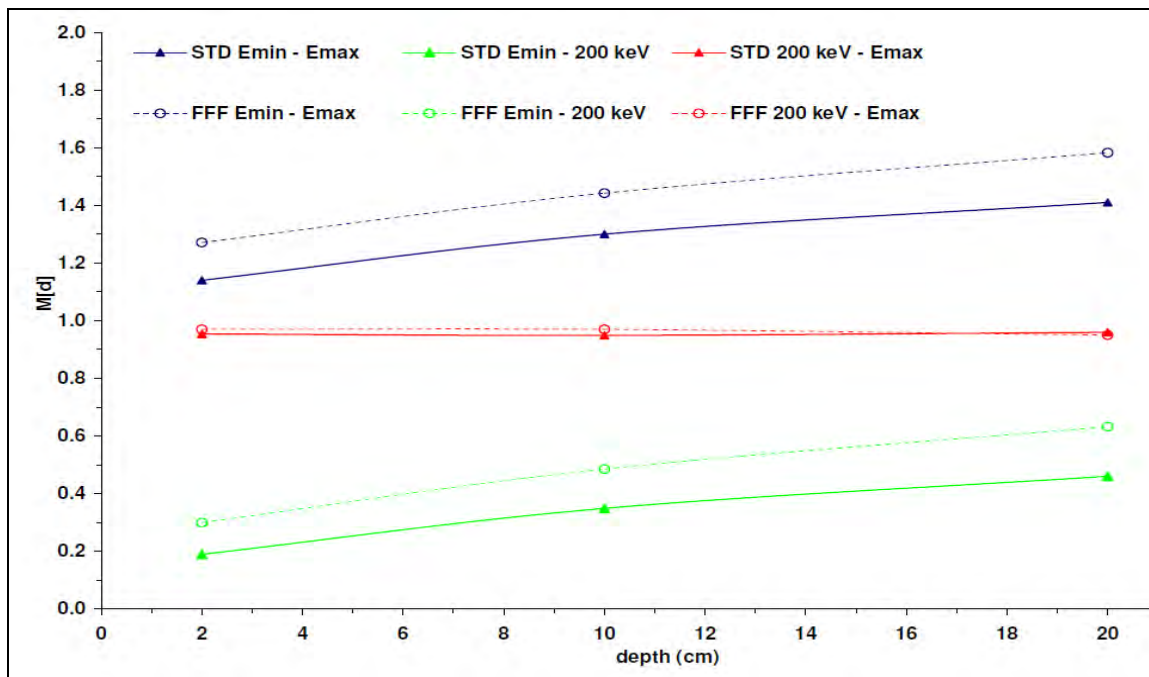


**Figure 34:** Example of how the integral metric  $M$  change as a function of depth for a film (Kodak AA) exposed to a STD open beam  $10 \times 10$  cm<sup>2</sup> and for three energy ranges: whole spectrum (Emin - Emax), 0-200 keV and 200 keV - Emax.

DE effect of different spectral areas and their effect on linacs with and without the flattening filter can be better demonstrated in [Figure 35](#). The figure shows how  $M(x_i)$  changes from the CAX to 4cm out of field for points every 1cm when gold is present (OB,  $14 \times 28$  cm<sup>2</sup>) for a STD versus a FFF linac.

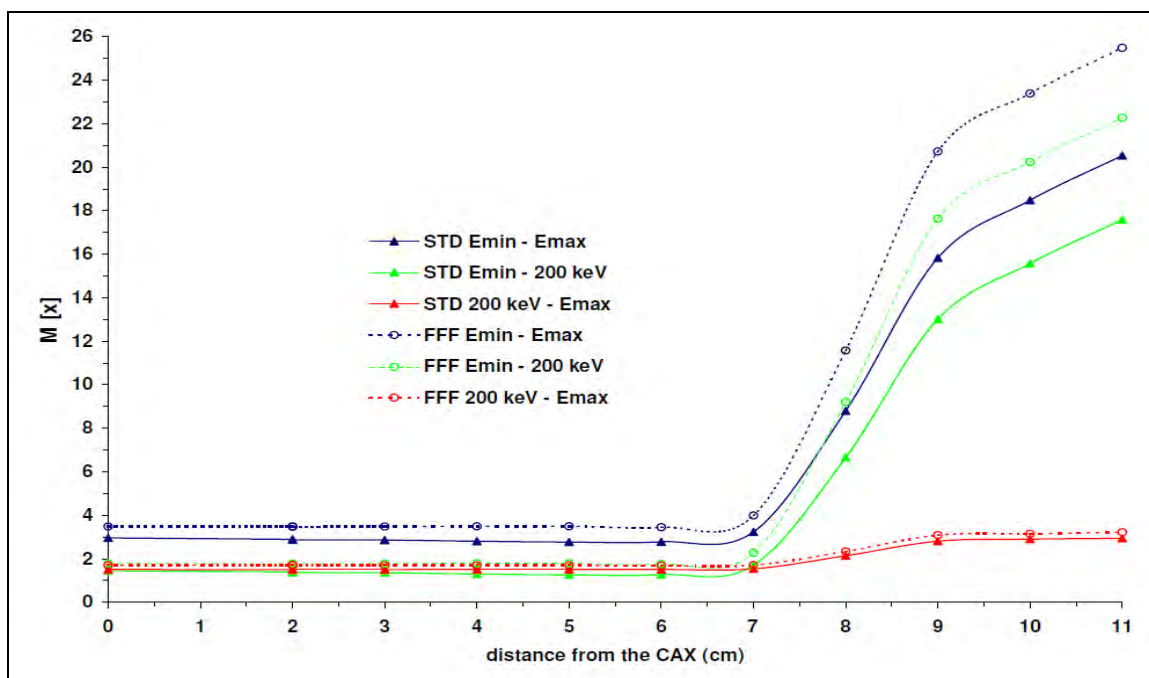


**Figure 35:**  $M[x]$  for gold for the three energy ranges: whole spectrum (0 - Emax), 0-200 keV and 200keV - Emax and for STD versus FFF in the case of an OB,  $14 \times 28$  cm<sup>2</sup> field size at depth of 10cm.

## Part C

### III.5. DER for clinical spectra - optimal beam quality for NPRT

#### III.5.A Monoenergetic beam calculation

Figure 36 shows examples of calculated  $DER(x,E,s)$  values for different monoenergetic (40 keV, 100 keV, 1 MeV) versus a clinical beam (6.5 MV STD linac, CAX, 10x10 cm<sup>2</sup>, depth=10 cm, s=100 nm).  $DER(x)$  simulated with GEANT4 agree with CEPXS. An example of  $DER(x)$  for both codes is presented for 100 keV and for 100 nm GNP's. It is seen that the DER increases with GNP thickness and it decreases as the beam energy increases. DER values for low-energy monoenergetic beams are much larger than for the clinical MV beam. In this particular example, the DER at the surface of the GNP (s=100 nm) for a 40 keV beam is ~20 times larger than that for the clinical beam. However, the clinical beam still shows an appreciably high DER of ~3 near the GNP surface.

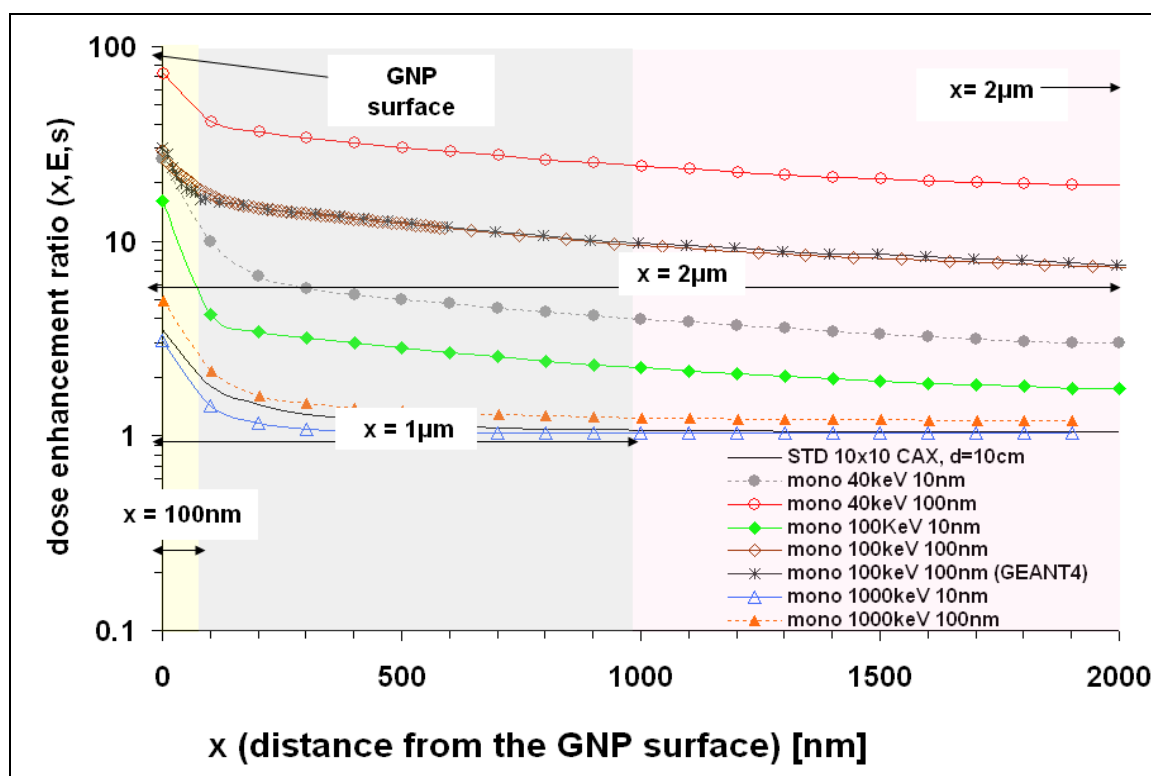


**Figure 36:** DER as function of distance for different monoenergetic beams (40 keV, 100 keV, 1000 keV) and a clinical beam (STD linac, 10x10 cm<sup>2</sup>, CAX, depth=10 cm), for GNP thicknesses s=10 nm and 100 nm. Various potential distances of interest from the GNP surface are marked. An example of DER for CEPXS and GEANT4 codes is shown for 100 keV.



### III.5.B Comparison of different clinical scenarios

DER( $x,E,s$ ) was computed with high spatial resolution (in 2–10 nm steps) within the range extending to 2  $\mu\text{m}$  from the surface of the GNP. DER values were tabulated /summarized for all spectral cases. In this paper data are presented in form of point-wise values and range-averages for several distances only:  $x \rightarrow 0$ ,  $x=100$  nm and  $x=2$   $\mu\text{m}$ . These distances were selected to represent various cellular and molecular ranges of interest, such as the scale of DNA and the nucleosome ( $x < 10$  nm), the phospholipids bilayer of the cell membrane ( $\sim 10$  nm), looped chromatin ( $< 100$  nm), endothelial cell nucleus ( $\sim 1$   $\mu\text{m}$ ), and the average size of endothelial cells ( $\sim 2$   $\mu\text{m}$ ).

Figure 37 shows DER values for selected cases and for 100 nm/ 10 nm GNP thickness. It is readily seen that out-of-field areas give rise to greater DE than along the beam CAX. In addition, the magnitude of the enhancement increases with GNP thickness. FFF beams and split-IMRT fields have larger values than STD and OB. The largest DER value ( $\sim 17$ ) was found for FFF-linac at 4 cm out-of-field and for GNP size  $s=100$  nm. The smallest DER ( $\sim 3$ ) applies for STD-linac beamline,  $3 \times 3$   $\text{cm}^2$  field size, CAX, with thickness  $s=10$  nm.

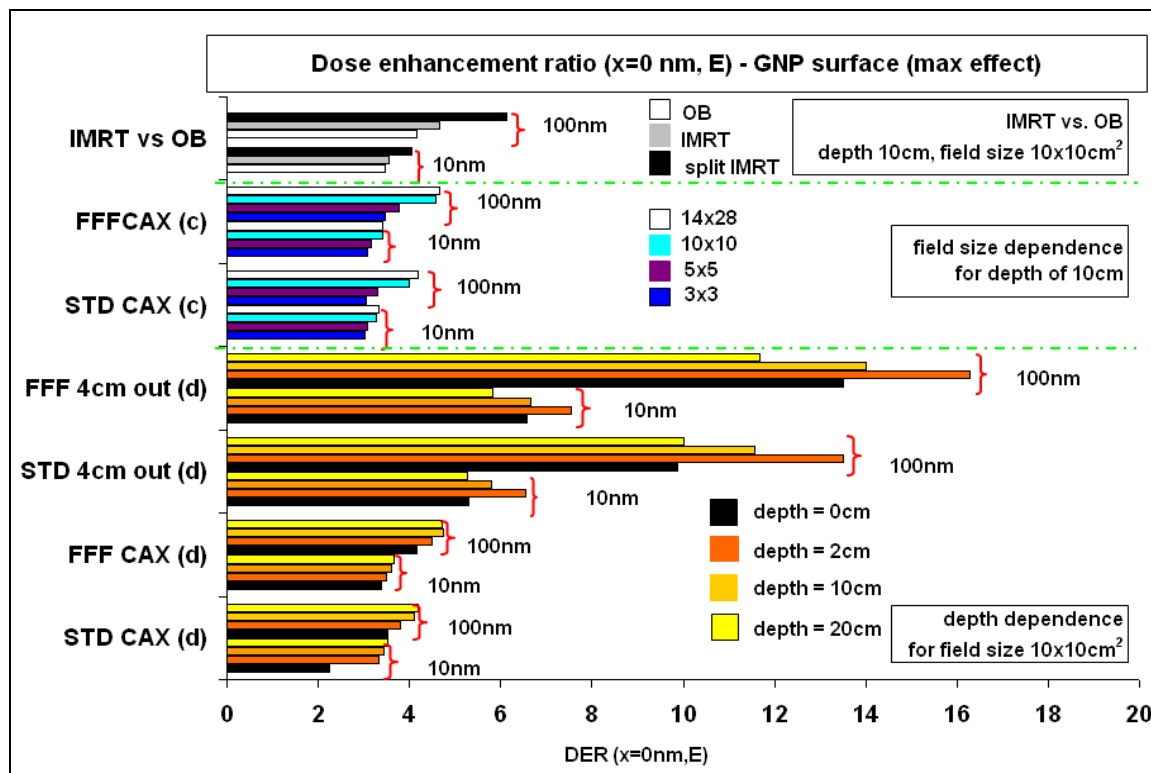


**Figure 37:** Maximum DER( $x \rightarrow 0$ , E) values at the GNP surface ( $x \rightarrow 0$ ) for different clinical scenarios and GNP thicknesses (10 nm, 100 nm).

Figure 38 compares the computed DER values for OB, IMRT and split-IMRT fields (STD,  $10 \times 10$   $\text{cm}^2$ , depth=10 cm) at various spatial ranges corresponding to different cellular targets. In all

examined cases, it is clear that the larger GNP results in larger DE (100 nm compared to 10 nm). The relative increase in DER as function of thickness is more pronounced for the split-IMRT case than for any other case. The least pronounced increase in DER is observed in the OB case. As expected, the largest DER values are computed near the surface of the GNP. The data shows that the DE is highly localized to the near vicinity of the GNP. The spatially averaged DER gradually decreases in all cases as the distance from the GNP increases. A marked change occurs as the range increases from  $[0, 100 \text{ nm}]$  to  $[0, 1 \text{ }\mu\text{m}]$ , while the relative difference between the average DER in  $[0, 1 \text{ }\mu\text{m}]$  versus  $[0, 2 \text{ }\mu\text{m}]$  is significantly smaller. For the 10 nm thickness, the DE shows little difference between OB and IMRT. At 100 nm size the difference is more distinct but it remains small.

In analyzing the various spatial averages, it is also seen that if the GNP resides outside of the cell the most feasible target of the radiation becomes the cell membrane (range 0–100 nm). In this range the average DER for 100 nm clusters is  $\sim 4$  versus over the range of the entire endothelial cell the average DER is less than 2. In this case a treatment using split-IMRT fields has at least a  $\sim 25\%$  higher DER compared to an OB treatment. In the case when the GNP enters the cell and migrates near the nucleus (range 1  $\mu\text{m}$ ) then DER is  $\sim 2.5$  (split-IMRT,  $s=100 \text{ nm}$ ).

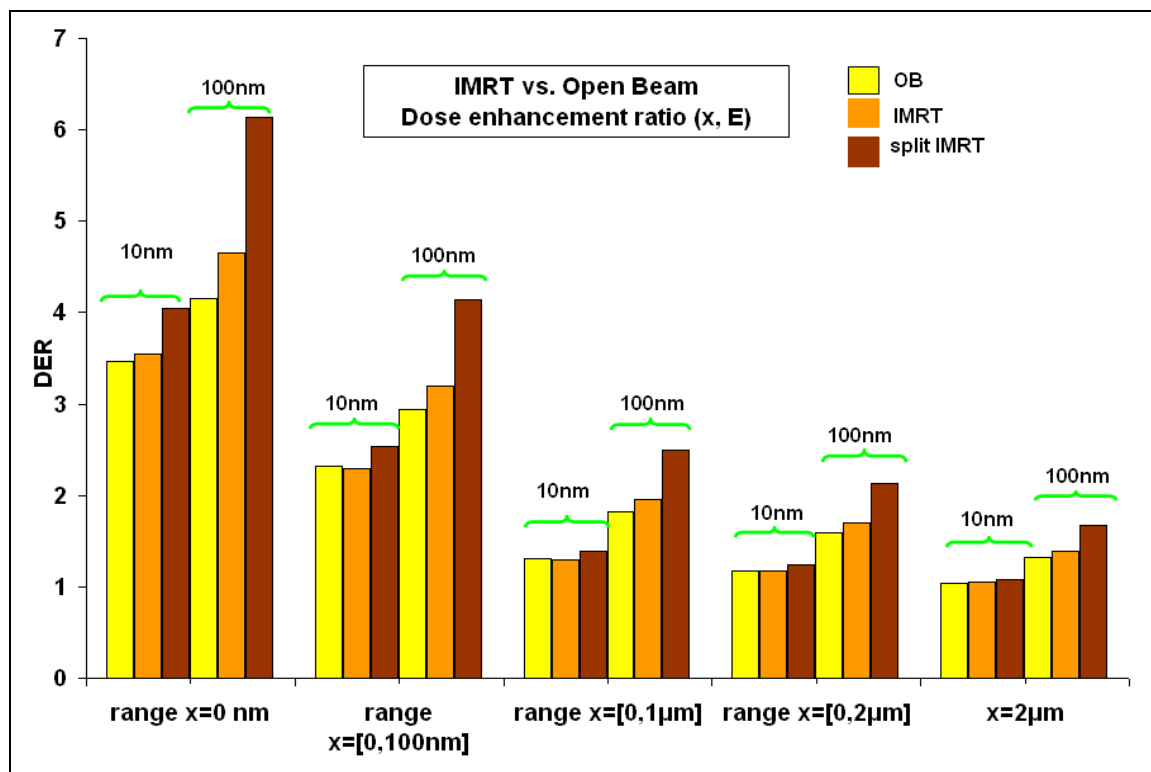


**Figure 38:** Calculated DER values as a function of distance from the surface of a GNP ( $s=10 \text{ nm}$ ,  $100 \text{ nm}$ ) for OB vs. IMRT and split-IMRT (STD-linac,  $10 \times 10 \text{ cm}^2$ , depth= $10 \text{ cm}$ ). Spatially averaged DER values are shown for ranges  $0 < x < 100 \text{ nm}$ ,  $0 < x < 1 \text{ }\mu\text{m}$  and  $0 < x < 2 \text{ }\mu\text{m}$ .

Comparison of DER for different clinical beam scenarios as function of depth shows that there is a very strong dependence with lateral distance from the CAX. DER undergoes a precipitous rise ( $\sim 17$ ) as both the depth and distance from the CAX are increased [Figure 39]. GNP size and FFF beams increases the strength of this effect. Average DER values for range equal to the cell size ( $0-2\ \mu\text{m}$ ) show that the DER for peripheral area is increased up to  $\sim 4$  depending on the case. DER for the cell membrane of a cell inside the irradiated field has a minimum value of  $\sim 2.3$  ( $s=10\ \text{nm}$ ) for the shallower depths (GNP sits outside the cell) while DER for the cell nucleus is decreasing  $\sim 50\%$  for the same case (GNP sits outside the cell nucleus).

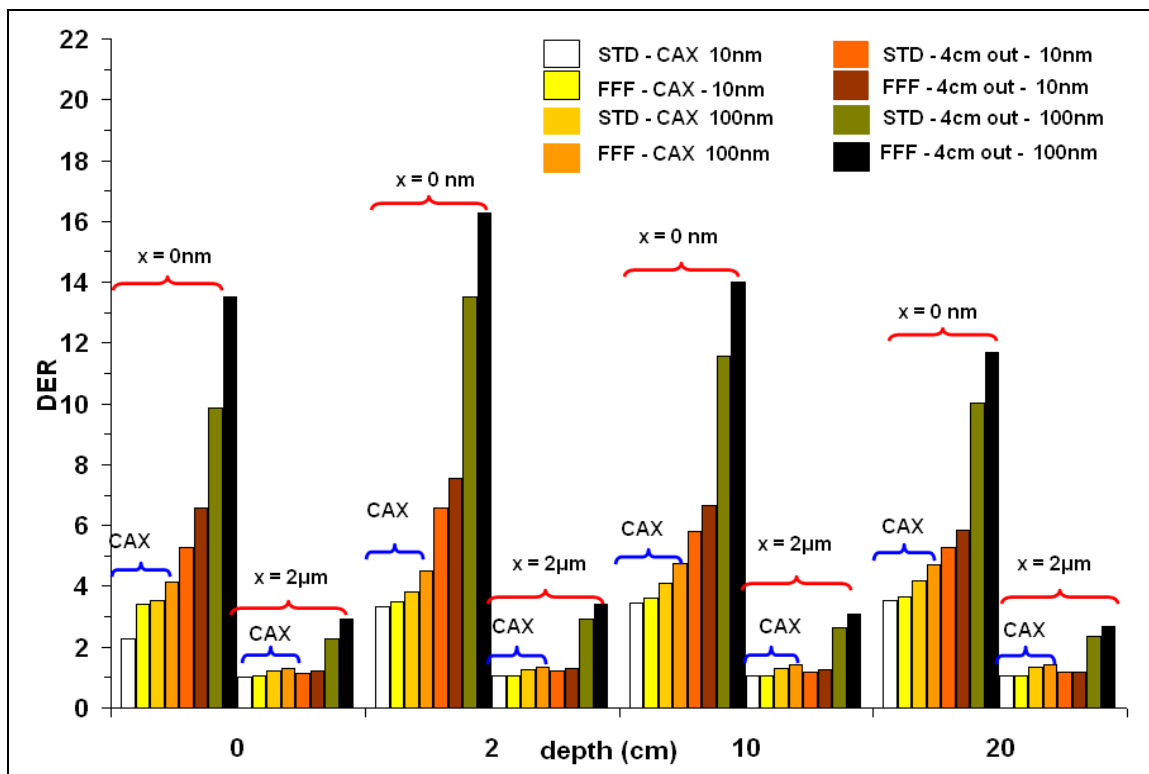


**Figure 39:** Calculated DER values for different depths in water (surface–20 cm) for FFF and STD-linac ( $10\times 10\ \text{cm}^2$ ) along the CAX and at 4 cm out-of-field as function of GNP thickness ( $s=10\ \text{nm}$ ,  $100\ \text{nm}$ ) and distance from its surface at  $x=0$  and at  $x=2\ \mu\text{m}$ .

DER calculation for different field sizes revealed a DE benefit for larger field sizes and for FFF-linac [figure 40]. When an  $s=10\ \text{nm}$  GNP is situated near the cell nucleus, the dose to the nucleus can be increased by 30%. However, for the same case the spatially averaged DER over the range equal to a cell size is  $\sim 1$ . For a thickness  $s=100\ \text{nm}$  the average DER over a  $2\ \mu\text{m}$  range leads to a DE benefit of  $\sim 20\%$ .



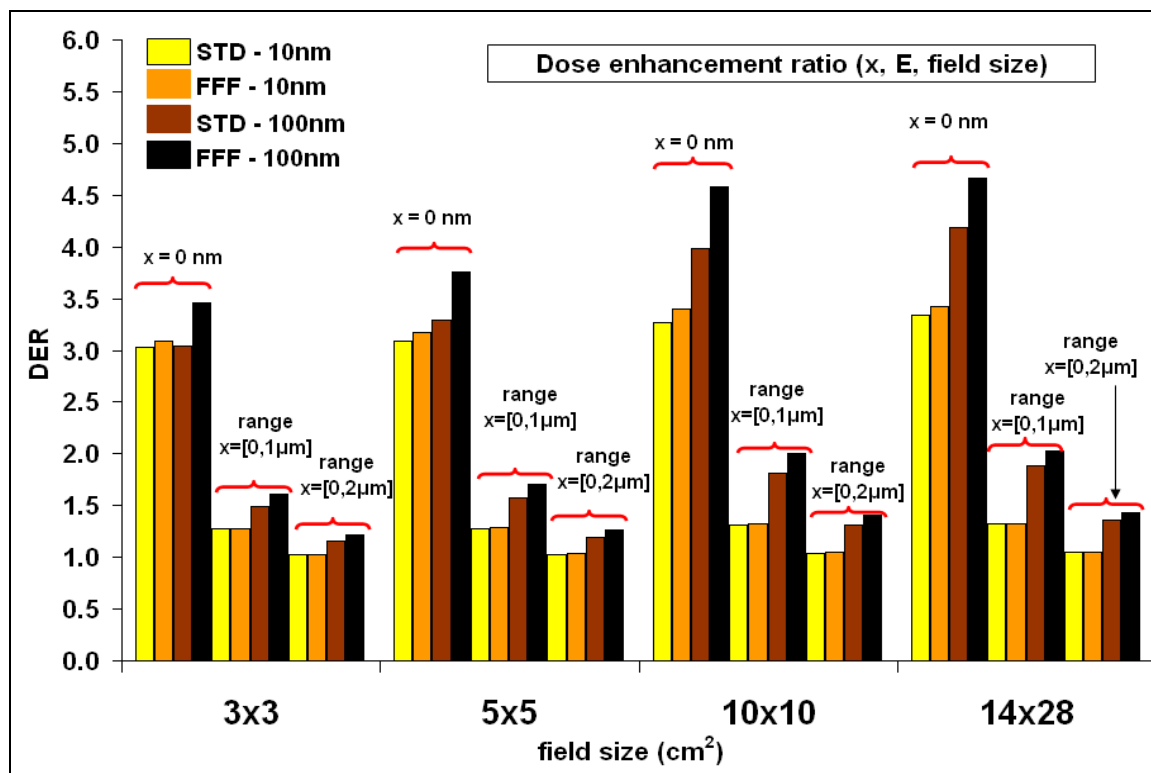


**Figure 40:** DER values for different field sizes (3x3-14x28 cm², depth=10 cm, CAX) as a function of GNP thickness (s=10 nm, 100 nm). Point-wise DER at x=0 and average DER over ranges  $0 < x < 1 \mu\text{m}$  and  $0 < x < 2 \mu\text{m}$  are shown.

## IV. DISCUSSION

### Part A

#### IV.1. Monte Carlo simulation of the medical linac and modification of the head assembly

##### IV.1.A Monte Carlo model validation

MC model for STD linac simulation has been verified. Comparison with measured data showed differences smaller than 2% for the in field area. Comparison of the out-of-field points showed PD difference between MC and measurements below 10% for all field sizes (6x6 - 30x30 cm<sup>2</sup>) until 30 cm from the center of the field. For distances larger than 30 cm differences increased 50% - 250%. This can be attributed to errors in dose measurement, due to the distance from the treatment field, as well as to the large statistical error of MC simulation due to small number of particles deposited in that area. The measured doses in these points and for those fields are extremely small. As a result, a small difference in the measured dose impacts to large % differences between MC and measurements. Furthermore, differences were originated most likely from the inability of the code to simulate accurately the physical back ends of the structures that are included in the linac head, and lack of detailed knowledge about linac structure in those areas.

After the validation of the STD linac the flattening filter was removed from the simulation. In order to verify our MC model for an FFF linac, simulated results were compared with published results and with measurements which took place at the linac, after the removal of the flattening filter. Simulations are in agreement with published parameters [41-60] and measurements for in field properties. Simulated results showed lower dose rate by 8% compared to the measured results. That difference might originate from the effect of secondary structures, which were excluded from the initial simulation with the flattening filter. Those structures might increase the mean energy of the beam, and therefore decrease the fluence of lower energy particles affecting the beam.

Peripheral dose comparison between the measurements and MC modeling of FFF linac was conducted for a similar set up as the one mentioned previously. Percentage differences between them were less than 12% for all points until 30 cm from the center. Most of those points have a percentage difference around 5% (59% of the points). That difference after 30cm increased to 180% to 250%. We consider that the reason is similar with the one mentioned in the case of the STD linac.

Smaller field sizes (1x1 cm<sup>2</sup>), with MLC forming a 1.2x1.2 cm<sup>2</sup> field, showed that our MC model can simulate accurately these fields for both linacs models (FFF and STD). Percentage differences

between MC and the measurements, for distances 15cm from the center of the field, showed differences of about 2% for STD linac (until 5 cm from the edges of the field) and up to 70% for distances of 5 cm – 20 cm from the center of the field. For the FFF linac, the differences between the measurements and MC were 2% - 5% until 20 cm from the center of the field. Percentage differences for STD were large but the measured values were extremely small (the residual dose after attenuation by collimating jaws and MLC) and small changes had a big impact. Moreover, the uncertainty of the code was around 15% in this area, due to the lack of particles because of the size of the field, and the distance of these points from the central axis. MC simulation of FFF is more accurate than STD as the results presented an uncertainty of 5% in the same region. Another possible cause of these differences was the inability of the code to simulate the physical back end of the head structures. Because of that MC could not calculate the increase in dose at around 22 cm from the central axis. That increase was probably due to the physical end of the leaves or of the other head structures. EGSnrc models jaws and MLCs as an extended slab, so dose changes could not be accurately calculated in that region, as shown by previous studies using different codes [48, 60].

In order to match the transmission, different tungsten alloy and interleaf air gap were tested based on published data [48, 148, 153, 163-165], information from Varian's blueprints and experimental data. The chosen values of density and interleaf air gap were  $d=17.5 \text{ gr/cm}^3$  and air gap = 0.0065 cm. Difference between MC and experimental transmission was less than 1%, while statistical uncertainty calculated by MC was less than 1.4% for the voxel of measurement (central axis voxel, depth of 5 cm and SSD =95 cm).

#### **IV.1.B Model of MLC**

Sweeping gap tests of different field sizes and gap sizes showed that simulation of dynamic IMRT with the used MC model presents differences compared to measured data. For the STD linac dosimetric gap calculated by MC seemed to be smaller by 0.034 mm for 14x28 cm<sup>2</sup> field. That difference increased moving to smaller fields (0.058 mm for 10x10 cm<sup>2</sup> field). Despite having matched the transmission through MLC, a more accurate model of the leaves seemed to be needed. In any case, measured and MC doses used for calculation of dosimetric gap were small and very sensitive to several potential effects observed.

Removal of the flattening filter decreased MLC transmission by 13%. Change in transmission between the FFF and the STD linac was expected, because the removing of the flattening filter softens the overall beam spectrum [45]. As a result, the beam was less penetrating and the transmission through the MLC was reduced. Modifying the energy of the FFF linac resulted in beam hardening as well, meaning that the effective energy was increased, so that the MLC transmission could be increased and closer to its original value. Thus, by modifying the linac's

energy we did not match only the PDD, but also the MLC transmission properties, which is useful for comparing IMRT beams using FFF and STD linacs.

#### **IV.1.C Modification of the FFF linac**

Several simulations were performed in order to match the PDD between flattened and unflattened beam for different field sizes. The modified energy was 8.0 MeV for small and medium field sizes and 8.5 MeV for larger field sizes. Furthermore, an attempt was made to match the attenuation properties of as many fields as possible with as few modified energies as possible. Modifying the energy, lead to an increase of dose rate ratio between flattened and unflattened beam, changing that ratio from 1.91 to 3.54 (for 10x10 cm<sup>2</sup>). Increasing the energy may lead to photoneutron production in those materials of the linac head for which the threshold energy is below 8.0 - 8.5 MeV. The sources of photoneutron in linac are mostly the tungsten collimators. For tungsten the threshold energy is around 7.2 MeV for its two main isotopes [<sup>184</sup>W, <sup>186</sup>W]. Cross section for the range of energy we used was still ~50% less than for 10 MV. Cross section changes dramatically after 11 MV, as it increases by a factor of ~3.5 for 12 MV compared to 10 MV. In that sense, neutron content of 8 - 8.5 MV beam was not an issue. However, further optimization of linac design, in order to obtain the best beam quality and spatial distribution, is recommended as described below.

In order to decrease the gradient of the unflattened profiles, changes of  $e^-$  beam spatial spread were made along with changes of electron beam mean angular spread. Profiles of the FFF linac proved to be not sensitive in changes of ( $\sigma_x$ ,  $\sigma_y$ ) values. The flatness of the FFF profiles was sensitive to the mean angular spread changes. Even for values from 5° to 10° (depending on the field size) profiles flatness were acceptable, while keeping a benefit of dose rate by ~2. Angular spread values close or over 14° should not be used as the effective field size is reduced. For field sizes smaller than 6x6 cm<sup>2</sup>, which are more relevant to SBRT, no increase of the mean angular spread is necessary as the beam is flat enough [62]. Therefore, for smaller field sizes the dose rate benefit can be increased even by a factor of ~3.5. This is very important for SBRT as it cannot only lead to a faster treatment, but it can increase the number of patients that can be treated per day. Moreover, it can decrease the possibility of intrafractional motion, as well as to increase patient's comfort (typically many beams with large number of MU values are used in such cases).

In order to characterize dose rate at the central axis and in the PD region for the mFFF linac and the STD linac,  $R_{\text{dose ratio}}$  and  $R_{\text{PD}}$  ratios were calculated. For the calculation of the  $R_{\text{PD}}$  two different methods were used for data normalization. For the first one, peripheral dose ratio was calculated in such a way that maximum dose was delivered in the center of the field. This normalization

method showed how larger the peripheral dose would be for the mFFF linac compared to STD for the same irradiation time. The Modified FFF linac's peripheral dose seemed to be larger by a factor of 1.5 even for the larger  $\sigma_0$  values. The reason for that is the fact that fluence of mFFF linac is much larger, so the delivered dose for the same irradiation time will be much higher compared to STD linac. However, since for a given treatment the target would be irradiated with the same dose for both mFFF and STD linacs, characterization of peripheral dose is best when  $R_{PD}$  ratio [Equation 8] is used. Figure 16b shows this second way of peripheral dose characterization. According to that, all the data were normalized in such a way that the same dose is delivered at the center of the field, for both FFF and STD linac. The graphs showing this normalization method [figures 16b and 17a] showed loss of PD benefit as mean angular spread angle increased for each field size. For small field sizes (6x6 cm<sup>2</sup>) even for 5° spread the lost of PD benefit was ~12%. On the other hand for large fields (>20x20 cm<sup>2</sup>) and for a spread angle of even 10° a benefit of 15% was still kept.

Angularly spreading of the electron beam can be achieved with a passive system, either by modifying the existing permanent magnet design or by designing a new defocusing element.

## Part B

### IV.2. Clinical beam quality and beam perturbation

Uncertainty for spectra calculated at the CAX was below 5% for all the points except for those at the lowest energies (<35 keV) and the highest energies (>6.4 MeV). Uncertainty in these energy ranges was about 30% due to the very small number of particles at the edges of the linac spectrum. For out-of-field spectra, uncertainty was below 5% for  $E < 3$  MeV, and 8% above this energy. Computations at the 511 keV annihilation peak had a much larger uncertainty, ~80% depending on the case considered. The reason was that the energy binning had to be chosen such as to accommodate this narrow peak without altering the results reported for the rest of the spectrum. Consequently, the magnitude of the annihilation peak should be considered only for qualitative assessments. The high uncertainty experienced in the computation of this particular peak did not affect the rest of the spectrum.

Regardless of the differences in the cases studied and the differences showed between FFF and STD linac, there were some general trends in the studied spectra related with the underlined physics. For most of the energies in a 6.5 MV photon beam water is nearly a pure Compton scatterer. Below 30 keV photoelectric (PE) absorption dominates. Although the cross-section for pair production is almost ten-fold lower than that for incoherent scatter even at the highest beam energy, annihilation photons had a pronounced presence in the computed spectra as the 511 keV was obvious in most of the plots. Because of these interactions, the beam quality gradually

changed with depth in the irradiated medium. Below  $\sim 30$  keV, photons were preferentially absorbed via the PE reaction, while higher energy photons underwent Compton scattering. This led to a beam hardening, at the low-energy end of the spectrum, and a simultaneous softening, at the mid-range of the spectrum up to  $\sim 1$  MeV. Since the number of incident photons below 30 keV was relatively small, there was a net effective spectrum softening below 1 MeV. Above this energy, forward scatter became increasingly dominant with little energy loss; therefore the spectrum between 1 MeV and 6.5 MeV was slightly hardened with depth in water. These features can be clearly seen in [figures 26 - 28](#). In addition, there was an increase in the photon fluence between 200 keV and 240 keV, which corresponded to the backscatter peak by photons between 1 MeV and 6.5 MeV of incident energy.

In most cases the studied spectrum changed significantly for different clinical beam scenarios. Analysis of all these cases showed that regardless of the specific irradiation conditions the spectra can be divided into two major categories: in-field and out-of-field. In most cases FFF spectra had similar shape as STD, with an exception of the spectral differences with field size and depth. The maximum of the spectra was larger for STD by as much as 40%, with the larger values taking place for smaller field sizes and larger depths. In general, the relative changes, between different conditions, were smaller for the FFF spectra. However, this was because of the higher component of low energy photons in the FFF linac, which already led to higher dose enhancement than that of the STD linac (photon energies were more “uniformly” distributed for FFF spectra and henceforth their perturbation resulted in lesser relative changes). Due to that, absolute values of the FFF spectrum were higher than the STD's, while the relative changes between different dependencies (e.g. field size or depth) were smaller, with the FFF spectra having a smaller relative change than the STD spectra, which varied from 70 -120 %.

Although it was possible to characterize the spectral differences for the entire energy range of the spectral curves, it was more revealing to divide the energy range into two sub-regions, from the minimum energy  $E_{min}$  - 200 keV and from 200 keV to the maximum energy  $E_{max}$ . The largest changes for different beam conditions were observed in the lower energy range, up until 200 keV. This region seemed to be the most sensitive part of the spectrum. In all the simulated cases (depth and field dependence, IMRT and split IMRT, presence or absence of heterogeneities, distance from the CAX) softening of the spectrum was dominant in this area. Differential effects in spectra for various irradiation conditions were not large for energies above 200 keV and can be neglected. The FFF spectra were changing following a similar pattern, but because their original spectra were softer than those of the STD linac, large differential effects were restricted mostly to the low energy area ( $< 200$  keV). In general, FFF and STD linac spectra can be considered having similar shapes and their integral metric  $M$  varies in a similar way.

Since the photon spectrum changes as a function of beam conditions, it was of interest to find a relation between spectral changes and relevant dosimetric quantities. For instance, if spectral changes were large but the overall dose contribution from the energy range under consideration was not large, then the impact was expected to be small. Therefore, we defined two simple dose perturbation metrics:  $m(E)$  for each energy bin of the spectra, and  $M$ , for the whole spectra. Figure 33a and 33b shows computed  $M$  values for selected clinical scenarios and for three different materials (Gold,  $GdO_2S_2$  and film (Kodak AA)) for FFF and STD linac respectively. Similarly to the analysis of energy fluences for different conditions, attention must be paid to the differential effects in  $m(E)$  or  $M$ , e.g.,  $\{m(E, d) - m(E, d_{ref})\}$  or  $\{M(d) - M(d_{ref})\}$  rather than the magnitudes of  $M$  or  $m(E)$ . Here  $d$  represents the spatial location (depth in phantom) and  $d_{ref}$  is the reference location.

Spectral changes lead to different doses in different materials when heterogeneities were considered. As it can be seen in figure 33a and 33b the dose perturbation metric  $M$  changes considerably for gadolinium oxysulfide and gold and less for film. As the figures showed DE applications would be more efficient when FFF linac was used. The benefit might vary on the irradiation conditions, high  $Z$  material used and case. As demonstrated in figure 34, differential effects were mostly due to spectral changes for energies up to about 200 keV. For greater energies the spectra remained almost the same. This was particularly true for spectral comparison with depth and field size. The larger the field and depth, the more contribution of the differential effects originate in the low energy area. In the case of FFF linac, the overall  $M$  values were higher, but these differences were coming from the low energy area, as in the energy range above 200 keV,  $M$  had practically the same value as in STD beams.

In the case of out-of-field spectra,  $M$  calculation showed that this effect was stronger. Due to the shifting of the spectrum towards lower energies, integral  $M$  values for energies below 200 keV were much higher than in the rest of the spectrum. Differences of  $M$  values between the two spectral areas can reach one order of magnitude, depending on the  $Z$  of the material (higher for higher  $Z$ ). For shallower depths, differences between the FFF and the STD linac were not as pronounced, however as depth increased the FFF beams were differentiated less than the STD. The reason for that was the same as described previously in this section. More low energy particles are the cause of “uniformity” in the phantom scatter, which was the reason for less relative spectral differences from case to case of FFF vs. STD linac.

The case of IMRT for split fields reveals a similar effect. The value of the  $M$  metric was practically the same between OB and IMRT for all spectral areas. However, there was a significant increase for the case of the split IMRT. The contributions of scatter, from the split IMRT field, lead to a spectrum, which was more susceptible to dose perturbation effects for different materials.



Dose data  $D_i$  (figures 31a and 31b) of a certain case and  $M_i$  (figure 33a and 33b) had to be read together for every given spectrum in order to be conclusive. The meaning of dose  $D_i$  is that it is the dose in water of  $i$ -th case ROI. For instance, dose outside of the beam or for deep tumors will be significantly smaller than the dose on the central axis and shallow depths. Thus, for instance, if the contribution of one treatment field to a given ROI is  $D_1$  and is associated with  $M_1$  versus another one ( $D_2, M_2$ ) the total dose in water is  $(D_1 + D_2)$  but the total dose in water containing high-Z material will be  $(M_1 D_1 + M_2 D_2)$ .  $M$  corresponds to the enhancement due to high-Z material resulting from photo absorption. Auger electrons were inherently included in the simulation but because the focus herein is the macroscopic dosimetric quantities, the Auger electrons did not have a big impact on them. Auger electrons should increase the Dose Enhancement Ratio (DER) at the microscopic scale (nm). Thus, our  $m(E)$  is the lower boundary of DER. As mentioned in the introduction section, there were studies showing no clinical significant DER for realistic gold concentrations in case of MV beams [78], as well others showing increase of the DER even by a factor of 8 [31]. The differences in these publications arise from different simulated conditions and normalization schemes used in MC. Clarification of the scale where these effects were calculated as well as normalization of the different quantities used must be done with caution, in order to avoid comparisons between different quantities.

In the current study IMRT fields were studied by using sweeping gaps. A question exists among medical physicists if these techniques can be used for general conclusion regarding IMRT with real patients. Published studies [159 – 161] showed that in a first approximation, sweeping gap can simulate the overall MLC related dose contribution for IMRT field, because it was mostly related to the time that the leaves are in the treatment field, even though the exact shape of the dose distribution is different. In a clinical plan, due to differences between the inter- and intra-MLC, leakage will lead to additional effects, such as tongue and groove effect and off-axis dependence of MLC leakage related to different energy of the beam. Due to the complexity of the MLC design and noise in MC simulations, these effects are best characterized and dealt with in the dose calculation algorithm by adopting an empirical approach [159 – 161], in which special “delayed” sweeping gaps are used to determine T&G, as well as off-axis dependence of MLC properties for various depths in water. In the presence of high-Z material these effects might be different due to difference in beam quality.

## Part C

### IV.3. DER for clinical spectra – optimal beam quality for NPRT

Recent microdosimetric studies using MC techniques focused on the calculation of the local DER at distances from 2 nm to ~100  $\mu\text{m}$  from the GNP surface [31-32, 75-78]. For a standard 6 MV

linac, the dose-enhancement-factor (DEF) was found to be  $\sim 8$  for spatially distributed nanoparticles at 7 mgAu/g concentration [31], while measured and calculated relative-biological-effectiveness (RBE) values had a range of 1.2–2.1 [92]. However, the various DEF reported in the literature have been derived in an indirect fashion and they utilize complex normalization schemes. Thus, caution should be taken against a direct comparison of DEF values from one report to another. In contrast, our work focuses on the dosimetric environment of single or agglomerated solid nanoparticles, and our DER for 6 MV linac is  $\sim 1.7$  ( $q=[5 \times 5 \text{ cm}^2$ , CAX, OB, depth=10 cm],  $s=100 \text{ nm}$ ,  $x=1 \text{ }\mu\text{m}$ ), which was consistent with the experimental RBE results [13].

A series of other studies investigated the potential biological benefit when GNPs were injected into the tumor [94–97]. It has been observed that the DER and its local distribution depend on the size of GNP, its concentration and aggregation status, as well as beam quality at a point within the treated volume [31–32, 75–78, 92–94].

Our results demonstrated that DER is sensitive to beam quality, which is dependent on many factors. From the perspective of spectral variations of the clinical beam, having different low-energy content results in different photo-absorption and Auger electron production rates. Therefore, even for a given beam and irradiation technique, the beam quality spatially varies, and it is recommended that the beam quality is examined for each individual region/ case to maximize the benefits of GNP and to avoid misinterpretations.

The greatest DER is observed for split-IMRT fields because in this case each of the split beams contributes out-of-field scatter dose to the complimentary field. Therefore, it is expected that for large volumes treated with split and large IMRT fields with small MLC gaps, the benefit of GNP therapy is the greatest. Our results strongly suggest that the exact DER values must be calculated per plan and per region of interest.

In the current study we considered several possible GNP-cellular target scenarios. Currently there is no clear evidence that all GNPs are taken up by cells the same way (by e.g., the cell nucleus) or aggregated at the cell membrane. In addition, in a given x-ray delivery (within cell cultures, animal models or in the future humans) there could be various possible geometrical configurations. Therefore, in this dissertation we did not limit the study to a specific situation. We calculated  $DER(x)$  with high spatial resolution (step size varying from 2 nm to 10 nm) and reported both point-wise and spatially averaged DE ratios over various ranges of interest, coinciding with important cellular and molecular scales. This method of data presentation had the added benefit of permitting the presentation of a vast amount of data in a concise form.

Thus, we distinguished three possible scenarios according to where the GNP was located with respect to a cell: (1) nanoparticles aggregated outside the cell, near its membrane, (2) particles near the cell nucleus, and (3) nanoparticles near or incorporated into the chromosome. In the case

of GNPs aggregating outside of the cell, the closest target was the cell membrane while the nucleus or the DNA was at least 1  $\mu\text{m}$  away (e.g. endothelial cell). In this geometry, even for the smallest GNP size and the most conservative scenario, DER=2.3 on the GNP surface and was  $\sim 2.2$  over the cell membrane. The largest DER values were calculated for split-IMRT and they were 6.1 on the GNP surface and 4.1 over the range of the cell membrane. Besides split-IMRT fields, unflattened beams with large field were also found to be the most beneficial scenarios for GNP-RT, as the DER was 4.7 and 3.3 for GNP surface and over the membrane, respectively. The value of DER, produced by a 100 nm GNP cluster averaged over 1  $\mu\text{m}$  range, was 2.5 for split-IMRT (depth=10 cm) and  $\sim 2.0$  for unflattened large fields (14x28  $\text{cm}^2$ , d=10 cm). Within the range extending from 2 - 4  $\mu\text{m}$  measured from the GNP surface, DER underwent a gradual but minimal decrease of about  $<10\%$ . Considering that the distance from the membrane to the cell center is about 1  $\mu\text{m}$  (endothelial cells) to  $\sim 4 \mu\text{m}$  (tumor cells) the value of DER (for range  $x=1-4 \mu\text{m}$ ) was sufficient to estimate the magnitude of DE from GNP located at the cell membrane.

The second possible scenario was when the GNP penetrated the cell membrane and was situated close to the cell nucleus. DER averaged over the range of the nucleus ( $\sim 1 \mu\text{m}$ ), could reach  $\sim 2.5$  ( $s=100 \text{ nm}$ ), if split-IMRT fields were used. The benefit would be greater for tumors that are deeper: due to scatter, there is an increase of DER with depth, reaching values 1.3–2 depending on the linac type. The DER was even larger for out-of-field areas. Therefore, if the GNP is located in an out-of-field area, the DER averaged over the entire cell, (2  $\mu\text{m}$  range) varies from 1.3–4, depending on the linac type.

When the GNPs are incorporated into the chromosome the maximum DER may be achieved [Figure 38]. In the most conservative scenario under this geometry (STD, open beam, shallow depth, small field, CAX) DER=2. The GNP size is important because a smaller GNP can penetrate the cell membrane easier and migrate closer to the DNA. However, a smaller GNP has a smaller photoabsorption probability, which leads in most cases to smaller DER. In the cases examined, the difference between DER generated by 10 nm vs. 100 nm GNP clusters was in the range of 14–287%. The smallest difference was observed for shallow depths and small field sizes, and the largest differences were seen for out-of-field areas of unflattened beams and larger depths.

An important aspect is the possible unintended DER in normal tissue when GNPs aggregate outside of the treatment field. Because DER increases in the out-of-field volumes, precise knowledge of the GNP accumulation within and outside of the tumor is essential. The presence of GNP, even in small concentrations, in normal tissue could adversely impact the treatment outcome.

## V. CONCLUSIONS

### PART A: Monte Carlo simulation of the medical linac and modification of the head assembly

A Monte Carlo model of Varian 6 EX linac was developed and verified for STD and FFF modes, for in-field and out-of-field regions, for open and dynamic IMRT fields. Beam energy of FFF linac was adjusted to match PDD of the STD, which lead to an even larger dose rate benefit. Characterization of the impact of these modifications on IMRT fields was conducted by comparing closed MLC and sweeping gap tests for several field sizes and gap openings. Transmission through the MLC was smaller for FFF linac, because the mean energy of the beam was smaller. By adjusting the penetration of the beam, MLC transmission reached its original value. Similar behavior was noticed in the sweeping gap tests for different gap sizes.

Moreover, an alternative design of linac target area was studied to determine the relation between the resulting dose rate, peripheral dose and beam uniformity. This study showed that by changing mean angular spread  $5^\circ$  to  $10^\circ$  (depending on the field size) results in beam of sufficient flatness, which can be utilized to generate more monitor unit efficient IMRT plans, and decrease treatment time by a factor of  $\sim 2$ . Angles close to  $14^\circ$  or larger than this value must not be used as they lower dose in the area close to the edges of the field. For field sizes smaller than  $6 \times 6 \text{ cm}^2$  (e.g. SBRT) modulation of the beam is not needed as the beam is already flat enough [166].

A heuristic function  $(1+b \cdot r^n)$  parameterizing change of flatness for FFF linac can be used. The model predicts accurately ( $<1\%$  difference) flatness changes for all open beam field sizes and depths for the treatment field area. For small field sizes the accuracy of the model is around  $2\%$ , while it was tested and worked with accuracy  $2\text{-}3\%$  for sweeping gap tests of gap size  $G=10, 20 \text{ mm}$ .

Increasing the mean angular spread angle lead to a slightly increased peripheral dose of FFF linac. The dose increase is depended on the field size and spread angle. For larger field sizes ( $30 \times 30 \text{ cm}^2$ ) and spread angles of  $10^\circ$ , PD was still lower than the dose for STD linac.

### PART B: Clinical beam quality and beam perturbation

Spectral difference between standard and FFF 6 MV beamlines were studied for an extensive number of irradiation conditions. Reference data for these clinical beams were produced, followed by qualitative and quantitative analysis of differential effects observed in different spectral regions or in the effective beam quality for various high-Z materials.

In the past few years, there has been an increase in the number of publications regarding dose enhancement with nanoparticles, mostly from gold. The resulting microscopic DER varies for different studies due to different set up and normalization schemes in MC, as well as the studied

scales (micro/ nano -scopic vs macroscopic). As our study implies the knowledge of the differential effects of dose enhancement for different clinical scenarios, materials and spectral areas may be of great importance in the assessment of the impact on dosimetry.

Qualitative analysis revealed similar patterns and shapes between spectra for STD and FFF linacs, with FFF beams being softer due to the lack of the flattening filter to attenuate the low-energy component of the beam. There was a progressive shift of the spectra towards lower energies for both linac types with increased depth, field size and distance. This effect was clearer when the in-field versus out-of-field spectra were compared. Spectral shifting is related to the increased scatter component of the beam, which leads to increased photoabsorption. In the cases of IMRT qualitative assessment of the spectra lead to similar observations. In general, the relative changes, between different conditions, were smaller for FFF linac spectrum compared to the STD linac. The main reason for that seemed to be the higher component of low energy particles, which was the main cause of larger phantom scatter compared to STD spectra. Due to the increased phantom scatter, particle energies were more “uniformly” distributed for FFF spectra so relative changes were smaller.

In the second part of the spectral analysis the relationship between spectral changes and dose were investigated. Metrics  $m(E)$  and  $M$  were calculated in order to investigate and characterize the dose perturbation due to different spectral scenarios and for different materials. Different spectral scenarios lead to different dose perturbations, which were increased for higher  $Z$  materials. The differential effect was directly related to the low-energy part of the spectrum (below 200 keV). For the remaining part of the spectrum, the metric  $M$  remained almost constant.

### **PART C: DER for clinical spectra – optimal beam quality for NPRT**

The results for GNP showed predominantly the same behaviors as for CRT, however the absolute values of DER were larger as expected, due to extra Auger electron production in GNP. Comparison of the data between Part B (macroscopic) and Part C (micro-/ nanoscopic) showed larger values for the second one from 20% to 85% (case of Gold) depending on the case studied, while relative differences were higher for STD linac compared to FFF. Nano/ micro calculation depends on distances and does not depend on the macroscopic concentration, but only on the nearest neighboring clusters of GNPs. On the other hand, macro calculation depends only on the concentration of the material.

Computations suggest that the largest DER value occurs for split-IMRT, larger depths for out-field areas, large fields sizes and/or for FFF-type linac. The DER study showed that the differential effects, which should be considered, were the depth of the tumor as well the position of the GNP with respect to the treatment field, as the DER effects were much larger for out-of-field areas and GNP accumulation of the normal tissue was of importance. Finally, the location of

GNPs with respect to the cellular or molecular target has to be taken into account, in relation to the experimental cell survival or tumor survival data in vivo.



## V. PhD OUTCOME

### PAPERS ACCEPTED/ SUBMITTED IN PEER-REVIEWED SCIENTIFIC JOURNALS

1. **Tsiamas P**, Seco J, Han Z, Bhagwat M, Maddox J, Kappas C, Theodorou K, Makrigiorgos M, Marcus K and Zygmanski P, "A modification of flattening filter free linac for IMRT", Medical Physics 2011, (38), 2342 - 2352.
2. **P Tsiamas**, B Liu, F Cifter, W F. Ngwa, R I Berbeco, C Kappas, K Theodorou, K Marcus, M G. Makrigiorgos, E Sajo, P Zygmanski, "Impact of beam quality on megavoltage radiotherapy treatment techniques utilizing gold nanoparticles for dose enhancement", Under review - Radiotherapy & Oncology
3. **P Tsiamas**, E. Sajo, F. Cifter, K. Theodorou, C. Kappas, M. Makrigiorgos, K. Marcus, P. Zygmanski, "Beam quality and dose perturbation of 6 MV flattening-filter-free beams", under review - European Journal of medical physics.
4. Ngwa W, **Tsiamas P**, Zygmanski P, Makrigiorgos GM, Berbeco RI., "A multipurpose quality assurance phantom for the small animal radiation research platform (SARRP)", Phys Med Biol. May 7;57(9):2575-86, 2012.
5. F Cifter, **P Tsiamas**, P Zygmanski, E Sajo, "Parametric Study of Gold Nanoparticle Dose Enhancement Using Deterministic Computations" Under review - Medical Physics
6. Sajo E, **Tsiamas P**, Cifter F, Zygmanski P "Deterministic computations of nanoscale energy deposition about nanoparticles", Medical Physics
7. A Detappe, **P Tsiamas**, W Ngwa, P Zygmanski and R Berbeco, "The effect of flattening filter free delivery on endothelial dose enhancement during gold nanoparticle-aided radiotherapy", Under Review - Phys Med Biol.
8. P Zygmanski, W Hoegele, **P Tsiamas**, F Cifter, E Sajo, "A stochastic model of cell survival for high-Z nanoparticle radiotherapy", Under review - Medical Physics.
9. L Wack, W Ngwa, E Tryggestad, **P Tsiamas**, R Berbeco, S K Ng, J Hesser and P Zygmanski, "Kilovoltage beam of a small animal irradiator: Film dosimetry in homogeneous and heterogeneous media", under review - European Journal of medical physics.

### ORAL PRESENTATIONS

1. **Tsiamas P**, Seco J, Han Z, Bhagwat M, Maddox J, Kappas C, Theodorou K, Makrigiorgos M, Marcus K and Zygmanski P, "A modification Filter Free (FFF) linac", NEAAPM - young investigation symposium, May 2011.
2. **Tsiamas P**, Bhagwat M, Kappas C, Theodorou K, Makrigiorgos M, Marcus K and Zygmanski P, "A straightforward conversion of IMRT plans optimized for the standard linac for delivery on FFF linac without re-optimization", International Workshop of Recent Advances in Monte Carlo Techniques for Radiation Therapy June 8-10, 2011 Montreal - Canada.
3. Ngwa W, **Tsiamas P**, Zygmanski P, Makrigiorgos GM, Berbeco RI., "A Multipurpose Quality Assurance Phantom for the Small Animal Radiation Research Platform (SARRP)", TU-C-BRB-06: Med Phys., 39 (6), 3899, 2012.

### POSTER PRESENTATIONS

1. **Tsiamas P**, Sajo E, Cifter F, Theodorou K, Kappas K, Makrigiorgos M, Marcus K, Zygmanski P., "Optimal Clinical Megavoltage X-Ray Beam Quality for Contrast Enhanced RT (CERT)", SU-E-T-35, Med Phys., Jun;39 (6), 3710, 2012.
2. **Tsiamas P**, Seco J, Han Z, Bhagwat M, Maddox J, Kappas C, Theodorou K, Makrigiorgos M, Marcus K and Zygmanski P, "Matching of Flattening-Filter-Less (FFL) to Standard (STD) linac beams based on Monte Carlo simulations Innovation/Impact:", SU-GG-T-387, Med. Phys. June;37, 3275, 2010.

## V. FUTURE GOALS

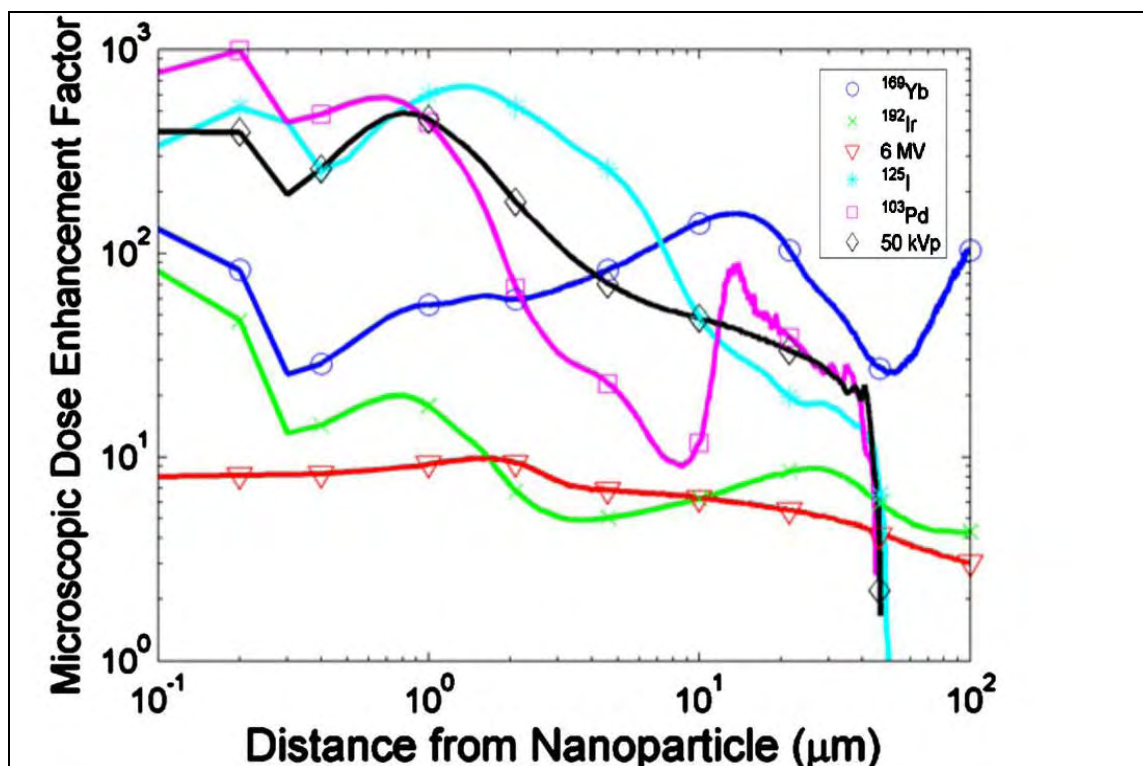
Development of new x-ray sources or modifications of the presently existing linac sources in combination with GNP radiation therapy, are two very exciting fields with strong indications of further research. Regarding the first one, of further interest are practical solutions for electron beam and target design, which would improve the photon beam flatness without the need of flattening filter, and leading to optimal dose rate within the target and peripheral dose outside of it. Moreover, clinical spectral study indicates directions for further research related to the original questions of beam flatness in IMRT (or VMAT) applications for larger volume targets or targets away from the central axis.

GNP radiation therapy can be a potential solution for more efficient utilization of radiation. In order for this field to progress beyond crude estimates, new imaging at the tissue / cellular/ sub-cellular level and more accurate dose calculation methods have to be developed. Accurate knowledge of the dose deposition mechanism in cellular and sub-cellular level and how this is translated in biological damage are still required for the latest one, so new simulation techniques and codes must be developed. The sensitivity of the results up until now and the variety of results depended on the geometrical set up and simulated parameters, indicates that measurements and simulation must be done consistently and clarification of the units scored must be reported with caution.

A potential future direction towards all the above could be the development of a new beam line, which will be dedicated to enhanced dose delivery and radiobiological damage of the tumor in the presence of nanoparticles, as well as to develop in vivo imaging and dosimetry using nanotechnology.

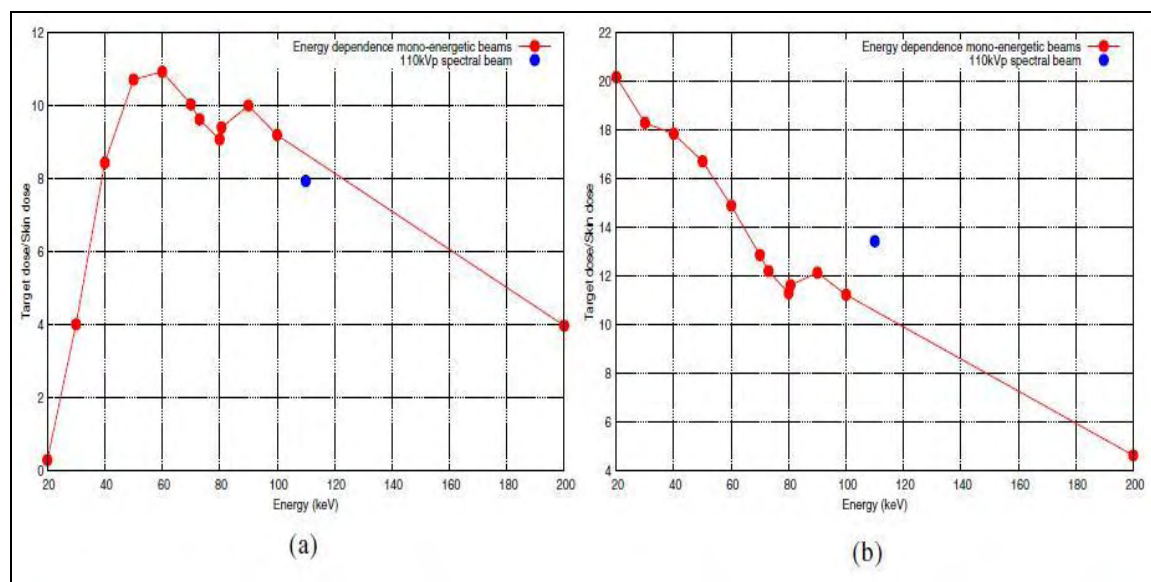
## Appendix

Image 1:



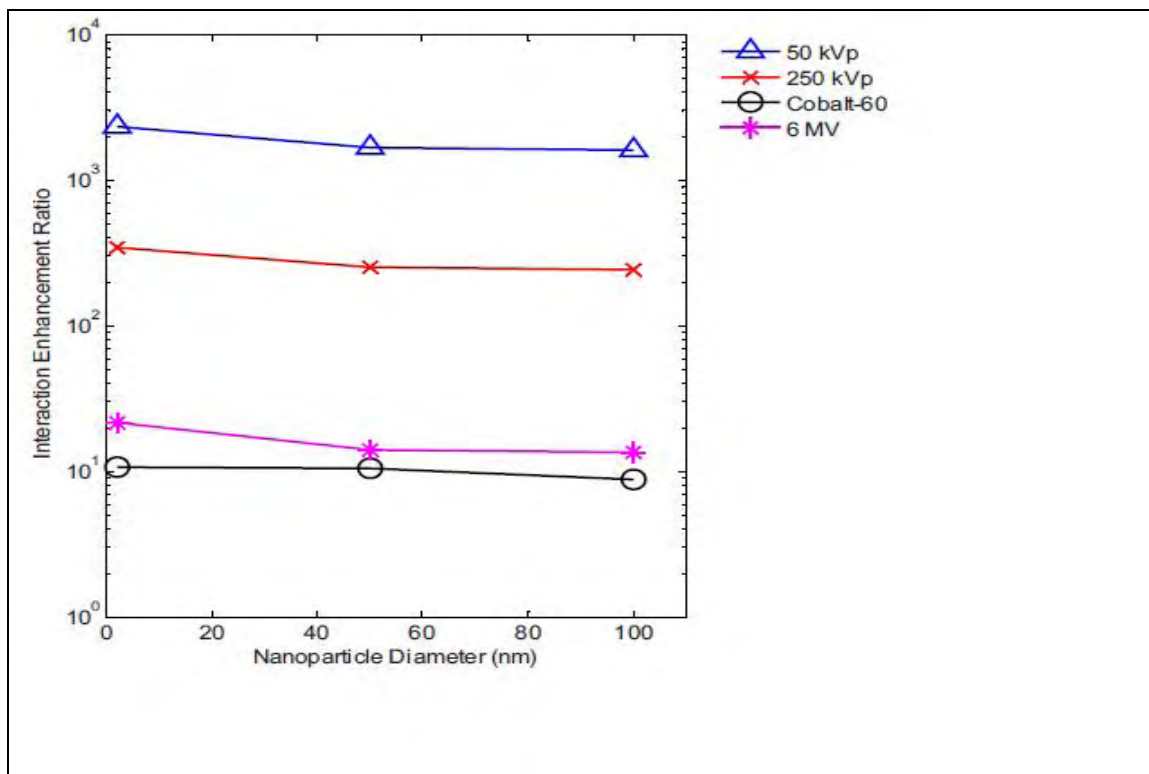
Reference: [31]

Image 2:



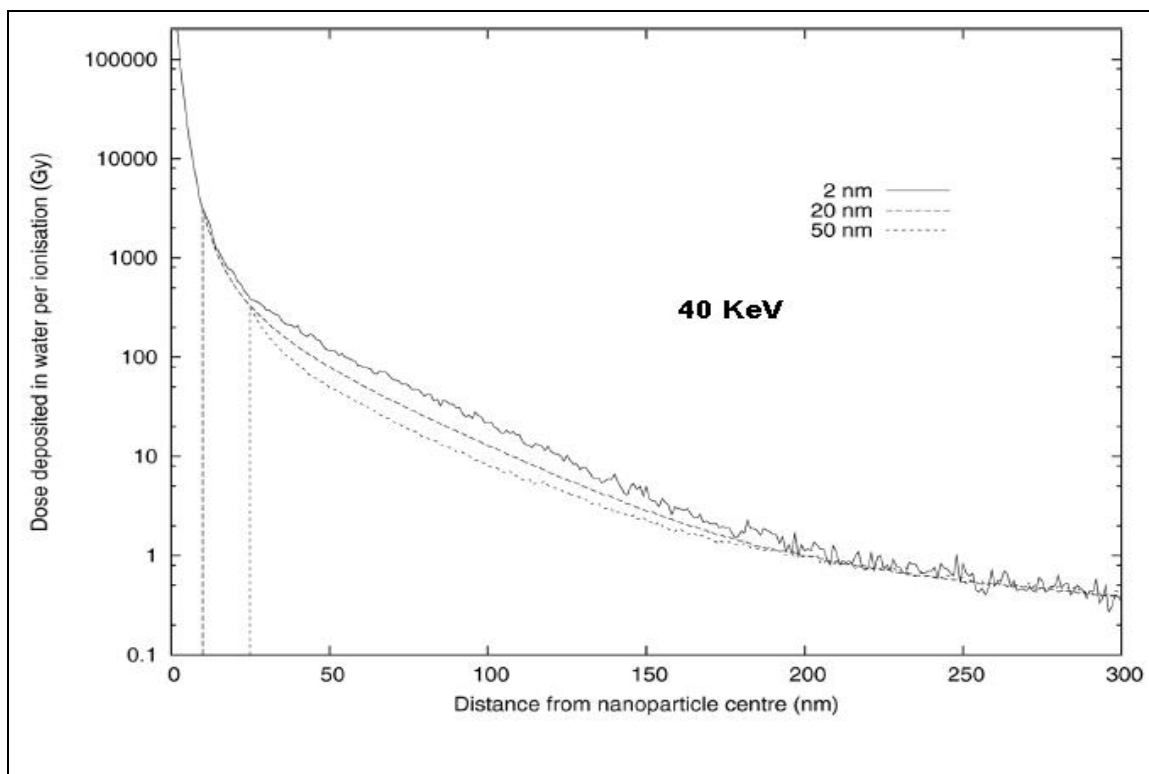
Reference: [77]

**Image 3:**



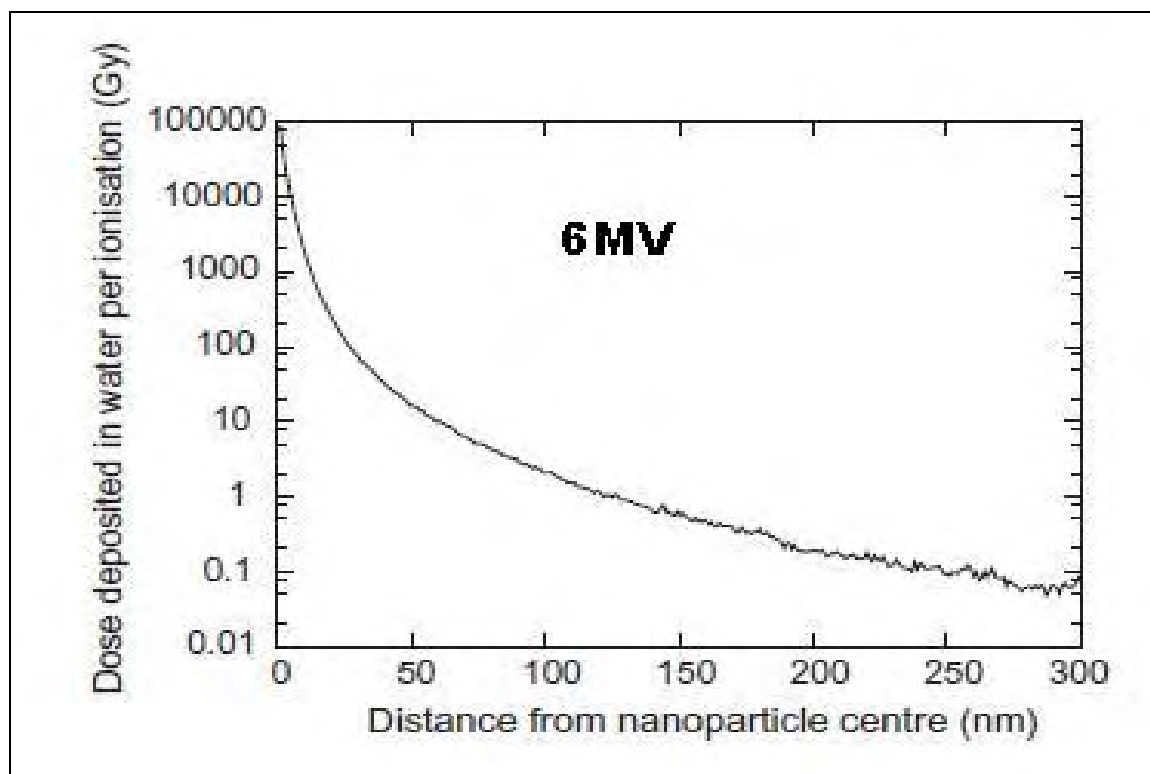
Reference: [32]

**Image 4:**



Reference: [91]

**Image 5:**



Reference: [92]

## VI. REFERENCES

1. N. Metropolis and S. Ulam, "The Monte Carlo method", J. of the Americ. Stat. Association, 44: 247, 1949.
2. A. F. Bielajew, "Fundamentals of the Monte Carlo method for neutral and charged particle transport", 2001.
3. P. Tsiamas, "Out of field Spectra determination of Electra's SL-18 Linac with MLC, for 6 and 15 MV, with Monte Carlo simulation.", MSc Dissertation, University of Patras, School of Medicine and Physics Department, Department of Medical Physics, 2008.
4. I. Kawrakow, E. Mainegra-Hing, D.W.O. Rogers, F. Tessier and B.R.B. Walters, "The EGSnrc Code System: Monte Carlo Simulation of Electron and Photon Transport", NRCC Report PIRS-701, 2011.
5. D.W.O. Rogers, "Monte Carlo Techniques in Radiotherapy", Physics in Canada, Medical Physics, 58(2): 63-70, 2002.
6. D.W.O. Rogers, B. A. Faddegon, G. X. Ding, C.-M. Ma, J. We, T. R. Mackie "BEAM: A Monte Carlo code to simulate radiotherapy treatment units", Med. Phys. 22(5): 503-524, 1995.
7. P. Mayles, A. Nahum, J-C Rosenwald, "Handbook of Radiotherapy physics: theory and Practice", Chapter 15<sup>th</sup>, Taylor & Francis, Third Edition, 2007.
8. M. J. Berger. "Monte Carlo Calculation of the penetration and diffusion of fast charged particles", Methods in Comput. Phys., 1: 135 - 215, 1963.
9. S. A. Goudsmit and J. L. Saunderson, "Multiple scattering of electrons", Phys. Reviews, 57: 24 -29, 1940.
10. S. A. Goudsmit and J. L. Saunderson, "Multiple scattering of electrons II", Phys. Reviews, 58: 36-42, 1940.
11. E. W. Larsen, "A theoretical derivation of the condensed history algorithm", Ann. Nucl. Energy, 19(10-12): 701-714, 1992.
12. X-5 Monte Carlo Team "MCNP - A General Monte Carlo N-Particle Transport Code, Version 5", 2008.
13. F. Salvat, J. M. Fernández-Varea and J. Sempau, "PENELOPE - A Code System for Monte Carlo Simulation of Electron and Photon Transport", Workshop Proceedings Issy les Moulineaux, 7-10 July, France 2003.
14. "Physics Reference Manual Version: geant4 9.5.0, 2nd December, 2011"
15. S. Incerti, G. Baldacchino, M. Bernal, R. Capra, C. Champion, Z. Francis, S. Guatelli, P. Guèye, A. Mantero, B. Mascialino, P. Moretto, P. Nieminen, A. Rosenfeld, C. Villagrasa and C. Zacharatou, "The Geant4-DNA project", 2009.



16. I. Kawrakow, "VMC++, electron and photon Monte Carlo calculations optimized for Radiation Treatment Planning", [http://www.irs.inms.nrc.ca/papers/vmcpp\\_paper/vmcpp\\_paper.pdf](http://www.irs.inms.nrc.ca/papers/vmcpp_paper/vmcpp_paper.pdf).
17. D.W. Rogers, "Fifty years of Monte Carlo simulations for medical physics" *Phys. Med. Biol.* 51(13): R287–301, 2006.
18. E. Spezi and G. Lewis, "An overview of Monte Carlo treatment planning for radiotherapy", *Radiat. Prot. Dosim.*, 131(1): 123–129, 2008.
19. I. J. Chetty, B. Curran, J.E Cygler, J.J DeMarco, G. Ezzell, B.A Faddegon, I. Kawrakow, P.J Keall, H. Liu, C.M Ma, D.W Rogers, J. Seuntjens, D. Sheikh- Bagheri and J.V Siebers, "Report of the AAPM Task Group No. 105: Issues associated with clinical implementation of Monte Carlo-based photon and electron external beam treatment planning" *Med. Phys.*, 34(12): 4818–4853, 2007.
20. S. Incerti, A. Ivanchenko, M. Karamitros, A. Mantero, P. Moretto, H.N Tran, B. Mascialino, C. Champion, V.N Ivanchenko, M.A Bernal, Z. Francis, C. Villagrasa, G. Baldacchin, P. Gueye, R. Capra, P. Nieminen and C. Zacharatou, "Comparison of GEANT4 very low energy cross section models with experimental data in water", *Med. Phys.* 37(9): 4692–4708, 2010.
21. S. Chauvie, Z. Francis, S. Guatelli, S. Incerti, B. Mascialino, P. Moretto, P. Nieminen and M.G Pia, "Geant4 physics processes for microdosimetry simulation: design foundation and implementation of the first set of models", *IEEE Trans. Nucl. Sci.*, 54(6): 2619–2628, 2007.
22. M. A. Bernal and J. A. Liendo, "An investigation on the capabilities of the PENELOPE MC code in nanodosimetry", *Med. Phys.* 36(2), 2009.
23. V. A. Semenenko, J. E. Turner and T. B. Borak, "NOREC, a Monte Carlo code for simulating electron tracks in liquid water", *Radiat Environ Biophys.*, 42(3): 213–217, 2003.
24. A.V. Lappa, E.A. Bigildeev, D.S. Burmistrov and O.N. Vasilyev, "'Trion' code for radiation action calculations and its application in microdosimetry and radiobiology", *Radiat Environ Biophys.*, 32(1): 1-19, 1993.
25. S. H. Cho, O. N. Vassiliev and J. L. Horton Jr, "Comparison between an event-by-event Monte Carlo code, NOREC, and ETRAN for electron scaled point kernels between 20 keV and 1 MeV", *Radiat. Environ. Biophys.*, 46(1): 77–83, 2007.
26. D. Emfietzoglou, G. Papamichael, K. Kostarelos and M Moscovitch, "A Monte Carlo track structure code for electrons (~10 eV–10 keV) and protons (~0.3–10 MeV) in water: partitioning of energy and collision events", *Phys. Med. Biol.* 45(11): 3171–3194, 2000.
27. P. Mayles, A. Nahum, J-C Rosenwald, "Handbook of radiotherapy physics: Theory and practice", chapter 5, Taylor & Francis, Third Edition, 2007.
28. L. H. Toburen, "Challenges in Monte Carlo track structure modeling", *Int. J. of Radiation Biology*, January–February; 88(1–2): 2–9, 2012.

29. H. Nikjoo, S. Uehara, I.G. Khvostunov, F.A. Cucinotta, W.E. Wilson and D.T. Goodhead, "Monte Carlo track structure for radiation biology and space applications", 11th Annual NASA Space Radiation Health Investigators' Workshop, Arona, Italy, May 27-31, 2000.
30. R. M. Thomson and I. Kawrakow, "On the Monte Carlo simulation of electron transport in the sub-1 keV energy range, *Med. Phys.* 38(8): 4531–4534, 2011.
31. B. Jones, S. Krishnan and S. H. Cho, "Estimation of microscopic dose enhancement factor around gold nanoparticles by Monte Carlo calculations", *Med. Phys.*, 37(7): 3809–3816, 2010.
32. M. K. K. Leung, James C. L. Chow, B. D. Chithrani, M. J. G. Lee and B. Oms, "Irradiation of gold nanoparticles by x-rays: Monte Carlo simulation of dose enhancements and the spatial properties of the secondary electrons production", *Med. Phys.*, 38(2): 624–631, 2011.
33. P. Lazarakis, M. U. Bug, E. Gargioni, S. Guatelli, H. Rabus and A. B. Rosenfeld, "Comparison of nanodosimetric parameters of track structure calculated by the Monte Carlo codes Geant4-DNA and PTra", *Phys. Med. Biol.* 57(5): 1231–1250, 2012.
34. L. J. Lorence, Jr. and D. E. Beutler, "Radiation Transport Phenomena and Modeling, Part A: Codes, Part B: Applications and Examples", SAND97–2135, UC–705, 1997.
35. L. J. Lorence, J. E. Morel, and G. D. Valdez, "Physics Guide to CEPXS: A multigroup coupled electron–photon cross section generating code", SAND89-1685, Sandia National Laboratory, 1989.
36. M.L. Williams and E. Sajo, "Deterministic Calculations of Photon Spectra for Clinical Accelerator Targets", *Medical Physics*, 29(6): 1019-1028, 2002.
37. G. Kraft, "Heavy ion tumor therapy: from the scientific principles to the clinical routine", *Nucl. Phys. News* 17(1): 24-29, 2007.
38. W.P. Levin, H. Kooy, J.S. Loeffler and T.F. DeLaney, "Proton beam therapy", *British Journal of Cancer*, 93(8): 849–854, 2005.
39. K.J. Russell, R.J. Caplan, G.E. Laramore, C.M Burnison, M.H Maor, M.E Taylor, S. Zink, L.W Davis and T.W Griffin, "Photon versus fast neutron external beam radiotherapy in the treatment of locally advanced prostate cancer: results of a randomized prospective trial", *Int J Radiat. Oncol Biol Phys.*, 28(1): 47-54, 1993.
40. C.F. Von Essen, M.A. Bagshaw, S.E. Bush, A.R. Smith and M.M. Kligerman, "Long-term results of pion therapy at Los Alamos", *Int J Radiat Oncol Biol Phys.*, 13(9): 1389-1398, 1987.
41. P.F. O' Brien, B. A. Gillies, M. Schwartz, C. Young and P. Davey, "Radiosurgery with unflattened 6-MV photon beams", *Med. Phys.*, 18(3): 519-521, 1991.
42. S. Zefkili, C. Kappas and J-C. Rosenwald, "On-axis and off-axis primary dose component in high energy photon beams", *Med. Phys.*, 21(6): 799-808, 1994.

43. W. Fu, J. Dai, Y. Hu, D. Han and Y. Song, "Delivery time comparison for intensity-modulated radiation therapy with/without flattening filter: a planning study", *Phys. Med. Biol.*, 49(8): 1535-1547, 2004.
44. U. Titt, O. N. Vassiliev, F. Pönisch, L. Dong, H. Liu, and R. Mohan, "A flattening filter free photon treatment concept evaluation with Monte Carlo", *Med. Phys.*, 33(6): 1595-1602, 2006.
45. O. N. Vassiliev, U. Titt, S. F. Kry, F. Pönisch, M. T. Gillin, and R. Mohan, "Monte Carlo study of photon fields from a flattening filter-free clinical accelerator", *Med. Phys.*, 33(4): 820-827, 2006.
46. O. N. Vassiliev, U. Titt, S. F. Kry, R. Mohan and M. Gillin, "Dosimetric properties of photon beams from a flattening free clinical accelerator", *Phys. Med. Biol.*, 51(7): 1907-1917, 2006.
47. F. Pönisch, U. Titt, O. N. Vassiliev, S. F. Kry, and R. Mohan, "Properties of unflattened photon beams shaped by a multileaf collimator", *Med. Phys.*, 33(6): 1738-1746, 2006.
48. S. F. Kry, U. Titt, F. Pönisch, D. Followill and O. N. Vassiliev, "A Monte Carlo model for calculating out-of-field dose from a Varian 6MV beam", *Med. Phys.*, 33(11): 4405-4413, 2006.
49. X. R. Zhu, Y. Kang, and M. T. Gillin, "Measurements of in-air output ratios for a linear accelerator with and without the flattening filter", *Med. Phys.*, 33(10): 3723 -3733, 2006.
50. U. Titt, O. N. Vassiliev, F. Pönisch, S. F. Kry, and R. Mohan, "A Monte Carlo study of backscatter in a flattening filter free clinical accelerator", *Med. Phys.* 33(9): 3270-3273, 2006.
51. J. Olofsson, T. Nyholm, A. Ahnesjö and M. Karlsson, "Optimization of photon beam flatness for radiation therapy", *Phys. Med. Biol.*, 52(6): 1735-1746, 2007.
52. J. Cashmore, "The characterization of unflattened photon beams from a 6 MV linear accelerator", *Phys. Med. Biol.*, 53(7): 1933-1946, 2008.
53. G. Xiong and D. W. O. Rogers, "Relationship between %dd(10)x and stopping-power ratios for flattening filter free accelerators: A Monte Carlo study", *Med. Phys.*, 35(5): 2104-2109, 2008.
54. S. F. Kry, R. M. Howell, J. Polf, R. Mohan and O. N. Vassiliev, "Treatment vault shielding for a flattening filter-free medical linear accelerator", *Phys. Med. Biol.*, 54(5): 1265-1273, 2009.
55. B. Bednarz and X. G. Xu, "Monte Carlo modeling of a 6 and 18 MV Varian Clinac medical accelerator for in-field and out-of-field dose calculations: development and validation", *Phys. Med. Biol.*, 54(4): N43-N57, 2009.
56. D. Georg, G. Kragl, S. af Wettersterdt, P. McCavana, B. McClean and T. Knoos, "Photon beam quality variations of a flattening filter free linear accelerator", *Med. Phys.*, 37(1): 49-53, 2010.
57. G. Kragl, S. af Wetterstedt, B. Knäusl, M. Lind, P. McCavana, T. Knöös, B. McClean and D. Georg, "Dosimetric characteristics of 6 and 10 MV unflattened photon beams", *Radiotherapy and Oncology*, 93(1): 141-146, 2009.

58. C. Ceberg, S. Johnsson, M. Lind and T. Knöös, "Prediction of stopping-power ratios in flattening-filter free beams", *Med. Phys.*, 37(3): 1164–1168, 2010.
59. S. F. Kry, O. N. Vassiliev and R. Mohan, "Out-of-field photon dose following removal of the flattening filter from a medical accelerator", *Phys. Med. Biol.*, 55(8): 2155–2166, 2010.
60. P. Tsiamas, J. Seco, Z. Han, M. Bhagwat, J. Maddox, C. Kappas K. Theodorou, M. Makrigiorgos, K. Marcus and P. Zygmanski, "A modification of flattening filter free linac for IMRT", *Med. Phys.*, 38(5): 2342–2352, 2011.
61. J. Seco, G. C. Sharp, J. Turcotte, D. Gierga, T. Bortfeld, and H. Paganetti, "Effects of organ motion on IMRT treatments with segments of few monitor units", *Med. Phys.*, 34(3): 923–934, 2007.
62. T. Kim, L. Zhu, T.S Suh, S. Geneser, B. Meng and L. Xing, "Inverse planning for IMRT with non uniform beam profiles using total-variation regularization (TVR)", *Med. Phys.*, 38(1): 57–66, 2011.
63. L. Wang, E. Mok, and L. Xing, "Pros and cons of flattening filter free IMRT: A comparison with conventional IMRT with flattened beams", *Med. Phys.*, 37(6): 3375–3375, 2010.
64. O. N. Vassiliev, S. F. Kry, D. A. Kuban, M. Salehpour, R. Mohan and U. W. Titt, "Treatment planning study of prostate cancer intensity-modulated radiotherapy with a Varian clinical operated without a flattening filter", *Int. J. Radiation Oncology Biol. Phys.*, 68(5): 1567–1571, 2007
65. O. N. Vassiliev, T. A. Wareing, I.M Davis, J. McGhee, D. Barnett, J.L Horton, K.Gifford, G. Failla, U. W. Titt and F. Mourtada, "Feasibility of a multigroup solution method for three-dimensional radiotherapy dose calculations", *Int. J. Radiation Oncology Biol. Phys.*, 72(1): 220–227, 2008.
66. S. F. Kry, U. W. Titt, F. Ponisch, O. N. Vassiliev, M. Salehpour, M. Gillin and R. Mohan, "Reduced neutron production through use of a Flattening-Filter-Free accelerator", *Int. J. Radiation Oncology Biol. Phys.*, 68(4): 1260–1264, 2007.
67. H. H. Liu and F. Verhaegen, "An investigation of energy spectrum and linear energy variations in mega-voltage photon beams used in radiotherapy", *Radiation Protection Dosimetry*, 99(1–4): 425–427, 2002.
68. S. B. Scarboro, D. S. Followill, R. M. Howell and S. F. Kry, "Variations in photon energy spectra of a 6 MV beam and their impact on TLD response", *Med. Phys.*, 38(5): 2619–2628, 2011.
69. A. Tsechanski, Y. Krutman and S Faermann, "On the existence of low-energy photons (<150 keV) in the unflattened x-ray beam from an ordinary radio therapeutic target in a medical linear accelerator", *Phys. Med. Biol.*, 50(23): 5629–5639, 2005.

70. S. Young Jang, H. H. Liu, R. Mohan and J. V. Siebers, "Variations in energy spectra and water-to-material stopping-power ratios in three-dimensional conformal and intensity-modulated photon fields", *Med. Phys.*, 34(4): 1388-1397, 2007.
71. G.X Ding, "Energy spectra, angular spread, fluence profiles and dose distributions of 6 and 18 MV photon beams: results of Monte Carlo simulations for a Varian 2100EX accelerator", *Phys. Med. Biol.*, 47(7): 1025-1046, 2002.
72. B. A. Faddegon, V. Wu, J. Pouliot, B. Gangadharan and Ali Bani-Hashemi, "Low dose megavoltage cone beam computed tomography with an unflattened 4 MV beam from a carbon target", *Med. Phys.* 35(12): 5777-5786, 2008.
73. D. Sawkey, M. Lu, O. Morin, M. Aubin, S. S. Yom, A. R. Gottschalk, A. Bani-Hashemi and B. A. Faddegon, "A diamond target for megavoltage cone-beam CT", *Med. Phys.*, 37(3): 1246 – 1253, 2010.
74. Z. Han, S. K. Ng, M. S. Bhagwat, Y. Lyatskaya, and P. Zygmanski, "Evaluation of MatriXX for IMRT and VMAT dose verifications in peripheral dose regions", *Med. Phys.*, 37(7): 3704–3714, 2010.
75. S. H. Cho, "Estimation of tumor dose enhancement due to gold nanoparticles during typical radiation treatments: a preliminary Monte Carlo study", *Phys. Med. Biol.*, 50(15): N163-N173, 2005.
76. S. H. Cho, B. L. Jones and S. Krishnan, "The dosimetric feasibility of gold nanoparticle-aided radiation therapy (GNRT) via brachytherapy using low-energy gamma- / x-ray sources", *Phys. Med. Biol.*, 54(16): 4889-4905, 2009.
77. F. Van den Heuvel, J.P Locquet and S. Nuyts, "Beam energy considerations for gold nanoparticle enhanced radiation treatment", *Phys. Med. Biol.*, 55(16): 4509-4520, 2010.
78. E. Lechtman, N. Chattopadhyay, Z. Cai, S. Mashouf, R. Reilly and J. P. Pignol, "Implications on clinical scenario of gold nanoparticle radiosensitization in regards to photon energy, nanoparticle size, concentration and location", *Phys. Med. Biol.*, 56(15): 4631-4647, 2011.
79. W. E. Wilson, J. H. Miller, D. J. Lynch, R. R. Lewis, and M. Batdorf, "Analysis of Low-Energy Electron Track Structure in Liquid Water", *Radiation Research*, 161(5): 591-596, 2004.
80. I. El Naqa, P. Pater and J. Seuntjens, "Monte Carlo role in radiobiological modeling of radiotherapy outcomes", *Phys. Med. Biol.*, 57(11): R75-R97, 2012.
81. Nanodosimetry: Status of the Art, Workshop held at Legnaro Laboratories, 17-18 November, Italy, 2003, [http://www.euradnews.org/storyfiles/10099.0.workshop\\_summary.pdf](http://www.euradnews.org/storyfiles/10099.0.workshop_summary.pdf).
82. H. Bichsel, "Thoughts about nano dosimetry", *Advances in Quantum Chemistry*, 46: 329-338, 2004

83. F. W. Spiers., "The influence of energy absorption and electron range on dosage in irradiated bone", *Br. J. Radiol.*, 22(261): 521–33, 1949.
84. F. H. Attix, "Introduction to radiological physics and radiation dosimetry", 1<sup>st</sup> Edition, Chapter 16, page 504, 1986.
85. J. L. Humm, R. W. Howell, D. V. Rao, "Dosimetry of Auger-Electron-Emitting Radionuclide's", AAPM report No 49, 1995.
86. H. Matsudaira, A. M. Ueno and I. Furuno, "Iodine contrast medium sensitizes cultured mammalian cells to x-rays but not to  $\gamma$  rays", *Radiat. Res.*, 84(1): 144 – 148, 1980.
87. D. M. Herold, I. J. Das, C.C Stobbe, R.V. Iyer and J.D. Chapman , "Gold microspheres: a selective technique for producing biologically effective dose enhancement", *Int. J. Radiat. Biol.*, 76(10): 1357–1364, 2000.
88. T. Nowak, M. Hupfer, R. Brauweiler, F. Eisa and W. A. Kalender, "Potential of high-Z contrast agents in clinical contrast-enhanced computed tomography", *Med. Phys.*, 38(12): 6469–6482, 2011.
89. W. Ngwa, G. M. Makrigiorgos and R. I. Berbeco, "Gold nanoparticle-aided brachytherapy with vascular dose painting: Estimation of dose enhancement to the tumor endothelial cell nucleus", *Med. Phys.*, 39 (1): 392-398, 2012.
90. W. Ngwa, G. M. Makrigiorgos and R. I. Berbeco, "Applying gold nanoparticles as tumor-vascular disrupting agents during brachytherapy: estimation of endothelial dose enhancement", *Phys. Med. Biol.*, 55(21): 6533–6548, 2010.
91. R. I. Berbeco, W. Ngwa and G. M. Makrigiorgos, "Localized dose enhancement to tumor blood vessel endothelial cells via megavoltage x-rays and targeted gold nanoparticles: new potential for external beam radiotherapy", *I. J. Rad. Onc. Biol. Phys.*, 81(1): 270-276, 2011.
92. S. J. McMahon, W. B. Hyland, M. F. Muir, J. A. Coulter, S. Jain, K. T. Butterworth, G. Schettino, G. R. Dickson, A. R. Hounsell, J. M. O' Sullivan, K. M. Prise, D. G. Hirst and F. J. Currell, "Biological consequences of nanoscale energy deposition near irradiated heavy atom nanoparticles", *Scient. Reports*, 1: 18, 2011.
93. S.J. Mc Mahon, W.B. Hyland, M.F. Muir, J.A. Coulter, S. Jain, K.T. Butterworth, G. Schettino, G.R. Dickson, A.R. Hounsell, J.M. O'Sullivan, K.M. Prise, D.G. Hirst and F.J. Currell, "Nanodosimetric effects of gold nanoparticles in megavoltage radiation therapy", *Rad. Oncol.*, 100(3): 412-416, 2011.
94. W. N. Rahman, N. Bishara, T. Ackerly, C. Fa He, P. Jackson, C. Wong, R. Davidson and M. Geso, "Enhancement of radiation effects by gold nanoparticles for superficial radiation therapy", *Nanomedicine: Nanotechnology Biology and Medicine*, 5(2): 136–142, 2009.

95. F. Xiao, Y. Zheng, P. Cloutier, Y. He, D. Hunting and L. Sanche, "On the role of low-energy electrons in the radiosensitization of DNA by gold nanoparticles", *Nanotechnology*, 22(46): 465101, 2011.
96. Y. Zheng and L. Sanche, "Gold Nanoparticles Enhance DNA Damage Induced by Anti-cancer Drugs and Radiation" *Rad. Research*, 172(1): 114-119, 2009.
97. Y. Zheng, D. J. Hunting, P. Ayotte, L. Sanche, "Radiosensitization of DNA by Gold Nanoparticles Irradiated with High-Energy Electrons", *Radiation Research*, 169(1): 9-27, 2008.
98. J.P. Pignol, E. Rakovitch, D. Beachey and C. Le Sech, "Clinical significance of atomic inner shell ionization (ISI) and auger cascade for radiosensitization using IUdR, BUdR, platinum salts, or gadolinium porphyrin compounds", *Int. J. Radiation Oncology Biol. Phys.*, 55(4): 1082-1091, 2003.
99. S. Jain, J. A. Coulter, A. R. Hounsell, K. T. Butterworth, S. J. McMahon, W. B. Hyland, M. F. Muir, G. R. Dickson, K. M. Prise, F. J. Currell, J. M. O'Sullivan and D G Hirst, "Cell-specific radiosensitization by gold nanoparticles at Megavoltage radiation energies", *Int. J. Radiation Oncology Biol. Phys.*, 79(2): 531-539, 2011.
100. J.F. Hainfield, D.N. Slatkin and H.M. Smilowitz: "The use of gold nanoparticles to enhance radiotherapy in mice", *Phys Med Biol*, 49(18): N309-N315, 2004.
101. D.F. Regulla, L.B. Hieber and M. Seidenbusch, "Physical and biological interface dose effects in tissue due to X-ray-induced release of secondary radiation from metallic gold surfaces", *Radiat Res.*, 150(1): 92-100, 1998.
102. G. M. Makrigiorgos, S. J. Adelstein, and A. I. Kassis, "Limitations of Conventional Internal Dosimetry at the Cellular Level", *J Nucl. Med*, 30(11): 1856-1864, 1989.
103. L. M. Garcia, D. E. Wilkins and G. P. Raaphorst, " $\alpha/\beta$  ratio: a dose range dependence study", *Int. J. Radiation Oncology Biol. Phys.*, 67(2): 587-593, 2007.
104. J. Z. Wang, N. A. Mayr, S. Nag, J. Montebello, N. Gupta, N. Samsami and C. Kanellitsas, "Effect of edema, relative biological effectiveness, and dose heterogeneity on prostate brachytherapy", *Int. J. Radiation Oncology Biol. Phys.*, 67(2): 587-593, 2007.
105. M. I. Koukourakis, I. Abatzoglou, S. Touloupidi and I. Manavis, "Biological dose volume histograms during conformal hypo fractionated accelerated radiotherapy for prostate cancer", *Med. Phys.* 34 (1): 76-80, 2007.
106. J. L. Dumas, F. Lorchel, Y. Perrot, P. Aletti, A. Noel, D. Wolf, P. Courvoisier and J. F. Bosset, "Equivalent uniform dose concept evaluated by theoretical dose volume histograms for thoracic irradiation", *Physica Medica*, 23(1): 16-24, 2007.
107. D. J. Brenner and E. J. Hall, "Fractionation and protraction for radiotherapy of prostate carcinoma", *Int. J. Radiation Oncology Biol. Phys.*, 43(5): 1095-1101, 1999.



108. D. J. Brenner, A. A. Martinez, G. K. Edmundson, C. Mitchell, H. D. Thames and E. P. Armour, "Direct evidence that prostate tumors show high sensitivity to fractionation (low  $\alpha/\beta$  ratio), similar to late-responding normal tissue", *Int. J. Radiation Oncology Biol. Phys.*, 52(1): 6-13, 2002.
109. H. D. Thames, S. M. Bentzen, I. Turesson, M. Overgaard and W. Van Den Bogaert, "Fractionation parameters for human tissues and tumors", *Int. J. Radiat. Biol.*, 56(5): 701-710, 1989.
110. H. B. Kal and M. P. Van Gellekom, "How low is the  $\alpha/\beta$  ratio for prostate cancer?", *Int. J. Radiation Oncology Biol. Phys.*, 57(4): 1116-1121, 2003.
111. J. Z. Wang, M. Guerrero and X. A. Li, "How low is the  $\alpha/\beta$  ratio for prostate cancer?", *Int. J. Radiation Oncology Biol. Phys.*, 55(1): 194-203, 2003.
112. A. Dasu, "Is the  $\alpha/\beta$  Value for Prostate Tumours Low Enough to be Safely Used in Clinical Trials?", *Clinical Oncology*, 19(5): 289 -301, 2007.
113. J. Van Dyk, K. Mah and T.J. Keane, "Radiation-induced lung damage: dose-time-fractionation considerations", *Radiotherapy and Oncology*, 14(1): 55-69, 1989.
114. S. Unezaki, K. Maruyama, J. I. Hosoda, I. Nagae, Y. Koyanagi, M. Nakata, O. Ishida, M. Iwatsuru and S. Tsuchiya, "Direct measurement of the extravasation of polyethyleneglycol-coated liposomes into solid tumor tissue by in vivo fluorescence microscopy", *International Journal of Pharmaceutics*, 144(1): 11-17, 1996.
115. D. Lasne, G. A. Blab, S. Berciaud, M. Heine, L. Groc, D. Choquet, L. Cognet and B. Lounis, "Single Nanoparticle Photothermal Tracking (SNaPT) of 5-nm Gold Beads in Live Cells", *Biophysical Journal*, 91(12): 4598-4604, 2006.
116. S.K. Cheong, B. L. Jones, A. K. Siddiqi, F. Liu, N. Manohar and S. H. Cho, "X-ray fluorescence computed tomography (XFCT) imaging of gold nanoparticle-loaded objects using 110 kVp x-rays", *Phys. Med. Biol.*, 55(3): 647-662, 2010.
117. J. Li, A. Chaudhary, S. J. Chmura, C. Pelizzari, T. Rajh, C. Wietholt, M. Kurtoglu and B. Aydogan, "A novel functional CT contrast agent for molecular imaging of cancer", *Phys. Med. Biol.*, 55(15): 4389-4397, 2010.
118. E. Heath and J. Seuntjens, "Development and validation of a BEAMnrc component module for accurate Monte Carlo modeling of the Varian dynamic Millennium multileaf collimator", *Phys. Med. Biol.*, 48(24): 4045-4063, 2003.
119. I. Kawrakow, D. W. O. Rogers and B. R. B. Walters, "Large efficiency improvements in BEAMnrc using directional bremsstrahlung splitting", *Med. Phys.* 31(10): 2883-2898, 2004.
120. B. Bednarz and X. G. Xu, "Monte Carlo modeling of a 6 and 18 MV Varian Clinac medical accelerator for in-field and out-of-field dose calculations: development and validation", *Phys. Med. Biol.*, 54(4): N43-N57, 2009.

121. N. Tyagi, J. M. Moran, D. W. Litzenberg, A. F. Bielajew, B. A. Fraass and I J. Chetty, "Experimental verification of a Monte Carlo-based MLC simulation model for IMRT dose calculation" *Med. Phys.*, 34(2): 651-663, 2007.
122. J. V. Siebers, P. J. Keall, J. O. Kim and R. Mohan, "A method for photon beam Monte Carlo multileaf collimator particle transport", *Phys. Med. Biol.*, 47(17): 3225-3249, 2002.
123. J. O. Kim, J. V. Siebers, P. J. Keall, M. R. Arnfield and R. Mohan, "A Monte Carlo study of radiation transport through multileaf collimators", *Med. Phys.*, 28(12): 2497-2506, 2001.
124. I. A. Popescu, C. P. Shaw, S. F. Zavgorodni and W. A. Beckham, "Absolute dose calculations for Monte Carlo simulations of radiotherapy beams", *Phys. Med. Biol.*, 50(14): 3375-3392, 2005.
125. J. Deng, S. B. Jiang, A. Kapur, J. Li, T. Pawlicki and C. M. Ma, "Photon beam characterization and modeling for Monte Carlo treatment planning", *Phys. Med. Biol.*, 45(2): 411-427, 2000.
126. J. Seco, E. Adams, M. Bidmead, M. Partridge and F. Verhaegen, "Head-and-neck IMRT treatments assessed with a Monte Carlo dose calculation engine", *Phys. Med. Biol.*, 50(5): 817-830, 2005.
127. P. C. Lee, "Monte Carlo simulations of the differential beam hardening effect of a flattening filter on a therapeutic x-ray beam", *Med. Phys.* 24 (9): 1485-1489, 1997.
128. I. Kawrakow and B. R. B. Walters, "Efficient photon beam dose calculations using DOSXYZnrc with BEAMnrc", *Med. Phys.*, 33(8): 3046-3056, 2006.
129. O. Chibani and C.M. Ma, "On the discrepancies between Monte Carlo dose calculations and measurements for the 18 MV Varian photon beam", *Med. Phys.* 34(4): 1206-1216, 2007.
130. M. K. Fix, P. Manser, E. J. Born, R. Mini and P. Ruegsegger, "Monte Carlo simulation of a dynamic MLC based on a multiple source model", *Phys. Med. Biol.*, 46(12): 3241-3257, 2001.
131. D. Sheikh-Bagheri and D. W. O. Rogers, "Monte Carlo calculation of nine megavoltage photon beam spectra using the BEAM code", *Med. Phys.*, 29(3): 391-402, 2002.
132. S. H. Cho, O. N. Vassiliev, S. Lee, H. H. Liu, G. S. Ibbott and R. Mohan, "Reference photon dosimetry data and reference phase space data for the 6 MV photon beam from Varian Clinac 2100 series linear accelerators", *Med. Phys.*, 32(1): 137-148, 2005.
133. M.H. Lin, T. C. Chao, C.C. Lee, C.J. Tung, C.Y. Yeh and J.H. Hong, "Measurement-based Monte Carlo dose calculation system for IMRT pretreatment and on-line transit dose verifications", *Med. Phys.* 36(4): 1167-1175, 2009.
134. L. L. Wang and K. Leszczynski, "Estimation of the focal spot size and shape for a medical linear accelerator by Monte Carlo simulation", *Med. Phys.* 34(2): 485-488, 2007.
135. A. J. Scott, A. E. Nahum and J. D. Fenwick, "Monte Carlo modeling of small photon fields: Quantifying the impact of focal spot size on source occlusion and output factors, and

- exploring mini phantom design for small-field measurements”, *Med. Phys.* 36(7): 3132-3144, 2009.
136. H. Yoriyaz, M. Morales, P. de Tarso, D. Siqueira, C. C. Guimarães, F. B. Cintra and A. dos Santos, “Physical models, cross sections, and numerical approximations used in MCNP and GEANT4 Monte Carlo codes for photon and electron absorbed fraction calculation”, *Med. Phys.*, 36(11): 5198-5213, 2009.
  137. M. R. Arnfield, J. V. Siebers, J. O. Kim, Q. Wu, P. J. Keall and R. Mohan, “A method for determining multileaf collimator transmission and scatter for dynamic intensity modulated radiotherapy”, *Med. Phys.*, 27(10): 2231-2241, 2000.
  138. T. LoSasso, C.S. Chui and C. C Ling, “Physical and dosimetric aspects of a multileaf collimation system used in the dynamic mode for implementing intensity modulated radiotherapy”, *Med. Phys.*, 25(10): 1919-1927, 1998.
  139. D. Sheikh-Bagheria and D. W. O. Rogers, “Sensitivity of megavoltage photon beam Monte Carlo simulations to electron beam and other parameters”, *Med. Phys.*, 29(3): 379-390, 2002.
  140. G. X. Ding, “Using Monte Carlo simulations to commission photon beam output factors – a feasibility study”, *Phys. Med. Biol.*, 48(23): 3865–3874, 2003.
  141. R. Mohan, M. Arnfield, S.Tong, Q. Wu and J. Siebers, “The impact of fluctuations in intensity patterns on the number of monitor units and the quality and accuracy of intensity modulated radiotherapy”, *Med. Phys.*, 27(6): 1226-1237, 2000.
  142. T. Kairna, J. Kenny, S. B. Crowe, A. L. Fielding, R. D. Franich, P. N. Johnston ,R. T. Knight C. M. Langton, D. Schlect and J. V. Trapp, “Modeling a complex micro-multileaf collimator using the standard BEAMnrc distribution”, *Med. Phys.*, 37(4): 1761-1767, 2010.
  143. K. Bush, R. Townson<sup>1</sup> and S. Zavgorodni, “Monte Carlo simulation of RapidArc radiotherapy delivery”, *Phys. Med. Biol.*, 53(19): N359–N370, 2008.
  144. B. Libby, J. Siebers, and R. Mohan, “Validation of Monte Carlo generated phase-space descriptions of medical linear accelerators”, *Med. Phys.*, 26(8): 1476-1483, 1999.
  145. O. Pisaturo, R. Moeckli, R.O. Mirimanoff and F. O. Bochud, “A Monte Carlo-based procedure for independent monitor unit calculation in IMRT treatment plans”, *Phys. Med. Biol.*, 54(13): 4299–4310, 2009.
  146. K. Yuen, M. S. A. L. Al-Ghazia, C. L. Swift, C. A. White, “A practical method for the calculation of multileaf collimator shaped fields output factors”, *Med. Phys.*, 26(11): 2385-2389, 1999.
  147. S. Kim, “Characteristics of elliptical sources in BEAMnrc Monte Carlo system: Implementation and application”, *Med. Phys.*, 36(4): 1046-1052, 2009.

148. D. Schmidhalter, P. Manser, D. Frei, W. Volken and M. K. Fix,, "Comparison of Monte Carlo collimator transport methods for photon treatment planning in radiotherapy", *Med. Phys.*, 37(2): 492-504, 2010.
149. J. Pena, D. M. González-Castaño, F. Gómez, F. Sánchez-Doblado and G. H. Hartmann, "Automatic determination of primary electron beam parameters in Monte Carlo simulation", *Med. Phys.*, 34(3): 1076-1084, 2007.
150. G. X. Ding, "An investigation of accelerator head scatter and output factor in air", *Med. Phys.*, 31(9): 2527-2533, 2004.
151. B. A. Faddegon, M. Aubin , A. Bani-Hashemi, B. Gangadharan, A. R. Gottschalk, O. Morin, D. Sawkey, V. Wu and S. S. Yom, "Comparison of patient megavoltage cone beam CT images acquired with an unflattened beam from a carbon target and a flattened treatment beam", *Med. Phys.*, 37(4): 1737-1741, 2010.
152. D. L. Sawkey and B. A. Faddegon, "Determination of electron energy, spectral width, and beam divergence at the exit window for clinical megavoltage x-ray beams", *Med. Phys.*, 36(3): 698-707, 2009.
153. S. Y. Jang, O. N. Vassiliev, H. H Liu, R. Mohan and J. V. Siebers, "Development and commissioning of a multileaf collimator model in Monte Carlo dose calculations for intensity-modulated radiation therapy", *Med. Phys.*, 33(3): 770-781, 2006.
154. H. H. Liu, F. Verhaegen and L. Dong, "A method of simulating dynamic multileaf collimators using Monte Carlo techniques for intensity-modulated radiation therapy", *Phys. Med. Biol.*, 46(9): 2283-2298, 2001.
155. D.W.O. Rogers, B. Walters and I. Kawrakow, "BEAMnrc Users Manual", NRCC Report PIRS-0509, 2009.
156. D.W.O. Rogers, B. Walters and I. Kawrakow, "DOSXYZnrc Users Manual", NRCC Report PIRS-0509, 2009.
157. I. Kawrakow, E. Mainegra-Hing and D. W. O. Rogers, "EGSnrcMP: the multi-platform environment for EGSnrc", NRCC Report PIRS-877, 2006.
158. F. Lorenz, J. H. Killoran, F. Wenz and P. Zygmanski, "An independent dose calculation algorithm for MLC-based stereotactic radiotherapy", *Med. Phys.*, 34(5): 1605-1614, 2007.
159. F. Lorenz, A. Nalichowski, F. Rosca, J. Killoran, F. Wenz and P. Zygmanski, "An independent dose calculation algorithm for MLC-based radiotherapy including the spatial dependence of mlc transmission", *Phys Med. Biol.*, 53(3): 557-573, 2008.
160. P. Zygmanski, F. Rosca, D. Kadam, F. Lorenz, A. Nalichowski, L. Court and L. Chin "Determination of depth and field size dependence of multileaf collimator transmission in intensity- modulated radiation therapy beams", *J. Appl. Clin. Med. Phys.*, 8(4): 2693, 2007.

161. F. Lorenz, A. Nalichowski, F. Rosca, J. Kung, F. Wenz and P. Zygmanski, "Spatial dependence of mlc transmission in IMRT delivery", *Phys Med Biol.*, 52(19): 5985-5999, 2007.
162. J. H. Hubbell and S. M. Seltzer, "Tables of X-Ray Mass Attenuation Coefficients and Mass Energy-Absorption Coefficients from 1 keV to 20 MeV for Elements  $Z = 1$  to 92 and 48 Additional Substances of Dosimetric Interest," NISTIR, <http://www.nist.gov/pml/data/xraycoef/index.cfm>, 2009.
163. J. V. Siebers, P. J. Keall, J. Oh Kim and R. Mohan, "A method for photon beam Monte Carlo multileaf collimator particle transport", *Phys. Med. Biol.*, 47(17): 3225-3249, 2002.
164. F. Pönisch, U. Titt, S. F. Kry, O. N. Vassiliev and R. Mohan, "MCNPX simulation of a multileaf collimator", *Med. Phys.*, 33(2): 402-404, 2006.
165. J. O. Kim, J. V. Siebers, P. J. Keall, M. R. Arnfield, and R. Mohan, "A Monte Carlo study of radiation transport through multileaf collimators", *Med. Phys.*, 28(12): 2497-2506, 2001.
166. O. N. Vassiliev, S. F. Kry, J. Y. Chang, P. A. Balter, U. Titt and R. Mohan, "Stereotactic radiotherapy for lung cancer using a flattening filter free Clinac", *J. Appl. Clinical Med Phys*, 10(1): 2880, 2009.